Homodyned and Heterodyned Vibrational Sum Frequency Generation Spectroscopy of Electrochemical Interfaces

Dissertation

zur Erlangung des Grades eines
Doktors der Naturwissenschaften
am Fachbereich Physik
der Freien Universität Berlin

vorgelegt von

Tobias Garling
Berlin, 2020

Diese Arbeit wurde von Mai 2015 bis Oktober 2020 durchgeführt
im Department für Physikalische Chemie
am Fritz-Haber-Institut der Max-Planck-Gesellschaft.

Berlin, Oktober 2020

Abstract

Since its development in the 1980s the second-order nonlinear optical technique of vibrational sum frequency generation spectroscopy (SFG) evolved into a versatile tool to detect and characterize molecules at interfaces. To obtain complete information on the molecules' absolute orientation and to disentangle the interference of a possible non-resonant substrate's response which distorts the spectral line shape, however, phase-resolved measurements need to be applied. In such heterodyned SFG experiments the signal pulse which is generated by the nonlinear interaction between two incoming short pulses and a sample subsequently interferes with a so called local oscillator (LO) pulse. To yield accurate results, relative phase stability between the signal and LO as well as a precise control of their individual timings must be warranted. The simultaneous fulfillment of this two requirements so far have restricted heterodyned SFG experiments to the study of solid/air and liquid/air interfaces. This thesis presents a way to overcome these limitations by integrating a timing control scheme into a collinear high accuracy phase-resolved SFG spectrometer. The versatility of this approach is tested at the solid/liquid interface and extended to potential dependent measurements since among others understanding of electrochemical processes at the electrode/electrolyte interface will be critical in the development of more efficient batteries and fuel cells to tackle the challenges presented by the climate crisis. The obtained heterodyned SFG spectra allow an insight into the parameters that influence the non-resonant substrate's response, such as an applied potential bias and the presence of specifically and non-specifically adsorbed ions and molecules. In addition a method is presented how to use phase-resolved SFG spectra to determine the phase of the local field Fresnel factors, which so far had to be modeled. The heterodyned spectra are compared to their homodyned analogs to discuss which new information in fact can be obtained and what limits still need to be overcome.

Kurzzusammenfassung

Eine verbreitete Methode zur Charakterisierung von molekularen Prozessen an Grenzflächen ist die Summenfrequenz(SFG)-Schwingungsspektroskopie, die auf einem nichtlinearen optischen Effekt zweiter Ordnung beruht. Die ursprüngliche Methode detektiert die Intensität des SFG Signals. Dabei gehen jedoch Informationen über die absolute Orientierung der Moleküle an der Grenzfläche verloren. Außerdem kann ein nichtresonanter Beitrag des unterliegenden Substrats durch Interferenz die Linienform des Spektrums beeinflussen, was die Interpretation erschwert. Daher wurde unter Zuhilfenahme eines lokalen Oszillator (LO) Pulses die phasenaufgelöste SFG-Spektroskopie entwickelt. Zur Gewährleistung einer akkuraten Phasenauflösung muss eine konstante Phasenbeziehung zwischen Signal und LO vorherrschen. Außerdem verlangt die Methode eine präzise Kontrolle der individuellen Pulszeiten. Die gleichzeitige Einhaltung beider Voraussetzungen ist experimentell aufwendig, was bisher einen Einsatz über die Grenzflächen fest/gasförimg und flüssig/gasförmig hinaus verhinderte. Die vorliegende Arbeit erweitert den Einsatzbereich auch auf die fest/flüssig Grenzfläche und erlaubt damit auch phasenaufgelöste *in situ* Messungen elektrochemischer Prozesse an der Elektrodenoberfläche. Das Verständnis dieser Prozesse ist ein wichtiger Schritt zur Entwicklung effektiverer Batterien und Elektroden für Brennstoffzellen, wichtige Bestandteile zur Eindämmung des Klimawandels. Zur Realisierung solcher Messungen wird ein Schema zur Pulszeitkontrolle vorgestellt und in ein kollineares hoch präzises phasenaufgelöstes SFG-Spektrometer eingeführt. Die entstandenen phasenaufgelösten SFG-Spektren erlauben einen Einblick in die Abhängigkeit des nichtresonanten SFG Beitrags des Substrat von Faktoren wie einer angelegten elektrischen Spannung und der Anwesenheit gebundener/ungebundener Moleküle/Ionen an der Substratgrenzfläche. Desweiteren wird eine Methode vorgestellt, die es erlaubt die Phase der lokalen Feldfaktoren zu bestimmen, die bisher nur theoretisch berechnet werden konnte. Die phasenaufgelösten SFG-Spektren werden mit herkömmlichen SFG-Spektren verglichen um den zusätzlichen Informationsgewinn herauszuarbeiten, aber auch um noch offene Fragen zu erkennen.

Acknowledgments

Contents

Chapter 1

Introduction

Electrochemical interfaces play a crucial role in tackling one of the biggest challenges for humankind these days, namely to combat the climate crisis. One cornerstone in this fight is the reduction of green house gasses, that are the main contributor to global warming, by abandoning fossil fuels and using renewable sources, e.g. solar and wind energy, instead. However, these sources are not constantly available and concepts have to be developed how to store the typically electrical energy until consumption.[1] If it needs to be portable, e.g. to be used in zero-emission vehicles, this electrical energy can be used to either charge a battery or produce hydrogen in the electrolysis of water. Either way electrochemical interfaces are applied, that play a crucial role in determining the efficiency at which the energy is stored and ultimately extracted.[2] Understanding the fundamental processes that happen at the electrode/electrolyte interface and how to influence them is crucial for the development of new electrode materials that simultaneously act as catalysts for the desired electrochemical reactions thereby increasing the energy efficiency by lowering the necessary overpotential.[3,4] To obtain such kind of information, surface sensitive investigation tools are needed.

Another major application for electrochemical interfaces is their utilization in electrochemical bio-sensors.[5–9] Here the electrode surface is functionalized by attaching certain molecules/enzymes that allow for the interaction with specific analytes. During sensing these analytes either directly undergo or in-

fluence an electrochemical reaction at which the flown current is proportional to their concentration. These types of sensors are already widely applied and are able to detect e.g. cancer cells[6] ,the bird flu virus[10], and more recently to detect the novel corona virus in asymptomatic patients to tackle the global COVID-19 pandemic.[11] Interesting candidates for this kind of functionalized electrodes are molecular switches that allow for these sensors to be switched "On" or "Off" on demand which would e.g. facilitate the removal of the analyte after sensing and consequently enhance the sensor's reusability.[12–14] However, to be able to tailor biosensors for specific applications again surface sensitive methods are needed to characterize the functionalized electrode and understand the fundamental electrochemical processes at its interface.

Progress in the Characterization of Interfaces

The interest in understanding processes at the interface rapidly grew during the advent of heterogeneous catalysis around the beginning of the 20th century with Paul Sabatier systematically investigating the hydrogenation of organic and inorganic molecules under moderate conditions through the use of nickel powder[15] and Fritz Haber developing an effective ammonia synthesis from its elements.[16] Although the former formulated some qualitative rules on the molecular interaction with the catalyst, known as the Sabatier principle,[17] a structural understanding of the catalyst's electronic surface properties which differ from its bulk and are defined by active sites and the role of promoters which enhance the catalytic activity was not available.[16] When during the transition of Haber's ammonia synthesis from a laboratory scale to the industrial procedure known today as Haber-Bosch process a more abundant catalytic material had to be found than the originally used Osmium Uranium catalyst, this lack of knowledge forced Bosch's co-worker Alwin Mittasch to conduct approximately 6500 activity measurements from about 2500 different possible catalysts before an adequate replacement was found. This empirical strategy, today known as "catalyst screening", took three years.[16,18]
Several decades later the development of semiconductor devices and their subsequent progressive minimization made the fabrication and characterization of

surfaces on the atomic level necessary. The parallel evolution of the ultrahigh vacuum technique provided the possibility to obtain clean surfaces.[18] The process of "catalyst screening" now could be performed more methodically producing and varying defined surface structures, often single crystal surfaces, that act as model systems.[19–22] Simultaneously designed surface specific investigation tools, among others Auger electron spectroscopy (AES),[20,23,24] X-ray/UV photoelectron spectroscopy (XPS/UPS),[20,23,25–27] low-energy electron diffraction (LEED),[20,21,28,29] scanning tunneling (STM)[27,30,31] and atomic force microscopy (AFM),[32,33] were applied to characterize their surface structure and composition, oxidation state of surface atoms and/or bonding of adsorbates.[18] Eventually elementary steps at the catalyst's surface (e.g. educt adsorption, dissociation, product formation and desorption) were characterized for e.g. the Oxidation of carbon monoxide and the reduction of hydrogen on Pt(111)-surfaces, the ammonia synthesis or olefin polymerization.[18,22,34,35] These findings in collaboration with theoreticians allowed for the development and refinement of computer based models to tailor future catalysts' characteristics.[36] While the solid/gaseous interface became more and more accessible through the aforementioned surface techniques their application to monitor the properties and dynamics at the electrode/electrolyte interface remain limited, since these techniques either require ultra high vacuum conditions (e.g. XPS, AES and LEED) or are to slow (STM/AFM). Optical techniques in contrast are applicable to all interfaces accessible by light,[37–39] although linear optical techniques, e.g. IR spectroscopy, lack interface specificity and consequently the surface response is obscured by a much larger bulk response. Hence second order non linear optical processes were increasingly utilized that show an intrinsic surface specificity (on centrosymmetric media) and led to the adoption of second-harmonic (SHG), sum-frequency (SFG) and difference-frequency (DFG) generation spectroscopy.

Sum Frequency Generation Spectroscopy

In a typical SFG experiment the vibrational response of a molecule induced by an incoming IR beam, that is either broad-band or will be frequency-scanned,

is up converted by a (narrowband) visible pulse. Since its first performance by Shen in 1986[40,41] (vibrational) SFG spectroscopy has grown into a common technique to gain insight into molecules present at the air/water, solid/liquid (including electrode/electrolyte) or solid/gas interface by probing the system's material response described in the (complex) second order susceptibility $\chi^{(2)}$.[42] Additionally if different tensor components of $\chi^{(2)}$ in polarization dependent SFG measurements are addressed the molecules' confirmation and orientation (namely their tilt angle) with respect to the surface normal can be deduced.[40,43] However, the interpretation of SFG spectra can be severely impeded, if the underlying substrate also exhibits a second order response, that is typically non-resonant with respect to the incoming IR beam and consequently called non-resonant background $\chi^{(2)}_{NR}$. While for diamagnetics the magnitude of $\chi^{(2)}_{NR}$ is typically zero it can become significantly large for metals and semiconductors.[40] Depending on the relative phase relationship between the resonant molecular response $\chi^{(2)}_{R}$ and the substrate's $\chi^{(2)}_{NR}$ their interference produces a SFG Intensity spectrum, that is commonly detected in so called homodyned experiments, in which the resonant features are resolved in peaks, dips, or in-betweens. Therefore, if the phase of $\chi^{(2)}_{NR}$ is unknown, its interference with $\chi^{(2)}_{R}$ is a source for a huge fitting ambiguity since the resonance frequencies, which for a given molecule present at an interface might differ from its bulk values due to surface interactions, will not be unambiguously deducible from the spectrum.[38]

The origin of $\chi^{(2)}_{NR}$, namely intra- and/or inter-band transitions of electrons inside the metal surface, has been the subject of countless studies.[44–50] Nevertheless, information on its actual phase is often not available. This is especially true for electrified interfaces since the application of a potential bias has been shown to alter the phase by up to tens of degrees.[51–54] How the chemisorption of molecules or adsorption of ions at the electrode influence $\chi^{(2)}_{NR}$ is also not clear. To circumvent this problem instead of measuring the SFG Intensity phase-resolved, also called heterodyned, SFG measurements are applied, that directly determine the system's $\chi^{(2)}$ instead of its square. This way the interference between $\chi^{(2)}_{NR}$ and $\chi^{(2)}_{R}$ is reduced to a summation in which $\chi^{(2)}_{NR}$ becomes a simple off-set in the complex heterodyned SFG spectrum. Addition-

ally information about the sign of $\chi_R^{(2)}$ is available and thus information on the molecules' absolute orientation (pointing up-wards or downwards).[38,55] However, care must be taken in evaluating the phase of the complex spectrum, that must be corrected for the shift introduced by local field Fresnel factors, that relate the electric fields of the incoming pulses to the surface bound local field which ultimately radiates to yield the SFG signal. Those complex factors, that in the homodyned case only affect the spectral amplitude, mix the imaginary and real part of the phase-resolved spectrum. As a result the absorptive and dispersive part of $\chi_R^{(2)}$ are not entirely found in the imaginary and real part respectively. The contribution of the local field factors and how they are influenced by changing conditions at the interface, so far could not be determined unambiguously since the factor for the z-component of the local field is determined using the refractive index of the thin interfacial layer, a property which so far is inaccessible through experiments and has to be modeled.[56]

Phase-Resolved SFG Measurements of the Solid/Liquid Interface

To perform phase-resolved SFG measurements, that have been designed in recent years,[38] the system's SFG response is brought to interference with an additional local oscillator (LO) of known phase. Phase stability between the pulses involved, by e.g. creating the LO and SFG pulse by the same pulse pair (or a replica extracted by a beamsplitter) or using common optics,[38,52,57] is critical for a successful phase-resolved SFG measurement. The same is true for timing control between the LO and the signal pulse that must be adjustable.[58,59] Common heterodyned SFG spectrometer so far usually fulfill one requirement on the expense of the other. The resulting uncertainties in acquiring accurate phase information has led to conflicting interpretation in phase-resolved SFG spectra of the water/air interface by different groups[60–63] and so far prevented the method's application to electrochemical interfaces.[64]

Objective of This Thesis

The aim of the present thesis is to characterize processes at the electrode/electrolyte interface. In order to achieve this goal the existing experimental limi-

tations will be overcome by implementing a scheme for precise timing control between the LO and the signal pulse into a collinear setup with enhanced phase stability. Thus interfaces buried by liquids in general and electrochemical interfaces in particular will become accessible to phase-resolved SFG spectroscopy. Measurements at those interfaces will then be conducted to investigate the influence of an applied potential bias as well as the presence and absence of non-specifically and specifically adsorbed ions and molecules on the second order nonlinear substrate response on the one hand and the local field factors on the other hand. Information on those two properties will help to evaluate the SFG spectra to characterize fundamental processes at the electrode/electrolyte interface. As an example a self-assembled monolayer (SAM) of molecular photo-switches attached to a gold electrode will be investigated. These switches can exist in two different states of varying properties, that will possibly be affected by the application of an electric bias. Homodyned and heterodyned SFG spectra will be taken of the SAM and compared with respect to their information content and accuracy to gain crucial knowledge for the design of smart (bio-)sensors.

Structure of This Thesis

The thesis will be structured as follows. In the theory chapter 2 section 2.1 will provide the basic theory for nonlinear optics necessary for the understanding of this thesis. The specific cases of homodyned and heterodyned SFG spectroscopy is discussed. Furthermore an overview is given on the current knowledge on the origin of $\chi_{NR}^{(2)}$ and it is discussed, how $\chi_{NR}^{(2)}$ impedes the spectral interpretation in the case of homodyned SFG. In addition chapter 2.2 presents some basic concepts about self-assembled mono-layers and molecular switches which were used to modify our substrate in the SFG measurements.
Chapter 3 describes the components that have been implemented into a collinear time domain heterodyned SFG setup in order to achieve high accuracy phase-resolved SFG measurements, namely a balanced detection scheme (section 3.1.3), a scheme for pulse timing control (section 3.2) and the application of a z-cut alpha-quartz for the generation of a linearly polarized local oscillator

pulse (section 3.3). The applicability and versatility of the so modified set-up is shown in section 3.4.

Chapter 4 provides additional information on the employed Laser systems as well as on the sample preparation. Before their use in SFG measurements the samples are pre-characterized using IR spectroscopy and cyclic voltammetry, the results of which are discussed in chapter 5. Finally chapter 6 and 7 evaluate and compare the SFG spectra obtained in homodyned, respectively heterodyned measurements, among others the, to our best knowledge, first phase-resolved SFG spectra taken on electrochemical interfaces. The findings of this thesis and their implications on future measurements are summarized in 8.

Chapter 2

Theory

The following chapter shall provide the basic theory needed throughout this thesis. It will present the basic equations for the surface specific investigation tool of sum frequency generation (SFG) spectroscopy, a nonlinear optical technique which was used to characterize processes taking place at the solid/liquid interface between an electrode and an electrolyte. Furthermore this chapter will give an overview about how to modify such interfaces via the self-assembly of functional molecules such as molecular switches.

2.1 Nonlinear Optics

2.1.1 Origin of Nonlinear Optical Response

For a start we consider the case of a monochromatic local electric field $E_{loc}(\omega)$ present in a material system where it induces a number of (oscillating) dipole moments which on a macroscopic scale yields a polarization $P(\omega)$. Typically $P(\omega)$ depends linearly on the strength of the electric field according to[65]

$$P(\omega) = \epsilon_0 \chi^{(1)} E_{loc}(\omega) \tag{2.1}$$

In this equation ϵ_0 is the permittivity of free space and $\chi^{(1)}$ is the material

dependent factor of proportionality, also called linear susceptibility. The corresponding time domain description of the polarization, $P(t)$, is given by

$$P(t) = \epsilon_0 \chi^{(1)} E_{loc}(\omega) e^{i\omega t} \tag{2.2}$$

Equation 2.1 and 2.2 is a good approximation when the local field is weak. However, if $E_{loc}(\omega)$ becomes sufficiently strong, as is the case for optical electric fields created by lasers, $P(t)$ is more accurately described using a power series. [65]

$$
\begin{aligned}
P(t) =& P^{(1)}(t) + P^{(2)}(t) + P^{(3)}(t) + ... + P^{(n)}(t) \\
=& \epsilon_0 [\chi^{(1)} E_{loc}(\omega) e^{i\omega t} + \chi^{(2)} E_{loc}(\omega)^2 e^{i2\omega t} + \chi^{(3)} E_{loc}(\omega)^3 e^{i3\omega t} \\
& + ... + \chi^{(n)} E_{loc}(\omega)^n e^{in\omega t}]
\end{aligned} \tag{2.3}
$$

The term $P^{(1)}(t)$ is called linear polarization and equals the polarization as defined in equation 2.1, while the correction terms $P^{(2)}(t)$, $P^{(3)}(t)$ and $P^{(n)}(t)$ are called second, third and nth order nonlinear polarization respectively. Accordingly $\chi^{(n)}$ is called nth order nonlinear susceptibility. The relative size of $\chi^{(n+1)}$ compared to $\chi^{(n)}$ is typically smaller by many orders of magnitude and for condensed matter approximately 10^{-12}. [65]

If we look at the second order nonlinear polarization term and assume the general case of more than one distinct monochromatic local electric field present at the material system, then $P^{(2)}(t)$ is given by:

$$P^{(2)}(t) = \epsilon_0 E_{loc}^{(a)}(\omega_2) E_{loc}^{(b)}(\omega_1) e^{i(\omega_2 + \omega_1)} \chi^{(2)}(\omega_2; \omega_1) \tag{2.4}$$

The frequency components ω_3, at which $P^{(2)}(t)$ oscillates are given in equation 2.5 with $\delta(\omega_3 = \omega_2 + \omega_1)$ a delta function.

12

$$P^{(2)}(\omega_3) = \epsilon_0 E_{loc}^{(a)}(\omega_2) E_{loc}^{(b)}(\omega_1) \chi^{(2)}(\omega_2; \omega_1) \delta(\omega_3 = \omega_2 + \omega_1) \qquad (2.5)$$

The frequency components are called second harmonic, if $\omega_1 = \omega_2$, sum frequency if ω_1 and ω_2 are unequal in value but have equal signs and difference frequency if they have opposing signs. Because the local electric fields present at the material system are real in the time domain instead of negative frequencies one can also consider the respective complex conjugate field:

$$E(-\omega) = E^*(\omega) \qquad (2.6)$$

The oscillating polarization $P^{(2)}(\omega_3)$ given in equation 2.5 will act as a source for an electromagnetic wave and accordingly the material system will emit light at these frequencies.[37] The corresponding electric field $E(\omega_3)$ can be related to the incident laser fields $E(\omega_1)$ and $E(\omega_2)$ with the help of equation 2.5 and the complex nonlinear Fresnel factors L:

$$E(\omega_3) = L(\omega_3) L(\omega_2) E^{(a)}(\omega_2) L(\omega_1) E^{(b)}(\omega_1) \chi^{(2)}(\omega_2; \omega_1) \delta(\omega_3 = \omega_2 + \omega_1)$$
$$(2.7)$$

These local field factors L relate the incident laser fields $E^{(a)}(\omega_2)$ and $E^{(b)}(\omega_1)$ to the actual present local fields $E_{loc}^{(a)}(\omega_2)$ and $E_{loc}^{(b)}(\omega_1)$, respectively the generated local field $E_{loc}(\omega_3)$ to the emitted $E(\omega_3)$ thereby taking into account reflection, refraction or field enhancement as a result of the presence of the material system's interface.[56,66]

So far only monochromatic fields have been considered. For the case of ultrashort broadband pulses incident on the material we have to expand equation 2.7 by integrating over all frequencies of the incident pulses which yield the respective response at ω_3.

$$E(\omega_3) = L(\omega_3) \int_{-\infty}^{+\infty} \mathrm{d}\omega_2 \int_{-\infty}^{+\infty} \mathrm{d}\omega_1 L(\omega_2) E^{(a)}(\omega_2) L(\omega_1) E^{(b)}(\omega_1)$$
$$\cdot \chi^{(2)}(\omega_2; \omega_1) \delta(\omega_3 = \omega_2 + \omega_1) \tag{2.8}$$

Using relation 2.6 the integration can be carried out over positive frequencies only, if $E(\omega_3)$ and $E^*(\omega_3)$ are considered separately. The nonlinear response at the sum frequency is then given according to

$$E_{SFG}(\omega_3) = L(\omega_3) \int_0^{+\infty} \mathrm{d}\omega_2 \int_0^{+\infty} \mathrm{d}\omega_1 L(\omega_2) E^{(a)}(\omega_2) L(\omega_1) E^{(b)}(\omega_1)$$
$$\cdot \chi^{(2)}(\omega_2; \omega_1) \delta(\omega_3 = \omega_2 + \omega_1) \tag{2.9}$$

and

$$E_{SFG}^*(\omega_3) = L^*(\omega_3) \int_0^{+\infty} \mathrm{d}\omega_2 \int_0^{+\infty} \mathrm{d}\omega_1 L^*(\omega_2) E^{*(a)}(\omega_2) L^*(\omega_1) E^{*(b)}(\omega_1)$$
$$\cdot \chi^{(2)}(\omega_2; \omega_1) \delta(-\omega_3 = -\omega_2 - \omega_1) \tag{2.10}$$

with $\omega_2 \neq \omega_1$.

2.1.2 Symmetry Properties Of $\chi^{(2)}$

The electric fields as well as the polarization considered in the previous section are vectors and can be described within a Cartesian coordinate system defined by the orthogonal unit vectors $\vec{e_x}, \vec{e_y}$ and $\vec{e_z}$. The nth-order susceptibility $\chi^{(n)}$ in equation 2.3 relating the present electric fields to the nth-order nonlinear polarization induced in the material system is therefore a rank $n+1$ tensor, e.g. the linear susceptibility $\chi^{(1)}$ becomes a matrix, the second order nonlinear susceptibility $\chi^{(2)}$ a rank three tensor.[40,65] The second order nonlin-

ear polarization $P^{(2)}(\omega_3)$ in equation 2.5 can be defined in terms of its vector components as follows:

$$\vec{P}^{(2)}(\omega_3) = \sum_i^{x,y,z} \vec{e}_i P_i^{(2)}(\omega_3) = \epsilon_0 \sum_i^{x,y,z} \sum_j^{x,y,z} \sum_k^{x,y,z} \vec{e}_i \chi_{ijk}^{(2)} \vec{e}_j \vec{E}_{loc}^{(a)}(\omega_2) \vec{e}_k \vec{E}_{loc}^{(b)}(\omega_1) \quad (2.11)$$

$\chi^{(2)}$ consists of 27 tensor components that must be taken into account to describe $\vec{P}^{(2)}(\omega_3)$. However, symmetry considerations typically reduce the number of independent and nonzero elements $\chi_{ijk}^{(2)}$. As an example we shall consider the case for a material which exhibits inversion symmetry. Supposed the electric fields given in equation 2.11 invert their direction so that $j \rightarrow -j$ and $k \rightarrow -k$. This results in the polarization to also change sign $i \rightarrow -i$[65] and accordingly the susceptibility becomes $\chi_{ijk}^{(2)} \rightarrow \chi_{-i-j-k}^{(2)}$. However, reversing the sign of all tensor components equals a multiplication of this tensor by the scalar -1:

$$\chi_{-i-j-k}^{(2)} = -\chi_{ijk}^{(2)} \quad (2.12)$$

For a material which exhibits inversion symmetry its optical response should not depend on the direction of the incoming fields. So the following equality should hold:

$$\chi_{-i-j-k}^{(2)} = \chi_{ijk}^{(2)} \quad (2.13)$$

Equation 2.12 and 2.13 can only be true simultaneously if $\chi^{(2)}$ equals zero, that is if all tensor components vanish. This has some important consequences. Any second order nonlinear response which stems from a material that displays inversion symmetry (such as to an excellent approximation isotropic materials) cannot originate from the bulk within the dipole approximation but must

15

have its origin from the material's interface region where the inversion symmetry is necessarily broken along its surface normal.[37]This interface specificity has been successfully exploited for the characterization of surfaces using second order nonlinear optical techniques most notably SHG and SFG spectroscopy.[38,67–69]

2.1.3 Resonant Contribution to $\chi^{(2)}$

The process of sum frequency generation can be visualized with the help of an energy diagram (see figure 2.1) as a process in which a nonlinear optical active system absorbs two photons to reach an excited state to eventually relaxate into the ground state via emission of a single photon. Due to energy conservation this photon's frequency equals the sum of the incoming photons' frequency. The transition probability is greatly enhanced if one (or both) of the incoming photons' frequency excites an electronic or vibrational resonance as shown in figure 2.1B.

In case of vibrational SFG spectroscopy, which has successfully been utilized to detect molecules at interfaces,[38,67] one of the incident fields typically exhibits a frequency in the IR range, while the other field's frequency is typically located in the visible range to create a SFG field E_{SFG} equally oscillating in the visible frequency range which facilitates the detection of the latter one's intensity on a photo detector. The used visible pulse's frequency is fixed while the IR pulse can either be scanned in frequency[55,70] or is broadband[62,71]. E_{SFG} thus only parametrically dependents on the visible frequency and can be described as a function of the incident IR field according to equation[72]

$$\vec{E}_{SFG}(\omega_{IR}; \omega_{Vis}) \propto \chi^{(2)}(\omega_{IR}; \omega_{Vis})\vec{E}_{Vis}(\omega_{Vis})\vec{E}_{IR}(\omega_{IR}) \qquad (2.14)$$

In this equation $\chi^{(2)}(\omega_{IR}; \omega_{Vis})$ can be viewed as the sum of the macroscopic averaged second order hyperpolarizability β over all vibrations ν of the N molecules probed at the interface.[40] The hyperpolarizability is like $\chi^{(2)}$ a third rank tensor and reflects the symmetry of the molecular group whose vibration
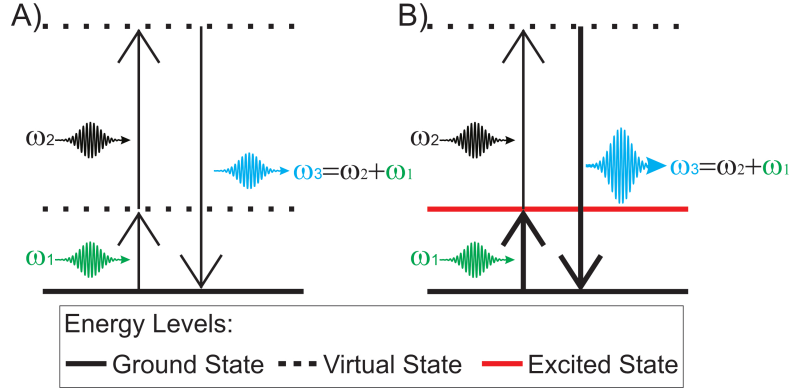
Figure 2.1: Energy diagram of SFG process. A)without and B) with resonant enhancement.

is examined. Its components are defined with respect to an internal molecular coordinate system with the axes a, b and c. To convert the hyperpolarizability into the surface bound coordinate system upon which $\chi^{(2)}$ is defined three rotations around the Euler angles ψ, θ and ϕ (twist, tilt and azimuthal angle respectively) have to be performed using rotation matrices R. $\chi^{(2)}$ can thus be deduced by:

$$\chi^{(2)} = \sum_{i,j,k} \chi^{(2)}_{ijk} = \frac{N}{\epsilon_0} \sum_{\nu} \sum_{a,b,c} < R(\psi)R(\theta)R(\phi)\beta_{\nu;abc} > \qquad (2.15)$$

The hyperpolarizability for vibrational resonances is given as[40,73]

$$\beta_{\nu;abc} = \frac{1}{2\hbar} \frac{\alpha_{\nu;ab}\mu_{\nu;c}}{\omega_\nu - \omega_{IR} - i\Gamma_\nu} \qquad (2.16)$$

As can be seen in equation 2.16 the hyperpolarizability becomes huge, if the frequency of the incident IR field ω_{IR} equals an eigenfrequency ν of the molecule (with Γ_ν^{-1} being the decay time of the excited resonance). Additionally to posses a nonzero hyperpolarizability the corresponding normal mode needs to exhibit both a nonzero Raman transition moment $\alpha_{\nu;ab}$ and a nonzero IR tran-

sition dipole moment $\mu_{\nu;c}$. Hence an important selection rule for vibrations to be observed in an SFG experiment consists of this vibration to be both IR and Raman active.

In summary the hyperpolarizability β and thus the corresponding averaged $\chi^{(2)}$ can be resonantly enhanced with the tunable IR laser. In vibrational SFG spectroscopy this contribution to the overall (or effective) second order susceptibility $\chi^{(2)}_{eff}$ is called resonant part or $\chi^{(2)}_R$. Due to its resonant nature the phase of the complex $\chi^{(2)}_R$ will always be $\pm 90°$. The non-resonant analogue which does not show resonant enhancement as a function of IR frequency is conversely called $\chi^{(2)}_{NR}$ and will be discussed in 2.1.5.

2.1.4 Polarization-Dependent Measurements

Different tensor elements of the nonlinear second order susceptibility $\chi^{(2)}_{ijk}$ (see also section 2.1.2) can be individually addressed in polarization dependent measurements. Therefore linearly polarized incident fields are utilized and the generated nonlinear response is measured at a specific polarization. In these measurements P-polarized light which is polarized parallel to the plane of incidence (POI) can be resolved into x and z components at the surface(see figure 2.2), while the S-polarized light is polarized perpendicular to the POI and exhibits an electric field vector exclusively along the y axis. The pulses' polarization in such measurements are given in the order SFG response, visible and IR pulse which is analogous to the order of the $\chi^{(2)}_{ijk}$ indices. As an example the SSP polarization combination, only probes the tensor components $\chi^{(2)}_{yyx}$ and $\chi^{(2)}_{yyz}$ of which only the latter is non zero for isotropic surfaces.[40] Of all possible polarization combinations only PPP, SSP, SPS and PSS yield non-zero tensor components for isotropic surfaces.[40]

Equation 2.15 shows, that the tensor components of the resonant part of the second order susceptibility $\chi^{(2)}_R$ depend for one on the tensor components of β_ν and thus on the symmetry of the hyperpolarizability's original vibrational mode ν. Additionally its tensor components also depend on the orientation of the functional group where the vibrational mode originates from. Comparing the magnitude of $\chi^{(2)}_R$ obtained in different polarization dependent measure-
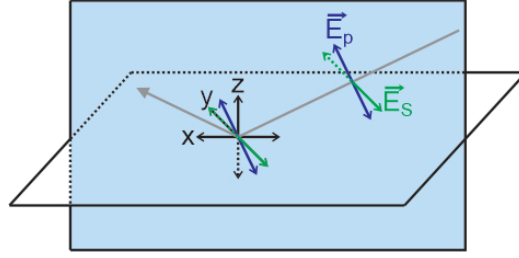
Figure 2.2: Beam polarization with respect to the surface bound coordinate system. The plane of incidence is highlighted in blue.

ments as well as taking into account the vibrational mode's symmetry thus allows for the deduction of the tilt angle with respect to the surface normal and if the sign of $\chi_R^{(2)}$ is accessible the group's absolute orientation (pointing upwards/downwards).[74,75]

To access $\chi^{(2)}$, however, the determined $\vec{E}_{SFG}$ and the incident fields $\vec{E}_{Vis}$ and $\vec{E}_{IR}$ need to be related to the local fields present at the interface with the help of the nonlinear Fresnel factors L already introduced in equation 2.7 in chapter 2.1.1. With the help of the normalized electric field vectors that contain the information about the field's actual polarization $\vec{\epsilon}_{Vis}$ and $\vec{\epsilon}_{IR}$, $\vec{E}_{SFG}$ is described according to:

$$\vec{E}_{SFG} = \sum_i^{x,y,z} \sum_j^{x,y,z} \sum_k^{x,y,z} L_{ii}(\omega_{SFG}) \vec{e}_i \chi_{ijk}^{(2)}(\omega_{SFG})$$
$$L_{jj}(\omega_{Vis}) \vec{e}_j \vec{\epsilon}_{Vis} |\vec{E}_{Vis}(\omega_{Vis})| L_{kk}(\omega_{IR}) \vec{e}_k \vec{\epsilon}_{IR} |\vec{E}_{IR}(\omega_{IR})| \tag{2.17}$$

The complex L-factors are derived from the linear Fresnel-factors r.[56,66] For the case of reflection and co-propagating beam geometry (Vis and IR travel in the same x-direction) they are defined for the three principal directions x, y and z as follows:

$$L_{xx}(\omega) = 1 - r_{p,12}(\omega) = \frac{2n_1(\omega)cos(\theta_2)}{n_2(\omega)cos(\theta_1) + n_1(\omega)cos(\theta_2)}$$

$$L_{yy}(\omega) = 1 + r_{s,12}(\omega) = \frac{2n_1(\omega)cos(\theta_1)}{n_1(\omega)cos(\theta_1) + n_2(\omega)cos(\theta_2)}$$

$$L_{zz}(\omega) = 1 + r_{p,12}(\omega)(\frac{n_1(\omega)}{n_{int}(\omega)})^2 = \frac{2n_2(\omega)cos(\theta_1)}{n_2(\omega)cos(\theta_1) + n_1(\omega)cos(\theta_2)}(\frac{n_1(\omega)}{n_{int}(\omega)})^2$$

$$(2.18)$$

The (complex) refractive indices n_1 and n_2 belong to the incident and reflecting medium respectively and accordingly θ_1 and θ_2 are the angle of incidence and angle of refraction. n_{int} is the effective refractive index of the interfacial layer. Since the refractive index is a macroscopic property it is not well defined for the interface as it is only a few monolayers thick. The actual value therefor is difficult to measure and often needs to be modeled.[56,76]

2.1.5 Non-Resonant Substrate Contribution to $\chi^{(2)}$ in Metals

General Overview

As opposed to $\chi_R^{(2)}$ which was discussed in chapter 2.1.3, $\chi_{NR}^{(2)}$ is non-resonant with respect to the incoming IR puls' frequency. Its complex phase therefor needs not necessarily take the value of $\pm 90°$. As shall be shown in chapter 2.1.6 which describes homodyned vibrational SFG spectroscopy the interference of $\chi_R^{(2)}$ and $\chi_{NR}^{(2)}$ causes huge data analysis problems due to the often unknown difference in their complex phases.

The origin of this non-resonant response and how it is influenced by e.g. an applied electric bias or the presence of molecule/ions at the interface has been the subject of numerous theoretical[47–50] and applied studies.[44–46] Especially valuable information has been provided by second harmonic generation measurements that investigated the azimuthal anisotropy of the nonlinear response of single crystal metal electrodes.[54,77,78]

In general the non-resonant second order susceptibility $\chi_{NR}^{(2)}$ and thus the non-linear response of the metal substrate's electrons to the incident electromag-

netic field can be split into parts referring to the excitation of intra-band transitions of the quasi free conduction electrons $\chi_{intra}^{(2)}$ and inter-band transitions $\chi_{inter}^{(2)}$ of the bound valence electrons.[45,48,79]

$$\chi_{NR}^{(2)} = \chi_{intra}^{(2)} + \chi_{inter}^{(2)} \tag{2.19}$$

Contributions due to Inter-band Transitions

Inter-band transitions occur when the upconversion beam's frequency ω_{Vis} (or resulting SHG/SFG, or both) matches the energy difference ω_{eg} between the energy level of bound valence electrons (ground state) and an excited electronic bulk or surface state.[44,45] For simplicity only one dominant transition is assumed which is resonant with the up-conversion beam's frequency ω_{Vis}, so that $\omega_{Vis} = \omega_{eg}$. $\chi_{inter}^{(2)}$ then becomes,[45]

$$\chi_{inter}^{(2)} = \frac{\beta_e}{(\omega_{Vis} - \omega_{eg} + i\Gamma_{eg})} \approx i\frac{\beta_e}{\Gamma_{eg}} \tag{2.20}$$

where Γ_{eg} and β_e act as the corresponding damping constant and the transitions strength respectively. An applied bias leads to changes in the occupation and distribution of electronic states at the interface,[46] thus changing β_e and the energy difference between ground and excited electronic states. Additionally bias induced specific adsorption of ions at the electrode/electrolyte interface influences the energies of surface states or creates new orbitals through mixing of adsorbate and substrate states thus also contributing to the electric potential-dependence of $\chi_{inter}^{(2)}$.[46,80,81]

Contribution due to Intra-band Transitions

In the absence of inter-band transitions the induced nonlinear polarization in a metal originates from the motion of its conduction electrons induced by the external incident field.[47,78] The corresponding susceptibility for this intra-band

transition $\chi^{(2)}_{intra}$ can be related to the normal and tangential surface suscepti-
bility χ_a and χ_b, respectively, as well as the bulk susceptibility χ_d via,[45,47]

$$\chi^{(2)}_{intra} = \frac{\bar{n}}{\omega_1^2 \cdot \omega_2^2}(\chi_a + \chi_b + \chi_d) \qquad (2.21)$$

where ω_1 and ω_2 are the incident beams' frequencies and $\bar{n}$ equals the bulk
electron density. The individual components are defined as,[45,50]

$$\chi_a = \epsilon_{SFG}sin(\theta_{SFG})sin(\theta_{Vis})sin(\theta_{IR})a(\omega_{Vis}, \omega_{IR}) \qquad (2.22)$$

$$\chi_b = \frac{-2\sqrt{\epsilon_{SFG} - sin^2(\theta_{SFG})}}{\omega_{SFG}}b(\omega_{Vis}, \omega_{IR})$$
$$\cdot (\omega_{Vis}\sqrt{\epsilon_{Vis} - sin^2(\theta_{Vis})}sin(\theta_{IR}) + \omega_{IR}\sqrt{\epsilon_{IR} - sin^2(\theta_{IR})}sin(\theta_{Vis}))$$
$$(2.23)$$

$$\chi_d = \frac{2\omega_{Vis}\omega_{IR}}{\omega_{SFG}^2}(\sqrt{\epsilon_{Vis} - sin^2(\theta_{Vis})}\sqrt{\epsilon_{IR} - sin^2(\theta_{IR})} + sin(\omega_{Vis})sin(\omega_{IR}))$$
$$(2.24)$$

with ϵ_i the dielectric constant of the substrate at $\omega_{SFG}, \omega_{Vis}$ and ω_{IR} respec-
tively and θ_i the respective angle of incidence/reflection.
The phenomenological parameters a and b where first introduced by Rudnick
and Stern[47] for SHG off a metal surface described within a jellium model for
a free electron metal. The parameter b takes into account boundary scattering
and hence is influenced by the surface roughness and flatness.[47] For a per-
fectly reflecting flat boundary its value takes -1.[47,50,82] The parameter a on the
other hand is a measure of the integrated weight of the induced surface polar-
ization and depends on the relative density profiles of free and bound electrons
across the interface.[82,83] Therefore, other than χ_b and χ_d, χ_a depends on an

applied electric potential.[45,78] The main tensor component of gold substrate's non-resonant second order susceptibility contributing to χ_a is $\chi^{(2)}_{zzz}$.[46,78,80]

Potential-dependence of Intra-band Transitions

The normal component of the surface susceptibility χ_a can be described as linear dependent on the strength of a static electric field E_{dc}, as defined in equation 2.25, due to an applied potential V_{dc} (with V_{pzc} the potential of zero charge).[45]

$$E_{dc} \propto V_{dc} - V_{pzc} \qquad (2.25)$$

This static electric field can be treated similar as the electric fields created by the incident visible and IR pulses with the frequency $\omega_{dc} = 0$. Therefore SFG (as well as SHG) from electrified interfaces is often viewed as a third order process, were the sum of the incident beam's frequency and the zero frequency of the dc field yield ω_{SFG}.[45,84–86]

$$\chi_a = \chi^{(3)}(\omega_{SFG}, \omega_{Vis}, \omega_{IR}, 0)E_{dc} \propto \chi^{(3)}(\omega_{SFG}, \omega_{Vis}, \omega_{IR}, 0)(V_{dc} - V_{pzc}) \quad (2.26)$$

Although the third order susceptibility $\chi^{(3)}$ is much smaller than $\chi^{(2)}$ as was pointed out in chapter 2.1.1 its contribution can still be significant since the huge field strength within the electric double layer due to an applied potential compensates for this effect. However, the value of viewing SFG from electrified interfaces as a third order process remains debatable. Since the presence of a static electric field can break the inversion symmetry of a material medium,[65] one can argue, that its presence just adds to the symmetry break due to the presence of the interface and thus just enhances $\chi^{(2)}$.

Summarizing the potential-dependent and independent intra-band suscepti-bility parts into the constants α and δ respectively and taking the square one ends up with the equation of the parabolic model that is frequently used to

describe the off-resonant behavior of the SFG/SHG intensity obtained in bias dependent homodyned measurements.[51,87,88]

$$I_{SFG/SHG} \propto |\chi_{intra}^{(2)}|^2 \propto |\alpha(V_{dc} - V_{pzc}) + \delta|^2 \qquad (2.27)$$

If δ is sufficiently small the minimum of I_{SFG} can be used to detect the potential of zero charge.[51]

Mixing of Intra- and Inter-band Contribution

Deviations from this parabolic behavior indicate the presence of inter-band transitions. Within the Drude model for a free electron like metal the respective dielectric constants of the substrate at $\omega_{SFG}, \omega_{Vis}$ and ω_{IR} in equation 2.22-2.24 are real numbers.[45] Consequently $\chi_{intra}^{(2)}$ (see equation 2.21) is entirely real as well. In contrast $\chi_{inter}^{(2)}$ as given in equation 2.20 is in good approximation entirely imaginary. The phase of $\chi_{NR}^{(2)}$ will therefore be influenced by the ratio of $\chi_{intra}^{(2)}$ and $\chi_{inter}^{(2)}$ which as described behave independently as a function of applied potential.

In this context it is worth noting that equation 2.20 and 2.21 do not take into account the complex Fresnel factors. These factors can mix the imaginary and real part of a materials second order non linear response as will be further explained in chapter 2.1.7. Taking into account these factors may explain the observations made by Wong et all.[78] In their experiment they observed the azimuthal dependence of the $\chi^{(2)}$ response on a single crystal Au[111] and Ag[111] surface. They were able to disentangle the χ_{zzz} and χ_{xxx} components based on their different behavior with respect to the azimuth angle (χ_{zzz} being independent and thus appeared as the isotropic component, while χ_{xxx} dominated the three-fold symmetry component). Both components were related to intra-band transition and hence should both be real. Nonetheless a phase difference between them was observed, which can be rationalized by the tensor components' different corresponding Fresnel factors.[78]

Equivalently as being rationalized as a function of applied bias as was done

in equation 2.26 χ_a and thus the real part of the isotropic parameter obtained in azimuthal dependent anisotropy measurements can be viewed as a linear function of the surface charge density (which is approximately linear with the static electric field[51]), which can be influenced by non specific ion adsorption.[80]

Ion adsorption on single crystal surfaces can additionally induce (in the case of cations) or lift surface reconstruction (e.g. surface reconstruction at the Au[111] surface leads to the compression of the top layer in the [1$\bar{1}$0] direction).[46,89,90] Thereby the surface's symmetry is changed and consequently new tensor components of the non-resonant second order susceptibility can contribute to the overall susceptibility.

2.1.6 Homodyned Vibrational SFG Spectroscopy

Since the generated electric field of a materials SFG response $\vec{E}_{SFG}$ as defined in equation 2.17 in chapter 2.1.4 is not easily accessible, the most common approach in vibrational SFG spectroscopy is to detect its intensity I_{SFG}[38] which is given as the square of equation 2.17:

$$I_{SFG} = |\sum_{i}^{x,y,z} \sum_{j}^{x,y,z} \sum_{k}^{x,y,z} L_{ii}(\omega_{SFG})\vec{e}_i \chi^{(2)}_{eff;ijk}(\omega_{SFG}) L_{jj}(\omega_{Vis})\vec{e}_j\vec{\epsilon}_{Vis} L_{kk}(\omega_{IR})\vec{e}_k\vec{\epsilon}_{IR}|^2 I_{Vis}I_{IR}$$

(2.28)

I_{SFG} is directly proportional to the square of the effective susceptibility $\chi^{(2)}_{eff}$ and the incident beams intensities' I_{Vis} and I_{IR}. $\chi^{(2)}_{eff}$ equals the sum of the resonant and non-resonant contribution to $\chi^{(2)}$. Their origin and the resulting expected difference in their complex phases Φ_R ($\Phi_R = \pm 90°$) and Φ_{NR} is described in chapter 2.1.3 for the resonant and chapter 2.1.5 for the non-resonant part. The square can be written as:

Pol. Combination	$\lvert L_{ijk} \rvert^2$	Air	Acetonitrile
PPP	$\lvert L_{zzz} \rvert^2$	4.93	186.06
	$\lvert L_{xxz} \rvert^2$	1.64	2.62
	$\lvert L_{xzx} \rvert^2$	0.02	0.09
	$\lvert L_{zxx} \rvert^2$	0.02	0.05
SSP	$\lvert L_{yyz} \rvert^2$	0.005	0.30

Table 2.1: Calculated Fresnel factors for experimental geometry used during homodyned SFG experiments: $\Theta_{SFG} = 60°$, $\Theta_{Vis} = 65°$, $\Theta_{IR} = 40°$. $\omega_{SFG} = 645\,nm$, $\omega_{Vis} = 800\,nm$, $\omega_{IR} = 3300\,nm$. The change in incident angles for the case of acetonitrile due to refraction at the air/liquid interface given by Snell's law has been considered. Calculation details can be found in the appendix.

$$\begin{aligned}
\lvert \chi_{eff}^{(2)} \rvert^2 &= \lVert \chi_R^{(2)} \rvert e^{i\Phi_R} + \lvert \chi_{NR}^{(2)} \rvert e^{i\Phi_{NR}} \rvert^2 \\
&= \lvert \chi_R^{(2)} \rvert^2 + \lvert \chi_{NR}^{(2)} \rvert^2 + 2\lvert \chi_R^{(2)} \rvert \lvert \chi_{NR}^{(2)} \rvert cos(\Phi_R - \Phi_{NR})
\end{aligned} \tag{2.29}$$

Depending on the phase relation of $\chi_R^{(2)}$ and $\chi_{NR}^{(2)}$ the cross term in equation 2.29 can add constructively or destructively. Their phase relation therefore has a strong influence on the line shape of the resulting homodyned SFG spectrum.

Fitting Equation of Homodyned Vibrational SFG spectroscopy

Using equation 2.15 and 2.16 to describe $\chi_R^{(2)}$ we can derive the fitting equation which was used in this thesis for homodyned SFG spectra for a given experimental geometry (incidence angles, polarization combination) according to:

$$I_{SFG} = \lvert \chi_{eff}^{(2)} \rvert^2 I_{Vis} I_{IR} = \lVert \chi_{NR}^{(2)} \rvert e^{i\Phi_{NR}} + \sum_{\nu} \frac{A_{\nu}}{\omega_{\nu} - \omega_{IR} - i\Gamma_{\nu}} \rvert^2 I_{Vis} I_{IR} \tag{2.30}$$

Here A_{ν} and $\lvert \chi_{NR}^{(2)} \rvert$ are the amplitudes of the individual resonances and the non-resonant part respectively. The amplitudes also take care of the local field factors which were present in equation 2.28. While their phase is lost while taking the square, it is worth noting that they have a strong influence on the final

26
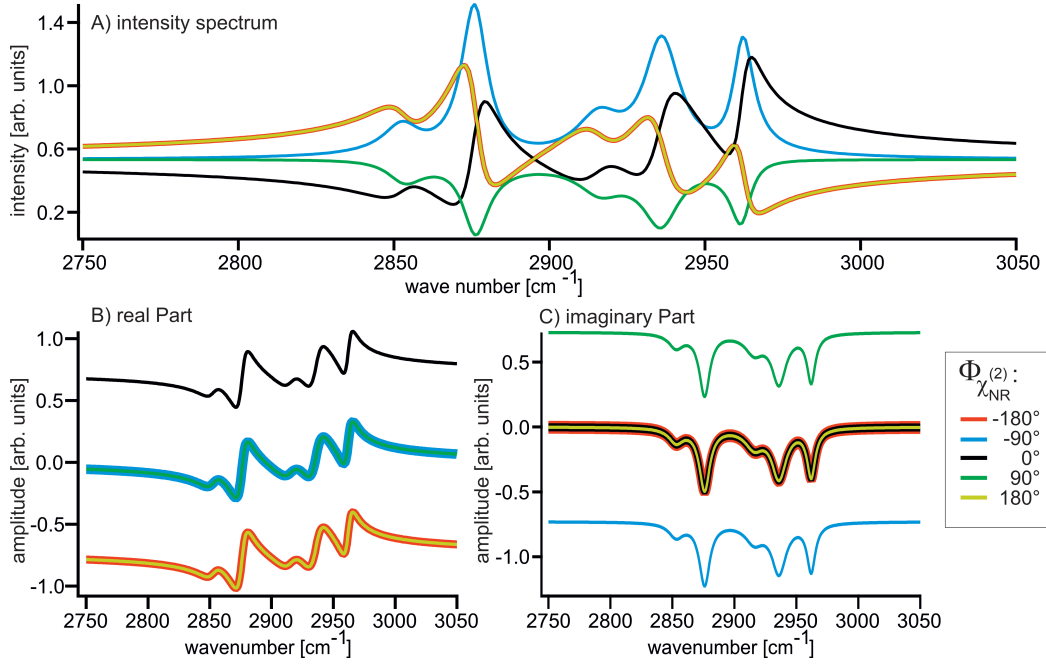
Figure 2.3: Influence of changes in Φ_{NR} on simulated homodyned SFG line shape. A) Intensity Spectrum and corresponding B) Real and C) Imaginary Part. Local field factors which might mix the real and imaginary part not taken into account.)

intensity of the SFG signal. The calculated relevant Fresnel factors for our experimental geometry during homodyned SFG measurements on self-assembled monolayers at a gold surface are listed in table 2.1 (for experimental details see chapter 4.1). For the interfacial refractive index $n_{int}(\omega)$ (see equation 2.18) for all fields the value 1.18 was assumed according to a previous publication for the case of hydrocarbons present at the gold interface.[76] Assumed all nonzero tensor components of $\chi_{eff}^{(2)}$ are of comparable magnitude, according to table 2.1 our measurements taken in PPP-polarization combination will be dominated by the $\chi_{zzz}^{(2)}$-term and SFG signals measured under SSP-polarization combination will be orders of magnitude weaker.

Equation 2.30 was used to illustrate the effect of the non-resonant phase on the line shape of the final SFG spectrum. The fitting values (resonant and non-resonant amplitudes $A_{NR/R}$, FWHM Γ_ν and resonance frequencies ω_ν) of an

actual spectrum of a self-assembled monolayer of octadecanethiol (see table 7.1 in chapter 7.1.4) were plugged into equation 2.30 and Φ_{NR} was varied (see figure 2.3A). The simulated homodyned SFG spectrum shows, that without knowledge of Φ_{NR} it is difficult to determine the actual center frequencies ω_ν and a correct interpretation of the spectrum remains problematic. Many publications therefore rely on IR bulk comparison spectra taken for the molecules present at the interface and literature values of Φ_{NR}.[91] However, to get rid of this problem phase-resolved measurements can be conducted that determine E_{SFG} rather than its intensity and accordingly the complex $\chi_{eff}^{(2)}$ rather than $|\chi_{eff}^{(2)}|^2$.[38] The corresponding real and imaginary part of $\chi_{eff}^{(2)}$ are presented in figure 2.3B and C respectively. Here the non-resonant contribution simply acts as an offset and the resonant line shape remains unaffected. Additionally the effect of the local field factors will be less pronounced on the strength of the acquired signals in different polarization combinations since the latter now depends only linearly on those factors. Phase-resolved, also called heterodyned, vibrational SFG spectroscopy will further be discussed in the following chapters.

2.1.7 Frequency Domain Heterodyned Vibrational SFG Spectroscopy

Collinear Approach

Due to the problems in disentangling the resonant and non-resonant contributions to $\chi_{eff}^{(2)}$ in homodyned measurements as discussed in the previous chapter, phase-resolved vSFG spectroscopy has been developed. The most common approaches so far are the frequency domain techniques with two distinct types of setups, a collinear and a non-collinear version.[38] In the collinear approach narrow-band *ps* laser pulses are used of which the frequency of the visible pulse is kept fixed while the IR frequency is scanned during the course of experiment (see figure 2.4 A).[55] The two pulses are sent to a reference material where they generate the local oscillator (LO). Subsequently all three beams simultaneously pass a delay plate (DP), sometimes also called phase modulator plate.
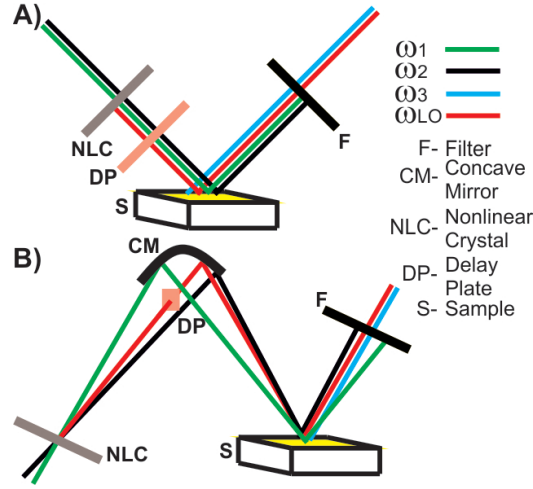
Figure 2.4: Different phase-resolved sum frequency generation schemes for measurements in the frequency domain. A) collinear IR frequency scanning approach. B) non collinear IR broad band approach.

Its angle towards the beams determines the distance they travel through the plate and thus controlled changes to their relative phases can be introduced due to dispersion by changing said angle. Finally the beams pass the sample to generate the sample SFG pulse which interferes with the LO. The resulting intensity can be detected with a photomultiplier tube (PMT) or a photodiode. It is worth noting that the order of the LO and the sample is interchangeable. The SFG signal reflected from the sample, $I_{SFG;S}$, is given by:[55]

$$I_{SFG} = A[||\chi_{eff;S}^{(2)}|e^{i\Phi_{eff;S}} + a|\chi_{LO}^{(2)}|e^{i\Phi_{LO}}|^2 + b^2|\chi_{LO}^{(2)}|^2] \qquad (2.31)$$

Since only a part of the LO field overlaps and subsequently interferes with the sample signal, the constants a and b are introduced to distribute the total LO intensity to the actual interfering and non-interfering intensities. The constant A depends on the overlapping beam profiles of the incident beams.[38] To obtain the phase-resolved SFG spectrum a minimum of four frequency scans is necessary: two to determine the pure LO spectrum and the pure signal spectrum respectively as well as two spectra recording their interference at two different

angles of the DP where the phase difference between the LO and the sample signal changes by 90° from one scan to the other, $I_{SFG;1}$ and $I_{SFG;2}$, respectively.[55] The phase difference between $\Phi_{eff;S}$ and Φ_{LO} can then be calculated to:

$$\Phi_{eff;S} - \Phi_{LO} = tan^{-1}(\frac{I_{SFG;2} - A|\chi_{eff;S}^{(2)}|^2 - A(a^2 + b^2)|\chi_{LO}^{(2)}|^2}{I_{SFG;1} - A|\chi_{eff;S}^{(2)}|^2 - A(a^2 + b^2)|\chi_{LO}^{(2)}|^2}) \qquad (2.32)$$

For determining the absolute phase another 4 scans are necessary on a reference sample with known phase. Analogous to equation 2.32 this yields the phase difference between $\Phi_{eff;Ref}$ and Φ_{LO}. Subtracting both results ultimately yields $\Phi_{eff;S}$.[38,55]

Non-Collinear Approach

The non-collinear type of setups (see figure 2.4B) makes use of broadband pulses that have been introduced to SFG spectroscopy with the advent of ultra short pulse lasers. As in their homodyned counterpart[71] a broadband pump pulse, usually in the IR frequency range, is overlapped with a frequency narrowed upconversion pulse in the visible range. Both beams are focused as well on a reference material to generate the LO and the sample to generate the signal SFG (see figure 2.4B). The total detected SFG intensity yields,

$$\begin{aligned} I_{SFG}(\omega) &\propto |E_S(\omega) + E_{LO}(\omega)e^{i(\omega\Delta t))}|^2 \\ &\propto |E_S(\omega)|^2 + |E_{LO}(\omega)|^2 + [E_S^*(\omega)E_{LO}(\omega)e^{i(\omega\Delta t)} + c.c.] \end{aligned} \qquad (2.33)$$

where the delay Δt of the LO with respect to the sample SFG is typically in the order of 1-3 ps [59,92,93] and will cause interference fringes in the frequency domain spectrum. This delay is necessary to unambiguously separate the two cross terms which maintain the phase information on the samples effective susceptibility $\chi_{eff;S}^{(2)}$ from the square terms, where this phase information is lost. Inverse Fourier transforming this spectrum into the time domain will

yield a pulse around $t = 0$ for the sum of the squares of the total electric field. The pulses of the two cross terms between the sample SFG and the LO will be present around $\pm\Delta t$. Application of a suitable window function allows to pick either pulse around $\pm\Delta t$ which can then be transformed back into the frequency domain. Dividing the result by a reference spectrum with known phase and amplitude response yields the phase-resolved spectrum.[59] Since the beams are applied in a non-collinear fashion the LO can independently be delayed with respect to the sample signal by either using a delay stage[92] or introducing some dispersive optic exclusively into the LO beam path (or the sample signal beam if the positions of the sample and the LO are reversed).[59] Compared to the scanning technique the broad band approach has many advantages. For one only two independent measurements are needed to reveal the absolute phase spectrum of a sample instead of eight. Additionally these single measurements are performed in shorter time, since the whole frequency spectrum is monitored simultaneously. Accordingly any phase drifts in the pump and upconversion beams over the course of the experiment which add to a certain uncertainty are minimized.[94] Using short pulses with a high peak intensity also allows to create the strong electric fields at the sample needed to induce a nonlinear polarization with less overall laser power. A significant SFG signal can therefore be generated without a high impact of heat at the sample that could change the sample structure due to damage during the measurement.

Despite the aforementioned advantages there are some limits concerning the spectral resolution that need to be discussed. In theory the resolution can be arbitrarily enhanced by simply increasing Δt. However, the temporal overlap between E_{LO} and E_{Sig} for increasing Δt is limited by the pulse duration of the applied up-conversion beam. Additionally there are two factors that limit the resolution of the obtained spectra further, namely the detector used in this scheme and the spectral width of the visible upconversion beam. In broad band SFG setups the detector usually consists of a polychromator and a camera. The signal and LO beams typically enter the polychromator via a slit and are reflected by a grating which leads to a loss in intensity. Furthermore since the polychromator fans out the beams according to their different frequency

components their total intensity is distributed over a wide range on the camera chip. A single pixel on the camera thus only experiences a small fraction of this intensity, leading to much weaker signal levels and thus a smaller signal-to-noise ratio.[94] One can tackle this problem by either binning a certain number of pixels thus loosing resolution or by averaging a larger number of pulses thus thwarting the advantage of a shorter acquisition time.

To be spectrally narrow the upconversion beam must be temporally long (in the range of *ps*). However the pump and upconversion beam usually originate from the same Laser source and therefor the visible beam is in the range of *fs* as well. To create the *ps* upconversion pulse from such broadband laser sources the use of spectral filters is required. Different approaches have been reported to tackle this issue among others using a narrow-band filter[59], a pulse shaper[95] or an Etalon[92]. The latter one is also used in the case of the homodyned measurements presented in this thesis (see chapter 4.1). All these approaches have in common that only a small frequency portion of the originally broad band pulse is selected. For economic reason therefore often the residual of an optical parametric amplifier (OPA) which generates the IR pulse is used in the generation of the frequency narrowed upconversion pulse.[96,97] However, in[98] it could be shown, that all of this approaches affect the temporal profile of the upconversion beam differently. Even though they might have the same spectral full width at half maximum two upconversion beams which differ in their temporal profile influence the peak shape of the final SFG spectrum differently, possibly leading to interpretation ambiguities.[98]

2.1.8 Time Domain Heterodyned Vibrational SFG Spectroscopy

Mathematical Description

The need to frequency narrow the upconversion pulse as described in the previous chapter vanishes if the spectrum is measured in the time domain. Therefore a broadband *fs* IR pulse is used to induce the vibrational free induction decay (FID) of the sample (see figure 2.5).[98] An ultrashort visible pulse upconverts a small fraction of the FID. By scanning the time delay t_{IR} between
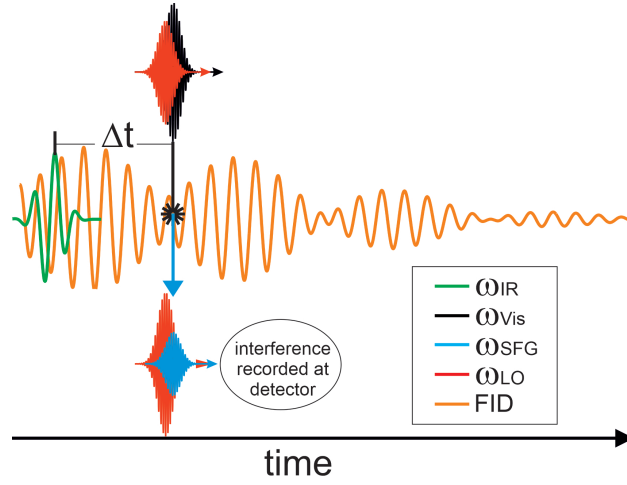
Figure 2.5: Excitation and up-conversion of the vibrational free induction decay (FID).

the visible pulse and the IR pulse the amplitude of the full FID can be recorded using a PMT or photo diode. The electric field of the IR pulse with respect to the upconversion pulse is given as follows.

$$E(\omega_{IR}, t_{IR}) = E(\omega_{IR})e^{i\omega_{IR}t_{IR}} \tag{2.34}$$

The electric field of the sample's resulting time delay dependent SFG response can then be found by inserting equation 2.34 into equation 2.8 (see chapter 2.1.1).

$$E_S(\omega_{SFG}, t_{IR}) = L(\omega_{SFG}) \int_{-\infty}^{+\infty} \mathrm{d}\omega_{Vis}$$
$$\int_{-\infty}^{+\infty} \mathrm{d}\omega_{IR} L(\omega_{Vis})E(\omega_{Vis})L(\omega_{IR})E(\omega_{IR})e^{i\omega_{IR}t_{IR}}$$
$$\cdot \chi^{(2)}(\omega_{Vis}, \omega_{IR})\delta(\omega_{SFG} = \omega_{Vis} + \omega_{IR}) \tag{2.35}$$

33

To get additional phase information a LO pulse with a fixed time relationship with the visible pulse is applied and the heterodyned SFG intensity is recorded as a function of t_{IR}. Just as in the broadband frequency domain case (see equation 2.33) the intensity consists of a square term for both the LO and the Signal and the interference term. Again the latter needs to be separated from the former two. How this can be achieved experimentally will be described in Chapter 3.1.3. The intensity of the remaining interference term corresponds to:

$$
\begin{aligned}
I_{SFG}(t_{IR}) &= \int_{-\infty}^{+\infty} dt \, (E_{SFG;S} \cdot E_{LO}(t)) \\
&= \int_{-\infty}^{+\infty} dt \int_{-\infty}^{+\infty} d\omega_{SFG} \int_{-\infty}^{+\infty} d\omega_{LO} E_S(\omega_{SFG}, t_{IR}) E_{LO}(\omega_{LO}) e^{i(\omega_{SFG} + \omega_{LO})}
\end{aligned}
$$

(2.36)

The only nonzero contributions to the integral over time are those, where the exponent in equation 2.36 vanishes, in other words if $\omega_{SFG} = -\omega_{LO}$. Thus we can introduce a δ-function:

$$
\begin{aligned}
I_{SFG}(t_{IR}) &= \int_{-\infty}^{+\infty} d\omega_{SFG} \int_{-\infty}^{+\infty} d\omega_{LO} E_S(\omega_{SFG}, t_{IR}) E_{LO}(\omega_{LO}) \delta(\omega_{SFG} = -\omega_{LO}) \\
&= \int_{-\infty}^{+\infty} d\omega_{SFG} E_S(\omega_{SFG}, t_{IR}) E_{LO}^*(\omega_{SFG})
\end{aligned}
$$

(2.37)

Inserting the definition of $E_S(\omega_{SFG}, t_{IR})$ from equation 2.35 into equation 2.37 we end up with:

$$I_{SFG}(t_{IR}) = \int_{-\infty}^{+\infty} d\omega_{SFG} L(\omega_{SFG}) \int_{-\infty}^{+\infty} d\omega_{IR}$$
$$\int_{-\infty}^{+\infty} d\omega_{Vis} [L(\omega_{Vis}) E(\omega_{Vis}) L(\omega_{IR}) E(\omega_{IR}) e^{i\omega_{IR} t_{IR}} \chi^{(2)}(\omega_{Vis}; \omega_{IR})$$
$$\cdot E_{LO}^*(\omega_{SFG}) \delta(\omega_{SFG} = \omega_{Vis} + \omega_{IR})]$$

(2.38)

which equals the intensity of the upconverted FID. The such obtained FID can be Fourier transformed to yield the complex frequency spectrum S.

$$S(\omega_S) = \int_{-\infty}^{+\infty} dt_{IR} [\int_{-\infty}^{+\infty} d\omega_{SFG} L(\omega_{SFG}) \int_{-\infty}^{+\infty} d\omega_{IR}$$
$$\int_{-\infty}^{+\infty} d\omega_{Vis} [L(\omega_{Vis}) E(\omega_{Vis}) L(\omega_{IR}) E(\omega_{IR}) \chi^{(2)}(\omega_{Vis}; \omega_{IR})$$
$$\cdot E_{LO}^*(\omega_{SFG}) \delta(\omega_{SFG} = \omega_{Vis} + \omega_{IR})] \cdot e^{i(\omega_{IR} - \omega_S) t_{IR}}]$$

(2.39)

Realizing that the only nonzero contributions to the integral over time require $\omega_S = \omega_{IR}$, we can summarize equation 2.38:

$$S(\omega_{IR}) = \int_{-\infty}^{+\infty} d\omega_{SFG} L(\omega_{SFG}) \int_{-\infty}^{+\infty} d\omega_{Vis} [L(\omega_{Vis}) E(\omega_{Vis}) L(\omega_{IR}) E(\omega_{IR})$$
$$\cdot \chi^{(2)}(\omega_{Vis}; \omega_{IR}) E_{LO}^*(\omega_{SFG}) \delta(\omega_{SFG} = \omega_{Vis} + \omega_{IR})]$$

(2.40)

Thus the frequency axis of the final spectrum corresponds to the IR frequencies. To obtain the absolute spectral phase again a reference spectrum of known phase needs to be recorded.

Comparison with Frequency Domain Techniques

As in the case of the broad band frequency domain approach only two spectra are necessary in this time domain scheme to obtain an absolute phase-resolved sample spectrum. In addition the resolution of the obtained spectra is independent of the spectral width of the upconversion beam but instead can be enhanced arbitrarily by scanning further into the tail of the FID. Since no polychromator is needed there is no limitation to the frequency range detected during the scan. The resolved range only depends on the step size Δt_{IR} of the scanned time delay t_{IR}, with a smaller Δt_{IR} yielding a broader frequency range. However, since more individual t_{IR} steps need to be recorded a higher resolution and a broader frequency range significantly enhance the acquisition time which depends on the number of steps recorded, the number of laser shots averaged at each step, the laser repetition rate and the delay stage's velocity.

2.2 Molecular Switches

Creating surfaces whose macroscopic properties can be switched between two or more states via the application of external stimuli are potentially useful in diverse applications, among others molecular (opto-)electronics,[99–101] membrane filters,[102] and (bio-)electrochemical sensors.[12,14,103–105] The substructure for such responsive surfaces are bistable molecules which are known to change such properties as conformation or dipole moment on external stimuli (e.g. light, pH, temperature) when dissolved in solution. The formidable challenge is to immobilize and orient such molecules on the surface while maintaining their ability to switch. Additionally the use restrictions of the resulting surfaces need to be understood if more than one external stimulus is applied (e.g. light and an electric potential in electrochemical sensors). SFG spectroscopy is predestined to investigate such systems due to its interface specificity (as explained in chapter 2.1.2) and its possibility to detect vibrational resonances. The following chapter shall provide the basis in understanding bistable molecules and their application in smart surfaces.

2.2.1 General Overview

Our life, and biological systems in general, depend on molecular machines that govern multiple essential processes, from small actions such as the opening/closing of cell membranes for mass transport into and out of our cells[106] up to the collective motion of muscles.[107] At the center of these machines are molecules which under the impression of external stimuli such as heat or a change in the surrounding pH value undergo electronical or structural changes such as isomerization. The process of vision as an example is based on the reversible cis→trans isomerization of retinal in the rhodopsin protein located in the eye's retina after being exposed to light of a distinct wavelength.[108] Such molecular switches have been in the focus of synthetic chemists since the early 1980's and their efforts have so far culminated in the award of the 2016 Nobel prize of chemistry to J.-P. Sauvage, J.F. Stoddart and B.L. Feringa "for the design and synthesis of molecular machines".[109]

For their incorporation into smart surfaces three key aspects have to be taken into consideration:[107] how to achieve and influence the reversible molecular transition into two (or more) distinguishable stable states; how to organize the molecules to maintain their ability to switch; and how to turn a microscopic change in one molecule into a collective macroscopic effect which can be exploited.

2.2.2 Bistability in Molecules

The origin of bistability in a molecular system is shown exemplaryly by taking a look at the molecular switch used in our measurements, a spiropyran derivative called 3',3'-dimethyl-6-nitrospiro[2H-1-benzopyran-2,2'-(2H)-indole], commonly called 6-Nitro-BIPS (see figure 2.6A). Spiropyran and its derivatives form a prominent class within the group of molecular switches among others such as Azobenzenes and Dithienylethenes (the general structure of the latter two is shown in figure 2.6 C).[100] This molecular system is bistable in a sense that 6-Nitro-BIPS can exist in a thermodynamic ground state equilibrium between the closed spiropyran (SP) form and the open merocyanine (MC) form. To induce ring opening the molecule needs to be exposed to UV light (see UV-Vis absorp-

tion spectrum in figure 2.6 B) which promotes the molecule into an electronically excited state. In this state the C-O-bond at the spiro-center is weakened and the molecule favors the open MC-form. After relaxation into the electronic ground state the molecule is trapped in the MC-form. The back reaction into the thermodynamically favored SP-form eventually occurs thermally when the reaction barrier is surpassed. An alternative pathway for the back reaction not shown in figure 2.6A via an electronically excited state involves the absorption of a photon with a wavelength in the visible. The molecular transition between the closed and open form is accompanied by a photochromism (see figure 2.6B) which can be understood by looking at the molecules respective structure. In the closed form the benzopyran and indoline substructures host two separate π electron systems which are orthogonally oriented. Upon ring opening the molecule becomes planar and the formally orthogonal π orbitals of the previously separated π electron systems can now overlap to form one extended delocalized π electron system which can be excited with photons of less energy.

While photochemical switching is advantageous since light as a stimulus can be applied with high spatial and temporal precision and is noninvasive[110] different stimuli play an additional role in the SP→MC transition of spiropyran derivatives, which can influence their possible use in specific areas of application and need to be investigated. The relative position of the electronic energy levels of the SP and MC-form depends on the molecule's environment which consequently enhances or attenuates the ability to switch from one state into the other. Since one contributing structure of the MC-form is zwitterionic as shown in figure 2.6 its dipole moment is much larger due to charge separation than the one of the SP-form (14-18 D vs 4-6 D[111]). Accordingly polar solvents stabilize the MC-form up to the point where it is thermodynamically favorable.[112] Additionally protonation of the former spiro-oxygen and hence the surrounding pH value,[113,114] the presence of metal cations[111] and, if the molecule is immobilized at a surface or a polymer chain, the application of mechanical stress[115,116] or applying an electric bias[117] potentially influence the equilibrium between the two states[111] and act as stimuli for switching.
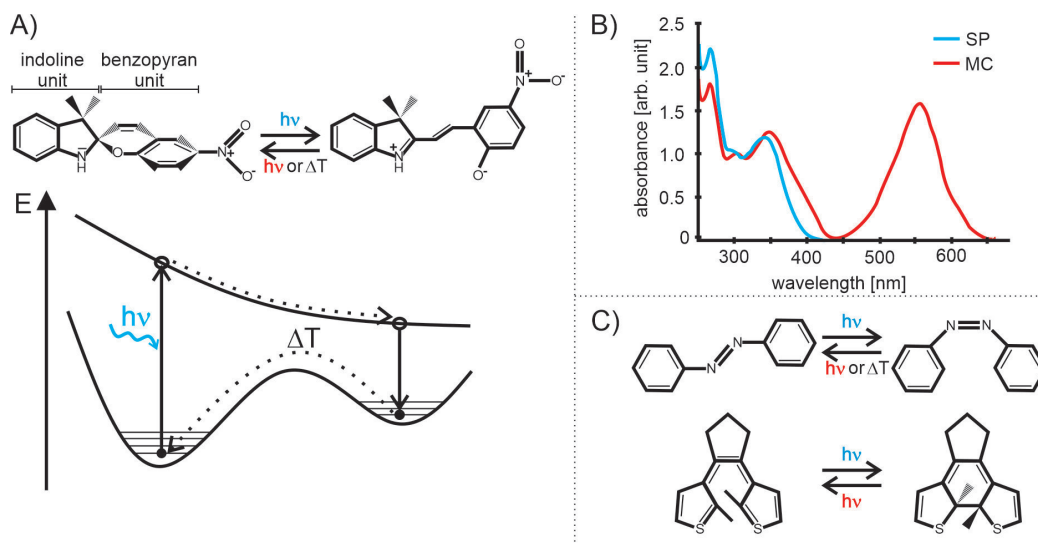
Figure 2.6: A) Open and closed form of the spiropyran derivative 6-Nitro-BIPS and schematic energy diagram of open SP- and closed MC-form. B) UV-Vis spectrum of SP- and MC-form which displays photochromism of 6-Nitro-BIPS. C) Stilben (upper) and Dithienylethene (lower) as additional examples of bistable molecules.

2.2.3 Arranging Molecular Switches

Bistable molecules, that reversibly change their properties, e.g. dipole moment, size, absorption(see figure 2.6B) and vibrational spectrum, under various stimuli (that can be independently applied) have been described in the previous section. However, to be ultimately used in responsive materials and smart surfaces the molecules need to be organized so that a microscopic change of their properties can be translated into a macroscopic change of the material's properties e.g. surface wettability.[118] Additionally the desired immobilization prevents leaching so that the bistable molecules are not washed away during their use,[119] and it leads to an improved processability where e.g. the substrates mechanical properties can be exploited.[111] Furthermore in case of the spiropyran it excludes the formation of dimers thus preventing the major source of photodegradation via the bimolecular pathway.[111,120,121]

To achieve immobilization of the molecules two strategies are commonly employed. In the first strategy the molecules are attached to a polymeric back-

bone.[122,123] This process is controlled by certain functional groups in the polymer which will react with distinct sites in the molecular switch and whose distance in the polymer can be precisely adjusted by the choice of the precursor monomer unit. The second strategy exploits attractive and repulsive forces in between the molecular switches itself as well as with the substrate that can ultimately lead to the formation of supramolecular structures and self-assembled monolayers (SAM) on substrate surfaces.[124] However the distance between the molecular switches as a result of self assembly is much harder to be controlled and they might loose their ability to switch due to sterical hindrance from neighbor molecules. Additionally molecule substrate interaction especially for metal surfaces might quench intermediate excited states or extensively favor one form over the other further limiting the switching process.[125,126] One strategy to counter these problems is the introduction of bulky substituents that act as spacer units to isolate the switchable moieties from both neighboring molecules and the substrate. These substituents also typically work as anchor groups to covalently attach the molecules to the substrate and thereby enhancing the stability of the SAM.

We followed the same strategy as was outlayed by Darwish et all. in[127] and used a 6-Nitro-BIPS headgroup which is attached via its nitrogen atom to a spacer chain which possesses a dithiolane group as an anchor group that easily binds to gold as a substrate (see figure 2.7). Gold has a high affinity towards sulfur[128] but is otherwise inert e.g. against oxidation with O_2 under ambient conditions and therefore can be handled outside ultra high vacuum conditions. Additionally it can easily be obtained either as a thin film or as colloids and is non-cytotoxic. Hence gold is an often used substrate and thiolates on gold make up the historically most studied SAMs.[128]

2.2.4   Exploiting a Microscopic Change on a Macroscopic Scale

With our molecules attached to gold as seen in figure 2.7 and arranged in SAMs we meet the second key aspect since in these SAMs switchability is maintained as shown in[127]. Now we can address the final aspect how to exploit a macroscopic change within our system after collectively switching individual
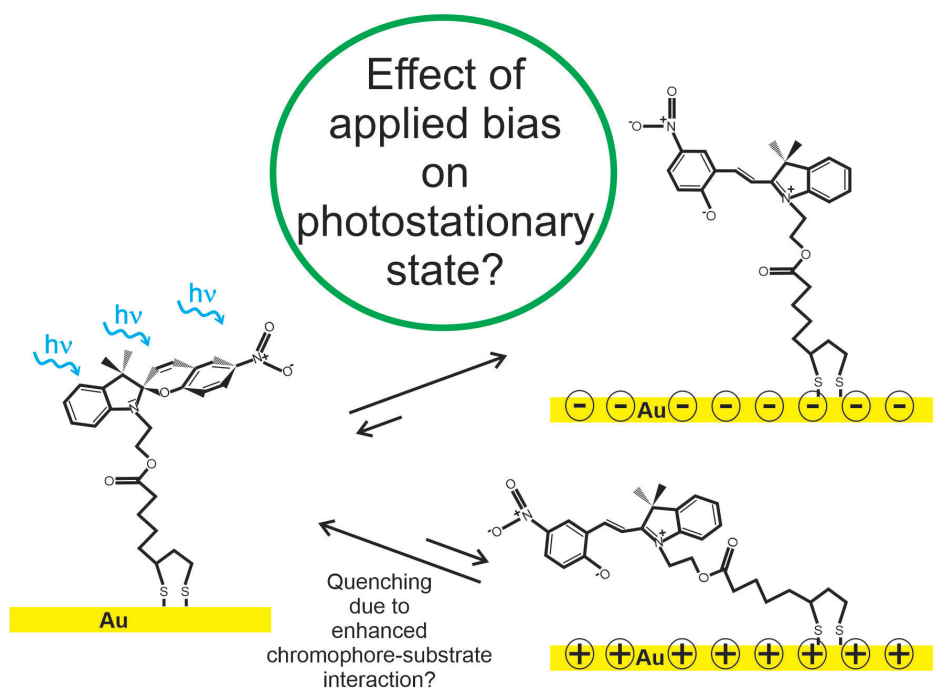
Figure 2.7: SP-LA attached to a gold electrode. Understanding the influence of an applied electric potential on the switching behavior of SP-LA is one goal of this thesis.

molecules. The modified gold film could be used e.g. as an electrode. Katz et all. have found a change in the capacity current of a gold electrode modified with a SAM which contained 6-Nitro-BIPS as headgroups upon switching from its closed SP to its (protonated) MC-form.[129] Willner et all.[14] have used a Spiropyran derivative with one additional Nitro group compared to 6-Nitro-BIPS (in *ortho*−position with respect to the spiro-oxygen) as a headgroup in a SAM which in the SP-form could interact with an antibody whereas in the MC-form it could not due to sterical repulsion. The antibody being bulky blocks a huge area of the electrode thus hindering the electrochemical reaction of an additional redox probe present in the solution. The strength of the system's amperometric response depends on the unblocked area of the electrode and therefore on the antibody's concentration in solution making such electrodes suitable for antibody sensing (down to an antibody concentration in the nano-molar range[13,14]). Afterwards the (macroscopic) electrode could be switched

"off" with the help of UV light converting the SAM molecules into their MC-form and consequently removing the antibody. Such "on/off"-switchable sensors are attractive because in the "off"-state the background signal can easily be quantified and the analyte can be washed off enhancing the re-use of the sensor.[13,14]

The SAM characterization in these sensor studies is usually based on cyclic voltammograms to determine the range in which no electrochemical reaction damages the SAM. However well before damage happens the molecules within the SAM might reorient due to an applied bias thus already inhibiting sensing (see figure 2.7). To reveal the orientation and conformation of the molecules during the switching process in the presence of an applied potential a surface specific in-situ method e.g. vibrational SFG spectroscopy is needed. Since we are also interested in the molecules' absolute orientation (e.g. specific functional groups pointing up/down) which is not accessible with conventional homodyned SFG (see chapter 2.1.6) phase-resolved SFG spectroscopy has to be applied. Such measurements, however, have so far not been applied to the electrode/electrolyte interface. The aim of this thesis is to overcome these limitations.

Chapter 3

High Accuracy Heterodyned SFG Measurements

In the theory section 2.1.7 two approaches were presented, that have been implemented in the frequency domain of Heterodyned SFG spectroscopy. Within a collinear setup[55,130,131] (see figure 2.4A) two narrowband pulses need to be applied and the frequency of the incident IR pulse has to be scanned over the course of the measurements. However, the typical drift of laser pulses and the accompanying significant changes in their intensities and spectra over time introduces phase and amplitude uncertainties in the obtained SFG spectra.[94] Additionally all beams being overlapped in space and time not only at the sample but on common optics (though not focused there) can introduce unwanted spectral interference from background SFG. Finally the experiment as described is time consuming since 8 scans have to be conducted to gain absolute phase information. In contrast only 2 scans have to be taken in the non-collinear broadband approach[59,92,132] (figure 2.4B). No background SFG is expected and since all involved IR frequencies are incident at once at the sample, the accuracy is less affected by pulse drifts. However, the nonlinear beam geometry makes the phase and amplitude of the generated SFG signal sensitive to the sample position so switching to a reference for absolute phase information again will introduce inaccuracies.[57]

To combine the advantages of both geometries and ultimately extend phase-

resolved SFG spectroscopy to the solid/liquid interface a collinear time domain broadband SFG approach is applied. This chapter will introduce its working principle and show its practical implementation into the measurements at buried interfaces.

3.1 Collinear Heterodyned Time Domain SFG

3.1.1 General Advantages

A collinear phase-resolved broadband time domain SFG setup has a number of advantages compared to non-collinear approaches either in the frequency domain[59,92,132] or time domain.[98] For one the phase relationship between the involved pulses is much improved since all beams travel along the same path.[38] In non-collinear setups the spacial separation of the visible, IR and LO pulse strongly reduces the phase stability of the interferometer due to vibrations and drifts of optics leading to phase drifts which can severely distort the resulting complex spectra.[38,94] This phase instability can be reduced by using common optics for all three beams such as a concave mirror as shown in figure 2.4 A which focuses all beams simultaneously onto the sample.[132] However, using common optics strongly reduces the degrees of freedom for the alignment of the three beams onto the sample. The pump and upconversion beams need to be spatially overlapped both at the nonlinear crystal to generate the LO and at the sample to generate the signal pulse. The LO on the other hand needs to be reflected at the sample such that it travels collinearly with the signal pulse towards the detector. Matching these requirements simultaneously represents a serious experimental challenge. Furthermore this tiresome alignment needs to be repeated if the wavelength of any of the incident pulses is changed since the emission angle for the signal is frequency dependent according to the phase matching condition of the SFG process,[40]

$$n_{SFG}\omega_{SFG}sin(\Theta_{SFG}) = n_{Vis}\omega_{Vis}sin(\Theta_{Vis}) \pm n_{IR}\omega_{IR}sin(\Theta_{IR}) \qquad (3.1)$$

with n_i the refractive index of the medium through which the respective pulses with frequency ω_i travel. Θ_i are the respective incident angles and the sign ($\pm$)depends on the geometry (+ for co-propagating beams). For ultra broadband pulses there is no suitable alignment at all.

Finally for absolute phase measurements it is critical that upon changing the sample of interest to the reference sample no additional phase uncertainty is introduced which depends on the exact positioning of the sample. However in the non-collinear geometry the relative phase of the LO and signal pulse is sensitive to the sample height, thus impeding the determination of the absolute phase and also lowering the comparability of the results from different samples in general.

The collinear geometry does not suffer from the described shortcomings but exhibits improved phase stability, a largely simplified alignment and high phase reproducibility,[38,130,131] which is why for the subsequent measurements a collinear time domain phase sensitive spectrometer is used.[94]

3.1.2   Working Principle

A schematic representation can be found in figure 3.1. In short the SFG signal and LO pulses are created by nonlinear mixing of two ultrashort pulses, the pump pulse in the IR frequency range (ω_1) and the upconversion pulse centered at $800\,nm$ (ω_2). The upconversion pulse thereby consecutively passes a z-cut quartz waver that acts as the nonlinear crystal (NLC) at which the LO is generated and the sample (S). At this two positions the $800\,nm$ upconversion pulse is collinearly overlapped with individual portions of the pump pulse using two custom-made incoupling optics (ICO) which are transparent in the IR. These two portions are obtained by the use of a beamsplitter (BS). Finally the pump and upconversion pulses are filtered and the interference between the SFG signal and LO is detected. An interferogram is recorded by time delaying the upconversion pulse with respect to the second portion of the pump pulse and thus by modulating the carrier envelope phase (CEP) and amplitude of the SFG signal with respect to the CEP of the LO while the SFG signal and LO temporally overlap to maximize the interference amplitude.[98] The resulting
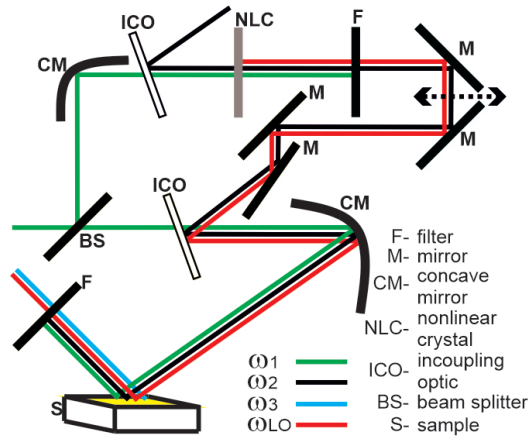
Figure 3.1: Schematic representation of the collinear time domain SFG spectrometer used in the phase sensitive measurements.

interferogram is Fourier Transformed to obtain the complex SFG spectrum.

Due to the collinearity in our experimental geometry which leads to enhanced phase stability the spectrum becomes insensitive to small changes in the common beam path of the three pulses. As a result this allows the introduction of an oscillating mirror into the beam path between the last concave mirror and the sample. This mirror oscillates at half the Laser's repetition rate so every other shot is sent to a second spot at the sample position.[94] Placing a reference sample with known phase into this second spot allows us to perform phase-resolved SFG measurements with quasi simultaneous referencing. Thus a single experiment is enough to obtain both a sample and a reference spectrum without the necessity to exchange the sample by the reference in a second scan.[94]

3.1.3 Balanced Detection

In the following the detection part after the sample is described. As already discussed in chapter 2.1.7 the detected intensity I_{Het} of the sum of the electric fields from the generated SFG signal E_{Sig} and the LO E_{LO} can be split into three summands according to equation 2.33, of which only the cross term be-
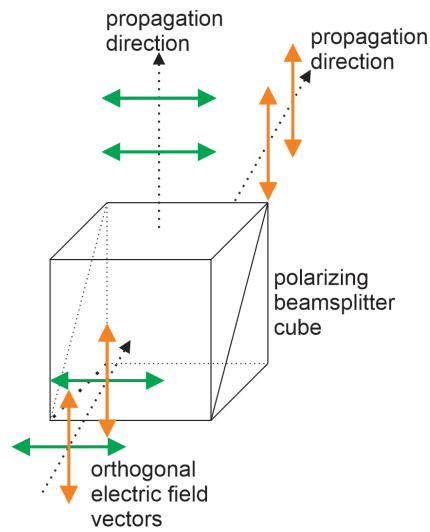
Figure 3.2: Separation of orthogonal polarized electric fields with the help of a polarizing beamsplitter cube.

tween the two fields yields phase information about the generated SFG field. However, usually the electric field of the LO is much stronger than the generated SFG field and hence the square term $|E_{LO}|^2$ will dominate I_{Het}. This term will consequently not only obscure the desired cross term but will also be a major source of noise.[133] Therefore it needs to be suppressed. For the case of frequency domain as discussed in chapter 2.1.7 this is achieved by time delaying the LO with respect to the SFG signal and using inverse Fourier Filtering.[38,57,131]

In the applied scanning time domain approach this is, however, not possible. To get rid of the square terms here we apply a balanced detection scheme[94,133,134] as shown in figure 3.2. Within this scheme the LO and SFG signal must be set to orthogonal polarizations. The such polarized pulses are sent to a beamsplitter cube which is oriented at 45°with respect to the electric field vectors. The two outputs of the cube can be detected independently on two photo-detectors with the detected intensities according to:

$$|E_{Sig;y} + E_{LO;y}|^2 = |E_{Sig} sin(\frac{3\pi}{4}) + E_{LO} sin(\frac{\pi}{4})|^2$$

$$= \frac{1}{2}|E_{Sig}|^2 + \frac{1}{2}|E_{LO}|^2 + Re(E_{Sig} * E_{LO})$$

$$|E_{Sig;x} + E_{LO;x}|^2 = |E_{Sig} cos(\frac{3\pi}{4}) + E_{LO} cos(\frac{\pi}{4})|^2 \tag{3.2}$$

$$= \frac{1}{2}|E_{Sig}|^2 + \frac{1}{2}|E_{LO}|^2 - Re(E_{Sig} * E_{LO})$$

The only difference for the detected intensities at the two photodetectors according to equation 3.2 is the sign of the cross term. Accordingly by subtracting the two intensities from each other we obtain exclusively twice that cross term since the squares simply cancel each other. With this scheme improvements of one order of magnitude in signal-to-noise ratio are easily possible.[94]

3.2 Pulse Timing Control in Collinear Setups

Despite the advantages of collinear spectrometer designs as discussed in the previous chapter there is one major challenge that has limited the applicability of such setups so far, namely the control of the individual pulses' timings. Every dispersive optic which might appear in the common beam path, e.g. a window to seal the sample, will introduce different group velocity delays (GVDs) depending on the pulses' respective frequency. This situation is illustrated in figure 3.3B. The introduced GVD between the local oscillator pulse at the SFG frequency and the visible upconversion beam leads ultimately to a time difference between the LO and the SFG sample signal, so that their interference in the detection area is diminished as opposed to the situation where they coincide in time (figure 3.3A).

In the collinear broadband frequency domain approach, where one typically applies an upconversion pulse with a duration time in the range of *ps* to *ns* a such introduced time delay, usually in the range of *fs*, is less critical. Here different parts of the upconversion pulse will overlap with the ultrashort pump
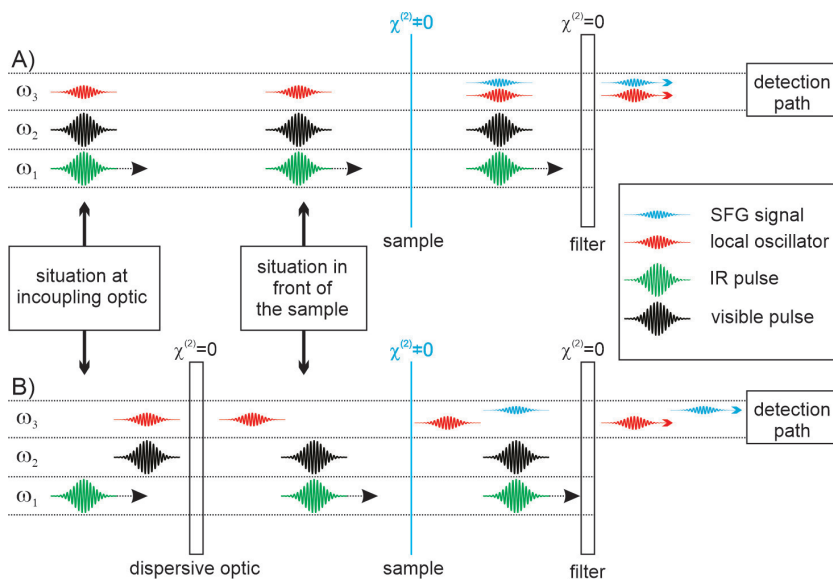
Figure 3.3: Time delay between local oscillator and sample SFG signal due to dispersive optic, e.g. window cover.

pulse to generate the LO and the SFG respectively, at most influencing the final spectral shape of the complex spectrum. In the collinear time domain approach on the other hand both pulses are ultrashort and a perfect overlap is more critical. The adjustment of the overlap between the pump and upconversion pulse in the spectrometer can be achieved using a delay stage (compare figure 3.3A and B, and see figure 2.4 for the schematic setup), since we are measuring an interferogram as a function of time delay anyway (see section 3.1.2). However, upon passing a dispersive optic the LO and upconversion pulse (and ultimately the LO and SFG pulse) will be separated in time. To maximize the interference amplitude SFG signal and LO pulse must be timed up.[135] Ideally this time compensation happens exclusively in the detection beam path where the presence of the IR and Vis pulse is no longer required and hence their phase will not be affected.

Both the SFG signal and LO pulse exhibit the same frequency and co-propagate collinearly, but to be addressed independently the pulses need to differ in at least one property. As was discussed previously in chapter 3.1 E_{LO} and E_{Sig} should be polarized orthogonally to profit from balanced detection. Supposed

orthogonality holds we can change the pulses' relative timing implementing a birefringent crystal[136] as will be shown in the following. Note that although the scheme is discussed for the implementation into our SFG setup it is a general approach that can very well be transferred to any collinear nonlinear interferometric technique were timing needs to be precisely controlled.[135]

An electromagnetic wave which travels through a bulk material experiences a refractive group index n_g which is a material property and a function of the wave's frequency ω. Taking c as the speed of light in vacuum the corresponding time T the wave takes to cover a certain distance l in this bulk can be calculated by

$$T = \frac{n_g(\omega)l}{c} \tag{3.3}$$

The distance l depends on the bulk thickness d, the wave's angle of refraction α' and for the general case of anisotropic material also on the waves polarization. In the specific case of a uniaxial birefringent crystal with ordinary (o) and extraordinary (e) optical properties l is given by

$$l_{o,e} = \frac{d}{\cos(\alpha'_{o,e} + \rho_{o,e})} \tag{3.4}$$

The walk-off angle ρ in equation 3.4 accounts for the mismatch between the Poynting and wave vector in anisotropic media.[137] For the ordinary wave ρ is always zero. For the extraordinary wave on the other hand ρ can be calculated according to equation 3.5[136] using the ordinary and extraordinary phase refractive indices $n_{p,o}$ and $n_{p,e}$ respectively as well as the angle δ which represents the crystal cut angle as defined in figure 3.4.

$$\tan(\rho) = \frac{\sin(\delta + \alpha'_e)\cos(\delta + \alpha'_e)(n_{p,o}^2 - n_{p,e}^2)}{n_{p,o}^2 \sin^2(\delta + \alpha'_e) + n_{p,e}^2 \cos^2(\delta + \alpha'_e)} \tag{3.5}$$
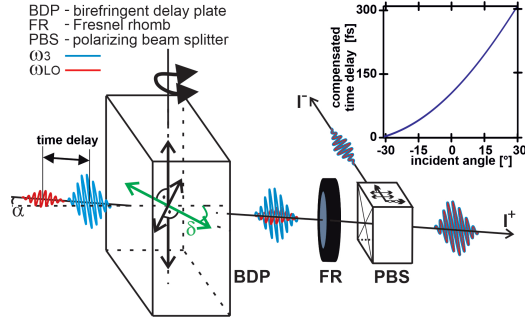
Figure 3.4: Working principle of the time delay compensation unit. The orthogonally polarized LO and Signal pulses (red and blue respectively) of same frequency pass a birefringent crystal which introduces a variable time delay (or compensates if the time delay is negative) between the pulses which can be varied as a function of the incidence angle α. δ represents the angle between the surface normal and the optical axis (green). The Fresnel rhomb turns both beams' polarizations by 45° and the polarizing beamsplitter projects the polarizations onto a horizontal and a vertical axis to achieve balanced detection.[94,98] The so compensated time delay as a function of incidence angle ($d_{Calcite} = 1\,mm$, $\delta = 25°$, $\lambda_{SFG} = 645\,nm$) is shown in the graph at the upper right corner.

Via Snell's law (equation 3.6) the refractive angle α' is obtained as a function of the incidence angle α.

$$(\alpha'_{e,o}) = \sin^{(-1)}(\frac{\sin(\alpha)}{n_{p;e,o}(\omega)}) \tag{3.6}$$

Pulses coming with an electric field orthogonal to the optical axis (OA) such as e.g. the depicted nonlinear signal pulse in figure 3.4 experience a phase refractive index $n_{p;o}$ that solely depends on the pulses frequency. The extraordinary pulse in contrast, whose electric field lies in the plane defined by the wave vector and the OA (the LO pulse in figure 3.4), will experience an effective phase refractive index $n_{p;eff}$ which in addition depends on the refractive angle according to[138]

51

$$n_{p,eff} = \frac{n_{p,o} n_{p,e}}{\sqrt{n_{p,o}^2 \sin^2(\delta + \alpha_e') + n_{p,e}^2 \cos^2(\delta + \alpha_e')}} \qquad (3.7)$$

After combining equation 3.6 and 3.7 $n_{p;eff}$ can be determined as a function of incidence angle α. If the cutting angle δ takes a value other than zero a simultaneous solution of equation 3.6 and 3.7 can only be obtained numerically. The result can be inserted into equation 3.6 to calculate the actual α_e'. α_e' and α_o' are used to calculate the individual transit times for the two pulses through the bulk material with the help of equation 3.3 and 3.4. The effective group refractive index required in equation 3.3 is the material constant $n_{g;o}$ for the ordinary wave while the corresponding value for extraordinary wave can be calculated in a similar manner as the effective extraordinary phase refractive index. The difference is, that now the respective values for the ordinary and extraordinary group refractive indices $n_{g;o}$ and $n_{g;e}$ must be applied. So equation 3.7 becomes:[138]

$$n_{g,eff} = \frac{n_{g,o} n_{g,e}}{\sqrt{n_{g,o}^2 \sin^2(\delta + \alpha_e') + n_{g,e}^2 \cos^2(\delta + \alpha_e')}} \qquad (3.8)$$

In a last step one has to take into account the additional distance that the ordinary ray travels outside the birefringent crystal en route to the detector compared to the extraordinary ray due to the difference in their respective refracted angles.[138]. The thus caused extra time T_{ex} is given by:

$$T_{ex} = \frac{1}{c}((\tan(\alpha_e' + \rho) - \tan(\alpha_o'))d \sin \alpha) \qquad (3.9)$$

The introduced or as the case may be compensated overall time delay via the birefringent crystal ΔT then is calculated according to equation 3.10

$$\Delta T = T_o + T_{ex} - T_e \qquad\qquad (3.10)$$

The graph in figure 3.4 depicts calculated values for ΔT as a function of incidence angle α. To perform this calculation a 1 mm thick calcite crystal with a cut angle δ of 25° and a wavelength of 645 nm was assumed which corresponds to our experimental parameters for measurements in the vibrational CH-stretch region around $3000\,cm^{-1}$ if an $800\,nm$ upconversion beam is used. The graph clearly shows that such a birefringent crystal can indeed be applied to smoothly vary the relative time delay between the LO and the nonlinear signal pulse over hundreds of femtoseconds. Larger delays can be easily obtained using a thicker crystal or to some degree by modifying the cut angle δ. So this versatile method is not restricted to the time domain case but also applicable for a possible collinear broad band phase-resolved frequency domain SFG setup, where a *ps* time delay between LO and SFG signal needs to be introduced (see also chapter 2.1.7).

In the beginning of this chapter it was argued that this time delay compensation method was chosen, because we wanted to apply a balanced detection scheme to reduce noise and hence the beams polarization was assumed to be orthogonal. However, it is worth mentioning that this balanced detection scheme is also a necessity for this compensation approach to be implemented in phase-resolved SFG setups. While indeed the birefringent crystal adjusts the pulses' relative timing, only the balanced detection scheme projects the in the crystal necessarily orthogonal pulses onto two new common polarization axes at which they can interfere with each other. The birefringent crystal and the balanced detection scheme should accordingly be viewed as an inseparable unit in the aim of pulse timing control.

3.3 Flexibility in the Linear Polarization of the Local Oscillator

The pulse delay control scheme which was outlined in the previous section has an important requirement. It is necessary for the LO pulse to be linearly polarized. In principal the balanced detection scheme acts as a polarization filter to the signal wave. Any field component parallel to the polarization of the LO will vanish after taking the difference of the measured intensities at the two detectors. To have full flexibility in measuring any desired SFG polarization combination therefore one needs an easy way to tune the LO independent of the pump and upconversion beams' polarization.

In our setup this is achieved by using a thin z-cut alpha-quartz crystal for LO generation, placed at normal incidence into the beam path of the collinear IR and Vis pulses. Alpha quartz possesses a non inversion symmetric crystal structure, d3 symmetry,[139] and thus a nonlinear bulk signal which will act as the LO can be generated. The LO's polarization depends on the polarization of the incident beams. For a z-cut alpha-quartz crystal with collinear pump and upconversion beams passing the crystal at normal incidence the transmitted second order signal can be calculated using the methods described in[140] to be of the following form for parallel (3.11 a) and orthogonal (3.11 b) incident pulses:[135]

$$\vec{E}_{LO} \propto (cos(3\Phi) * \vec{e}_x + sin(3\Phi) * \vec{e}_y) * \chi^{(2)}_{xxx} \tag{3.11a}$$

$$\vec{E}_{LO} \propto (sin(3\Phi) * \vec{e}_x - cos(3\Phi) * \vec{e}_y) * \chi^{(2)}_{xxx} \tag{3.11b}$$

Φ represents the angle between the x-axis in the crystal- and the x-axis in the laboratory frame and $\vec{e}_x$ and $\vec{e}_y$ are the two unit vectors along the x- and y-axis in the latter one. The only nonzero tensor component of the alpha-quartz' second order susceptibility is $\chi^{(2)}_{xxx}$. As is evident from equation 3.11 a and b regardless of the incident beams polarization the LO will always be linearly polarized with a constant intensity independent of Φ. Furthermore the LO's polarization can be continuously adjusted by rotating the quartz along its surface normal.

The intensity and the spectral shape of the generated LO will not only depend on the effective second order susceptibility of the alpha-quartz but also on its thickness L. Due to the necessity to have the pump beams pass the quartz crystal along its z-axis it is not possible to achieve any kind of phase matching for the LO generation. Due to dispersion between the incident pulses and the generated LO its intensity only builds up over a short distance inside the crystal, defined by the coherence length L_c, to subsequently decrease again in an oscillatory fashion accompanied by increasing modulations in the LO spectrum. The thickness of the quartz crystal should therefore not exceed L_c. Latter can be derived from the wave vector mismatch Δk [65]

$$L_{coh} = \frac{2}{\Delta k} \tag{3.12}$$

The coherence length is typically in the range of 10-50 μm. A very thin quartz crystal is thus required to maximize the LO output and to avoid the appearance of distortions in the LO spectrum.

3.4 Applicability of the Collinear Time Domain SFG spectrometer

3.4.1 Suppression of Background SFG

In the following section two examples will be discussed that demonstrate how the implementation of the pulse timing control scheme presented so far in chapter 3 into the collinear time domain SFG spectrometer opens the possibility to measure phase-resolved SFG spectra of buried interfaces and can enhance the quality of collinearly obtained SFG spectra by suppressing unwanted background SFG signals.

The problem of unwanted background SFG (BSFG) signals which interfere with the sample SFG and distort the acquired phase information has been briefly mentioned in the beginning of this chapter. Along with the complicated pulse timing control this BSFG often is one factor of favoring the non-collinear approaches over the collinear one, despite the aforementioned advantages of the

latter. BSFG can be expected to be present in every collinear SFG measurement originating from all optics' surfaces in the common beam path of the pump and upconversion beams especially using ultrashort broadband pulses with a high peak intensity. However, since the beams are only focused at the sample spot and the NLC for generation of the LO, this background SFG is estimated to be small and therefore usually ignored. With the time control scheme it is possible to separate BSFG from the sample SFG and ultimately suppress it. To illustrate this problem and its final solution four measurements of the non-resonant SFG response of a z-cut alpha-quartz sample which were consecutively taken (see figure 3.5) will be discussed.

Figure 3.5A shows the common case of phase-resolved collinear SFG measurements. After the LO is generated (not shown in the figure) it coincides in time with the driving pulses. On their way towards the sample they pass a couple of optics with a nonzero second order susceptibility, at which BSFG is generated. After the generation of the sample SFG the driving pulses are filtered out. Due to our balanced detection scheme only BSFG with orthogonal polarization to the LO and therefor with the same polarization as the sample signal will contribute significantly to the background noise (since the crossterm between the orthogonally polarized BSFG and the sample SFG is much smaller than the respective LO crossterms). The detected interferogram then contains the interference term of the sample SFG and the LO as well as the term of the LO and the BSFG of unknown magnitude.

A possible way to distinguish both terms outlined in figure 3.5B is the introduction of a fused silica plate at normal incidence into the beam path directly in front of the sample spot. While in this scenario the driving pulses overlap in time at the guiding optics they do not simultaneously overlap in time at the sample due to group velocity dispersion (GVD). This temporal separation of the pump and upconversion pulse leads to a suppression of the sample SFG. The LO and BSFG on the other hand posses the same frequency and as a result experience the same GVD in the window. The interferogram obtained with this experiment thus only shows the isolated BSFG contribution. As expected the amplitude of the BSFG contribution in the interferogram in figure 3.5 B is much smaller than the amplitude of the overall signal in figure 3.5A. Its ra-
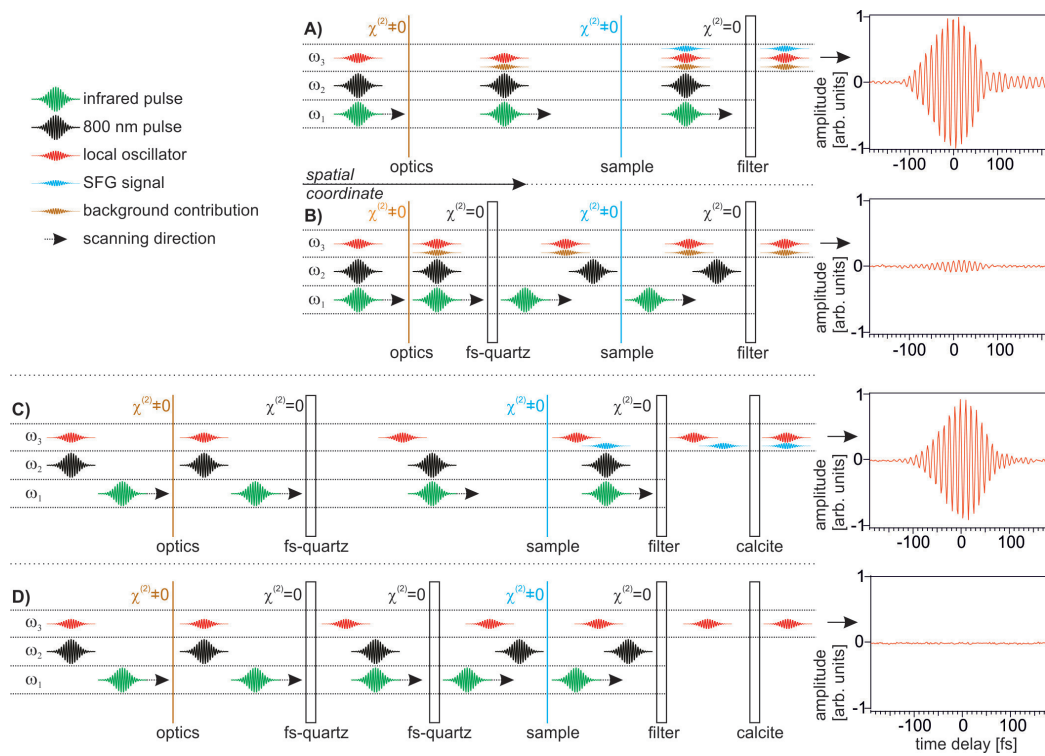
Figure 3.5: Analysis and suppression of background SFG contributions. A) Common interferogram as obtained in our collinear setup, acquired under PPP polarization combination. B) The dispersion of a quartz plate introduced in front of the sample separates the IR and 800 nm pulse in time. Consequently the generation of sample signal is suppressed. The residual SFG can be attributed to background SFG. C) The pump pulses are delayed with respect to each other to compensate for the dispersion. They again overlap in time at the sample position. The resulting timing mismatch between the LO and the sample signal is compensated by inserting and adjusting the calcite crystal. D) Control experiment. A second fs quartz plate is introduced into the beam to eliminate the sample signal. All interferograms are normalized to the one shown in A).

tio with respect to the sample SFG is roughly 1:10. Taking into account that the sample signal originates from the relatively strong non-resonant bulk response of alpha-quartz its size is in fact significant. One can easily imagine a scenario in which a sample with a much weaker nonlinear response is investigated so that the relative size of the background contribution with respect to

the now smaller sample SFG is increased up to the point where the resulting interferogram is dominated by the BSFG. The considerable size of the BSFG is also remarkable taking into account the extensive precautions which had been taken to avoid this contribution while developing the spectrometer, among others keeping reflection angles close to normal incidence and a careful choice of the material of the installed optics. It can therefore be supposed that BSFG is a source of phase inaccuracies in other collinear phase-resolved SFG studies as well. In fact expected phase shifts and spectral distortions as a result of the interference between the sample SFG and BSFG might have contributed to the lack of reproducibility and a controversial discussion about the interpretation of phase-resolved SFG spectra from the air-water interface taken under collinear[60,63] and non-collinear approaches.[61,62]

In principal we can use the measurement in figure 3.5B to determine the amplitude and phase of the BSFG and subtract the resulting interferogram from the one acquired in 3.5A to yield a background free spectrum. However, to enhance accuracy and save time it is desirable to suppress BSFG during the sample measurement. To achieve this, we keep the fused silica plate that was installed in 3.5B but move the relative pulse delays between the two driving pulses such that they overlap in time not until they passed the fused silica as depicted in figure 3.5C. As a result the generation of any background contribution will be suppressed. Before the fused silica plate, the LO and $800\,nm$ upconversion pulse will coincide in time. After the plate due to GVD the LO will lag behind the upconversion pulse and ultimately behind the signal SFG so that interference between these two will be reduced. Applying the calcite crystal according to the previously described pulse control scheme (see section 3.2) into the beam path compensates for the timing mismatch so that the LO and background contribution free sample SFG pulses coincide in time at the detector. The resulting interferogram is depicted in figure 3.5C with an amplitude comparable to the measurements in figure 3.5A. The successful delay compensation with the calcite plate is thus confirmed.

The scenario in figure 3.5D describes a control experiment. The applied relative time delay between the driving pulses equals the setting in figure 3.5C. In addition to the previously installed fused silica plate, we introduce a sec-

ond one in the same manner in front of the sample. Now both the generation of BSFG and sample SFG should be suppressed. The resulting interferogram accordingly shows no oscillations. Therefore we can conclude, that the BSFG measured in figure 3.5B does not originate from the fused silica plate but indeed from the common optics in the beam path.

3.4.2   SFG spectra of solid/liquid interfaces

The situation described in figure 3.5C is pretty similar to measurements in electrochemical cells. Here the driving pulses need to traverse the electrolyte before reaching the surface. In principal the thickness of the electrolyte layer can be very thin (down to some μm) to minimize introduced GVD, but then evaporation over the cause of the experiment becomes a problem. Typically the cell is covered by a window to prevent evaporation. This window then introduces a time delay between the driving pulses and the LO as does the silica plate in figure 3.5C. Timing up the LO and sample signal with the help of the time control scheme becomes mandatory. To demonstrate this a spectrum of a self-assembled monolayer (SAM) of Octadecanethiol, a widely studied system,[71,132,141,142] was taken covered by a calcium fluoride window and a $25\,\mu m$ layer of deuterated acetonitrile to mimic the situation in our electric cell. The experimental geometry can be seen in figure 3.6A. The SFG for PPP polarization combination spectrum of an ODT SAM on gold in air typically consists of three main spectral features at $\nu \approx 2875\,cm^{-1}$, $\nu \approx 2935\,cm^{-1}$ and $\nu \approx 2962\,cm^{-1}$ which can be related to the symmetric C-H-stretch vibration, its Fermi resonance and the asymmetric C-H-stretch vibration respectively of the terminal methyl group.[141] Typically these features appear as dips in the spectrum. Depending on the SAMs quality gauche defects in the molecular chain lead to the appearance of two additional peaks at $\nu \approx 2850\,cm^{-1}$ and $\nu \approx 2900\,cm^{-1}$ related to symmetric and asymmetric C-H-stretch vibrations of methylene groups.[141]

Figure 3.6B shows the magnitude spectrum of the ODT SAM inside a liquid cell with (black) and without (green) compensation for the GVD introduced mainly by the window. The delay compensated spectrum nicely shows the
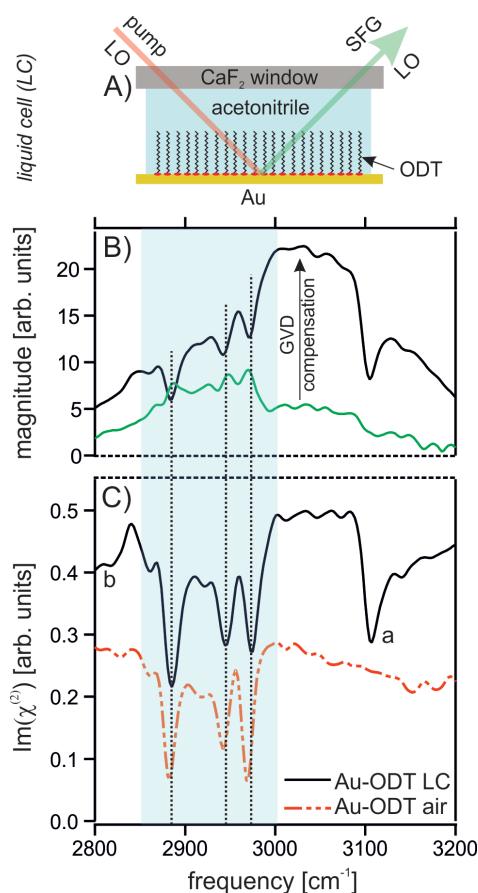
Figure 3.6: Phase- resolved SFG measurements of Au-ODT in a liquid cell filled with acetonitrile. Spectra acquired under PPP polarization combination: A) schematic experimental configuration, B) raw magnitude SFG spectra of Au-ODT under acetonitrile with (black line) and without GVD compensation (green line). C) Imaginary parts of $\chi^{(2)}$ for the sample under acetonitrile (black line) and in air (red dotted line, vertically shifted for better visibility). The spectra in C) are corrected for the spectral Gaussian profile of the IR pulse. Dotted black lines indicate peak positions from the ODT response.

three expected dominant resonance dips of the SAM on top of a broad non-resonant background signal originating from the gold substrate which resembles in shape the IR pump beam. The dips related to gauche defects in contrast are small, indicating a well ordered SAM. The magnitude spectrum without GVD compensation on the other hand shows largely diminished spectral features that barely rise above noise level. Additionally the relative phases of this features with respect to the non-resonant gold signal seem to be inverted, so that rather than dips the features appear as peaks in the spectrum. This result emphasizes the necessity for time delay compensation to avoid severe spectral distortions as a result of the timing mismatch between the LO and the SFG signal.

Finally to verify the accuracy of the obtained spectrum and thus evaluate the applicability of our time delay compensation technique we compare the imagi-

nary (absorptive) part of the second order susceptibility for the ODT SAM with the respective imaginary part of the same sample measured against air where no GVD compensation is necessary in figure 3.6C. The comparability of their two spectra is based on the assumption that the well ordered and dense structure of the ODT SAM should for sterical reasons prevent the molecules from changing their orientation or structure when in contact with the liquid. Thus the nonlinear spectral response of the ODT SAM in either case should be similar. Indeed comparing the three main resonant features' line shapes for both measurements in figure 3.6C shows a very close match between both spectra. The most prominent differences, labeled a and b, in the spectrum from the liquid cell appear in frequency regions not associated with the ODT resonances. As shown in figure 7.14 in chapter 7.3.1, in which the ODT spectrum is discussed in greater detail, these features also appear in a control experiment of bare gold under acetonitrile and must hence be attributed to molecular species introduced with the solvent. However, a FTIR spectrum taken of our deuterated acetonitrile does not show a feature that could be related to the peak in b and only a small bulk absorption feature in the region of dip a, whose strength does not justify the huge dip observed in the SFG spectrum. It is therefore concluded, that the observed peaks stem from the solvent related formation of interfacial species that interact with the Au substrate. Although the exact origin of these features remains unknown, however, the good match of the main features related to the ODT shows that we correctly measure the sample. We can conclude, that the timing control technique yields accurate phase-resolved spectra of buried interfaces and can subsequently be used to study electrochemical interfaces whose results will be discussed in chapter 7.

Chapter 4

Experimental

The following chapter describes the experimental details of the homodyned and heterodyned SFG measurements conducted within this thesis. It further describes the sample preparation.

4.1   Homodyned VSFG-Spectroscopy

Homodyned vibrational sum frequency generation (vSFG) measurements are conducted applying two pulsed laser, a broadband infrared (IR) pulse and a spectrally narrow pulse in the visible range, coinciding at the sample in space and time. The resulting output at the frequency equal to the sum of the incident frequencies is monitored. The two incoming pulses are created in a laser system that contains a Ti:Sapphire oscillator (Venteon, Femtosecond Laser Technologies) and a regenerative amplifier (Legend Elite Duo He+ Cryo Pa, Coherent). The regenerative amplifier output is split and one half ($P_{pulse} = 7.5\,mJ$, t_{pulse}=45 fs, f=1 kHz, ν_{center}=800 nm) pumps a commercial optical parametrical amplifier (He-TOPAS, Light Conversion). The resulting signal and idler output is mixed in a non-collinear difference frequency generation (DFG) scheme yielding Gaussian shaped broadband IR pulses (FWHM$\approx$ 300 cm^{-1}, ν_{center}=1390cm^{-1}). The residual of the TOPAS passes an etalon to create a narrow band visible (Vis) pulse (FWHM$\approx$10cm^{-1}, ν_{center}=12500cm^{-1} $\widehat{=}$800 nm). A band pass filter centered at 800 nm removes any higher order
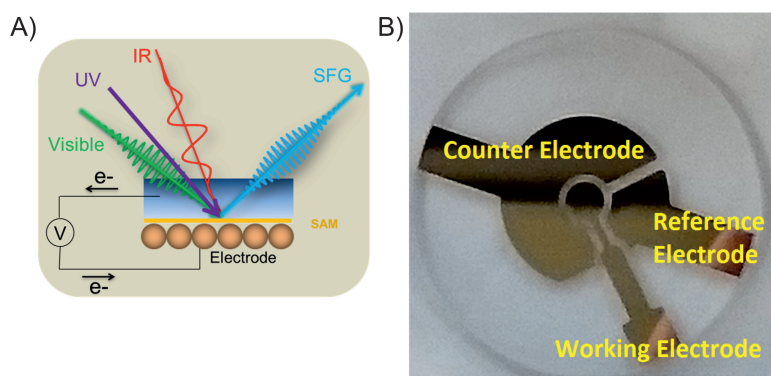
Figure 4.1: A)Schematic representation of homodyned vSFG measurements within our spectroelectrochemical cell. B) Home-build three electrode cell. Both pictures are also shown in our previous publication.[97]

components.

The IR and Vis pulses' polarization and energies each are adjusted with a $\lambda/2$ plate, polarizer, $\lambda/2$ plate combination. The energies are set to $10\,\mu J$ (IR) and $8\,\mu J$ (Vis) per pulse respectively. The pulses are directed such that they travel coplanar in the plane of incidence, each focused onto the sample using a lens with a focal length of $700\,mm$, with incident angles of $40.4°\pm0.5°$ (IR) and $65°\pm0.5°$ (Vis). A schematic setup is shown in figure 4.1A.

The emitted SFG signal from the sample is collimated, passes a polarizer and is ultimately dispersed in a spectrograph (ISA Triax Series 320, HORIBA Jobin Yvon GmbH) to be detected on an emICCD Camera (PI-MAX®4, Princeton Instruments) with an acquisition time of 1 minute per static spectrum or 20 seconds during kinetic measurements. If not stated otherwise all spectra are taken under *ppp* polarization conditions.

To be able to switch between the two photostationary states of the spiropyran derivative arranged in a self-assembled monolayer at our gold sample (see chapter 4.3 for details) we additionally apply a UV laser ($\lambda=355\,nm$, $t_{pulse}=10\,ns$, $f=10\,kHz$, CryLas). To prevent sample damage the pulses' energy was set to $0.1\,\mu J$ using filters.

During measurements the IR beam path is constantly flushed with nitrogen to avoid attenuation due to water vapor absorption. Otherwise the measure-

ments are taken under ambient conditions.

For potential-dependent studies we employ a three electrode cell which consists of three thin film gold electrodes (thickness: $200\,nm$) arranged onto a glass substrate (BK7, $\varnothing = 2$") as shown in figure 4.1B via physical vapor deposition prepared at our institute. To enhance the stability below the gold film a thin layer of chromium ($30\,\text{Å}$) is applied. After forming a SAM at the working electrode the glass disc is covered with a $50\,\mu m$ Teflon spacer and a barium fluoride window ($3\,mm$). Subsequently the cell is filled with a solution of tetramethylammonium hexafluorophosphate (TMAH) in deuterated acetonitrile (c=$0.1\,M$) so that all three electrodes are covered by the solution. Potential control between the electrodes is achieved through a potentiostat (VSP, Bio-Logic Science Instruments).

4.2   Heterodyned VSFG-Spectroscopy

The heterodyned vSFG measurements are taken using a commercial Ti:Sapphire based regenerative amplifier (Legend Elite duo + Vitesse Oscillator, $P_{pulse} = 8\,mJ$, $t_{pulse} = 50\,fs$, $f = 1\,kHz$, $\nu_{center} = 800\,nm$). Of the total pulse energy $2.2\,mJ$ are taken of which a small fraction ($0.2\,mJ$) functions without further treatment as the $800\,nm$ upconversion beam. The rest pumps a commercial optical parametrical amplifier followed by a difference frequency generation unit were the OPAS's signal and idler output are mixed in a collinear fashion (TOPAS, Light-conversion). The resulting tunable IR beam ($P_{pulse} \leq 30\,\mu J$, $t_{pulse} \approx 70\,fs$), of which we use $P_{pulse} \approx 8\,\mu J$, is Gaussian shaped and centered either at $\approx 3000\,cm^{-1}$ for measurements in the methyl stretch region or $\approx 1400\,cm^{-1}$ for measurements in the nitro group stretch region with a respective FWHM of $\approx 350\,cm^{-1}$. The IR beam enters the spectrometer (see figure 4.2) and is split into two portions using a Germanium window beamsplitter. The reflected portion ($\approx 5\%$ of the incident pulse energy) passes a combination of two free standing wire grid polarizers to achieve tunable attenuation and the possibility to control the pulses polarization. Thereafter the beam is focused with the help of a parabolic mirror onto a z-cut quartz window. En route it passes another germanium win-
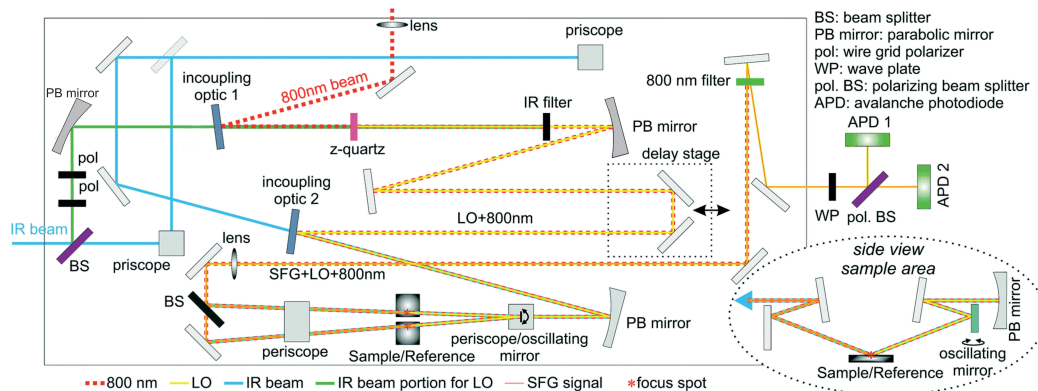
Figure 4.2: Spectrometer Scheme in our Heterodyned vSFG-Spectroscopy. The Scheme was first published in[94].

dow which is coated such that it is highly transparent in the IR but highly reflective in the visible range. This window acts as an incoupling optic upon which the aforementioned 800 nm pulse is reflected to travel collinearly with the IR. This visible pulse is focused as well onto the z-cut quartz where the two beams' nonlinear interaction with the medium generates the local oscillator (LO) at the incident pulses' sum frequency. The IR portion is subsequently filtered and the collinear LO/800 nm pulses are collimated using another parabolic mirror. Subsequently they pass a delay stage.

The second portion of the IR beam after being reflected at several mirrors eventually is overlapped collinearly in space with the LO/800 nm pulses at the second incoupling optic which is similar in type to the first one. All three pulses are focused onto the sample or the reference depending on the current position of the wobbling mirror that oscillates at half the regenerative amplifier's repetition rate. The incident angle equals 70°. A combination of filters ensures only the SFG generated at the sample and the (orthogonally polarized) LO to reach the detectors applied in our balanced detection scheme which is described in detail in section 3.1.3. In short the SFG/LO pulses' polarization angles are rotated by 45° using a Fresnel rhomb (Thorlabs, CCM1-PSBS252) after which they pass a polarizing beam splitter cube. The resulting two outputs are each detected using two avalanche photodiodes (Thorlabs, APD410A2) and com-

65

Figure 4.3: Electrochemical cell geometry for heterodyned potential-dependent SFG measurements. For clarity the window, that is attached via parafilm and is slightly tilted through the Teflon wedge, is not shown.

bined to yield their difference or sum using a Ghz Balun(Marki Microwave). The resulting signal is integrated by gated integrators (SRS, Boxcar Averager) and finally digitized.

If necessary before the detection scheme the orthogonally polarized pulses pass a calcite crystal(1 mm thick, cut at 25° with respect to its optical axis, EKSMA Optics) to compensate for the sample SFG/LO time delay, which is a result of the time delay between the LO/800 nm pulse pair introduced by dispersive optics before the sample (e.g. a window which covers the sample). The underlying compensation principle is extensively described in section 3.2. Fine control of the time delay compensation is achieved by rotating the calcite crystal with the help of a rotational stage (Thorlabs, PRMTZ (stage), KDC101 (Servo Motor Controller)).

Compared to the homodyned vSFG potential-dependent measurements for the heterodyned case slight adjustments had to be applied. Instead of using a uniform Teflon spacer we used a 20μm wedge. That way we changed the angle of the LO portion reflected at the Calcium fluoride (for measurements at ≈3000 cm^{-1}) or diamond (for measurements at ≈1400 cm^{-1}) window with respect to the angle of the LO reflected at the sample enough that the former LO portion does not reach the detector. We also had to use a different cell geome-

try so that direct referencing was a possibility (see figure 4.3). In this case our BK7 substrate had a diameter of 1".

4.3 Self-Assembled Monolayer Preparation

Self-assembled monolayers of the spiropyran derivative 2-(3'3'-dimethyl-6-nitro-3'H-spiro[chromene-2,2'-indole]-1'yl)ethyl (1,2-dithiolane-3)-pentanoate (SP-LA) and octadecanethiol (ODT) are prepared throughout this thesis. While the latter one is commercially available (Sigma-Aldrich, 98% purity) the former is synthesized by T.A. Darwish of the Australian Nuclear Science and Technology Organisation.[97,127]

For the self-assembly at a gold surface, a mirror or a home-build three electrode system such as shown in figure 4.1B, are used as a substrate. The latter one consisted of thin films, $200\,nm$ thick, that were put onto a glass disc via physical vapor deposition in the electrode arrangement shown. If not taken directly from the evaporation chamber, the substrate is cleaned using a series of solvents: successively chloroform, ethanol and purified water. Subsequently the substrate is blown dry with nitrogen and exposed for $\approx 30\,min$ to UV/ozone(ProCleaner™, Bioforce Nanoscience). Subsequently the substrate is immersed into a solution of $0.5\,mM$ SP-LA or $5\,mM$ ODT solved in dichlor methane (DCM) or ethanol respectively. After at least $24\,h$ the substrate is removed from the solution, rinsed with the pure respective solvent (DCM or ethanol) and immediately used in the experiment. Unlike the SP-LA SAM the ODT SAM does not show any sign of degradation even 1 month after the self-assembly.

Chapter 5

Preliminary Sample Characterization

Before their application at electrode surfaces in SFG experiments preliminary measurements on the spiropyran derivative SP-LA were conducted. ATR-FTIR spectra were taken of the closed SP-form and (while constantly irradiated with UV light) the open MC-form to obtain information on the expected molecular vibration which later will help to interpret the recorded vSFG spectra. Additionally the self-assembled monolayer (SAM) formed by the SP-LA was characterized electrochemically with the means of cyclic voltammetry. The results help to identify the upper and lower electric potential limits up to which the SAM's integrity is provided to not irreversibly damage the SAM in potential electrochemical sensor applications. Additionally the space per molecule can be deduced by calculating the molecular density within the SAM. This helps to estimate, whether the 6-Nitro-BIPS-headgroup of the SP-LA has enough free space to undergo the transition to the open (and more extended) MC-form, or whether the ability to switch will be diminished due to sterical hindrance from neighboring molecules. The in this chapter presented results will additionally be compared to literature values.

$\nu_{FTIR}[cm^{-1}]$	Florea et all.[143]	assignment	Delgado-Macuil[144]	assignment
1026	1026	$\delta(C-C-N)$	1026	$\delta_{(oop),sym}(CH)$
1088	(1086)	$(\nu(CO_{ester})$ linker)	1090	$\delta_{(oop),asym}(CH)$
1125	—-	—-	1123	$\delta_{(oop),asym}(CH)$
1168	(1169)	$(\nu(CO_{ester})$ linker)	1175	$\nu(C-O-CH_3)$
1270	1271	$\nu(C-O-C)$	1278	$\nu(CN)$
1297(w)	1307	$\nu(C-N^+)$	1297	$\nu(CN)$
1335	1336	$\nu_{sym}(NO_2)$	1332	$\nu_{sym}(NO_2)$
1361(w)/1378(w)	—-	—-	1388	$\delta_{sym}(CH_3)$
1424 (w)	1426	$\nu(C-O^-)$	—-	—-
1458/1480	1459/1481	$\delta(C-C_{arom})$	1466	$\delta_{asym}(CH_3)$
1518	1520/1509	$\nu_{asym}(NO_2)$	1517	$\nu_{asym}(NO_2)$
1578	1593	$\nu(C=N^+)$	1570	$\delta(C-C_{arom})$
1610	1610	$\nu(C=C)$	1610	$\delta(C-C_{arom})$
1650	—-	—-	1642	$\nu(C=C)$

Table 5.1: Absorption peaks of SP-LA measured with an ATR-FTIR spectrometer (see also figure 5.1)A, compared to literature values. Vibrational modes exclusively present in the UV switched open MC-form highlighted in blue.

5.1 ATR-FTIR Spectra of SP-LA

To conduct the ATR-FTIR spectroscopic measurements the SP-LA is dissolved in deuterated acetonitrile. A few drops are placed at the ATR crystal. The solvent is allowed to evaporate after which the spectrum is taken. The same procedure is repeated while constantly irradiating the sample with a UV-lamp. The resulting linear vibrational spectrum is shown in figure 5.1. The peak center frequencies of the 6-Nitro-BIPS headgroup are listed in table 5.1 and compared to literature values from FTIR measurements of the same head group but with different linker groups.[143,144] From table 5.1 we see that the resonance frequencies of our IR spectrum's strong vibrational features are in good agreement with literature values of 6-Nitro-BIPS. However, the correct assignment of the absorption peaks to vibrational modes of particular functional groups within the molecule based on the literature values is difficult since the peak assignments are inconsistent between different published studies. We shall see in
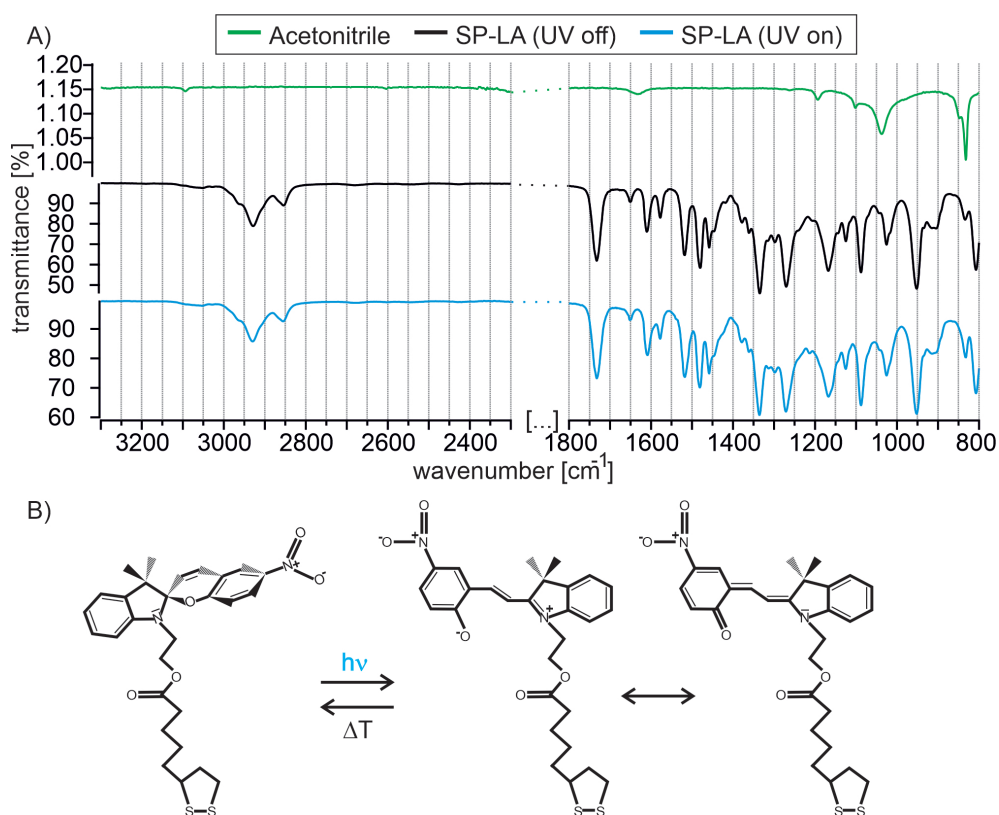
Figure 5.1: A) ATR-FTIR spectrum of SP-LA, without (black) and under irradiation with UV light (blue). To identify remaining traces of its evaporated solvent, a spectrum of pure deuterated acetonitrile is displayed as well (green). B) Assumed closed Spiropyran and open Merocyanine form of the SP-LA without and under constant UV irradiation, respectively.

chapter 6 how SFG selection rules provide in some of these cases a tool to unambiguously decide which assignment is correct.

After irradiation with UV light the IR spectrum hardly changes although the switching was successful which is supported by the sample's change in color from colorless to deep blue. The vibrational modes related to functional groups exclusively present in the switched MC-form according to the literature are highlighted in table 5.1 with blue color. The biggest difference in the UV irradiated spectrum is the appearance of a weak shoulder at around $1424\,cm^{-1}$ which can be assigned to the C-O^{-}-vibration of the former spiro-oxygen in the

open Merocyanine (MC) form. However, this peak is obscured by its proximity to the much stronger absorption at $1458\,cm^{-1}$. Additional peaks exclusively observed in the MC-form by Florea et all. at $1307\,cm^{-1}$ and $1593\,cm^{-1}$ are absent in our case. The reason might be that after the evaporation of the polar solvent the zwitterionic form of the MC-form is no longer supported but instead is its mesomeric quinoic form (see figure 5.1B). This is also in agreement with the weak peak of the aforementioned C-O$^-$ vibration. The additional feature at $1733\,cm^{-1}$ is likely to be the carbonyl vibration of the ester group in the linker chain.[145] The features present at around $2855\,cm^{-1}$, $2930\,cm^{-1}$ and $2960\,cm^{-1}$ are characteristic for terminal methyl groups (compare the Octadecanethiol-spectrum discussed in chapter 3.4) as the ones attached to the SP-LA in the indoline unit (see figure 5.1B).

In summary the absorption frequencies of our SP-LA in the measured FTIR spectra are in good agreement with literature values for molecules containing the same 6-Nitro-BIPS headgroup which points to the high purity of the used SP-LA. However, the assignment of absorption peaks to specific functional groups remains ambiguous within this linear optical technique.

5.2   Electrochemical Characterization

5.2.1   Stable Potential Regime of the SP-LA SAM

The SP-LA SAM is characterized with respect to its stability under an applied potential using cyclic voltammetry. A $0.1\,M$ solution of tetramethylammonium hexafluorophosphate in acetonitrile serves as the electrolyte. This characterization is critical since the identified stability range determines which electrochemical reactions actually can be monitored with such functionalized electrodes in e.g. immunosensors.[14] The stability range is restricted to a certain potential regime on the cathodic side by the reduction of the gold atoms that form the thio-gold bonds which leads to desorption of the SAM molecules.[128] In the anodic regime the 6-Nitro-BIPS headgroup undergoes an irreversible dimerization followed by a reversible redox process[146] as illustrated in figure 5.2A. To determine the potentials at which the aforementioned reactions take
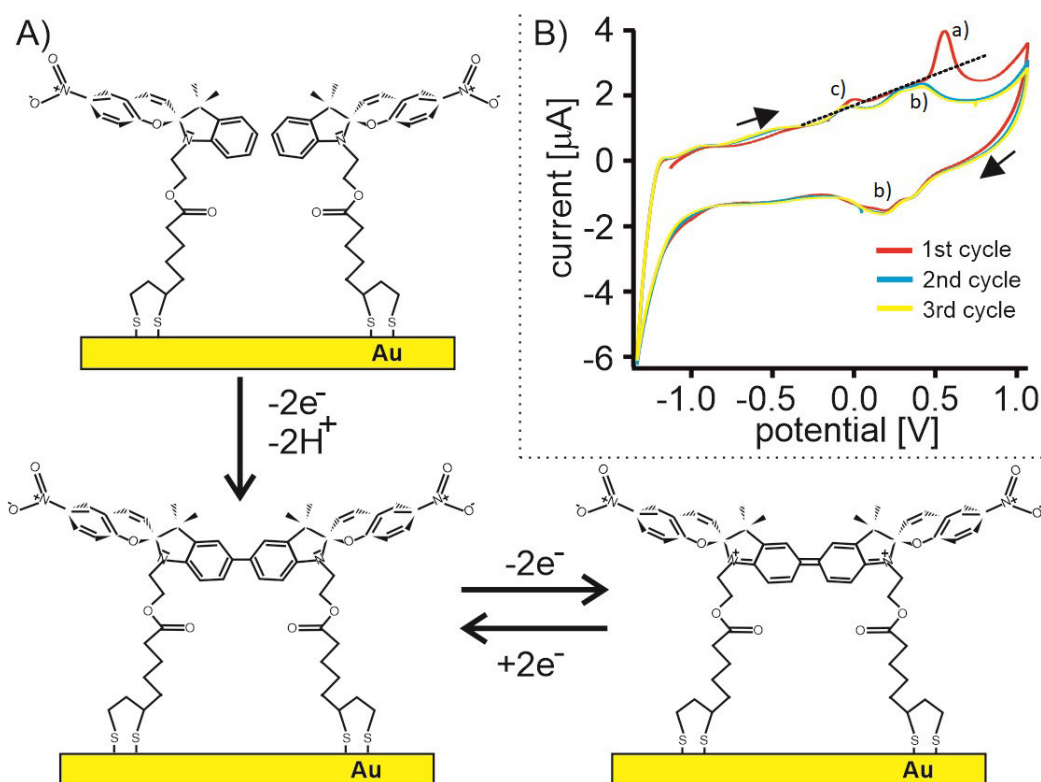
Figure 5.2: A) Electrochemical behavior of SP-LA molecules attached to a gold electrode. An irreversible oxidation accompanied by dimerization is followed by a reversible redox process. B) 3 cycles of the corresponding cyclic voltammogram. The irreversible oxidation a) can only be monitored in the first cycle, while the consecutive reversible redox process b) is visible in all subsequent cycles, as is an unknown feature c). The CV scanning speed is $100 \, mV/s$ and the arrows indicate the scanning direction. Potential measured against a gold pseudo-reference electrode but offset by -220 mV to match the potential axis of a reference measurement taken against a mercury/mercury(II) sulfate reference electrode.

place we take a cyclic voltammogram (CV) ($v_{scan} = 100 \, mV/s$) of our SP-LA SAM in our electrochemical cell against a gold pseudo reference electrode(see figure 4.1 in chapter 4.1). The resulting CV is shown in figure 5.2B. The potential of the used pseudo-reference is unknown, but was in the same range ($\pm 100 \, mV$) for all applied three-electrode cells obtained as described in chapter 4.3. To obtain the absolute potential against a standard reference electrode the axis

of potential was calibrated to an analogous measurement we took of a comparable SP-LA SAM outside the electrochemical cell against a standard mercury sulfate reference electrode, MSE, (shown in figure A1 in the appendix) with known potential. The first cycle of the CV which starts at -1.23 V vs MSE exhibits a current spike at 0.56 V (see feature a) in figure 5.2B). This peak can be related to the dimerization of the SAM molecules and its position is in accordance with literature values.[146] As a consequence of the irreversible nature of the dimerization all subsequent cycles lack this peak. Instead a new double peak feature appears in the forward direction of the CV (maxima at 0.30 V and 0.41 V) as well as in the backward direction (0.18 V and 0.35 V) [feature b] in figure 5.2B. This two peaks can be assigned to the reduction/oxidation of the dimers as shown in figure 5.2A via a radicalic intermediate step[146] not shown. The onset of the SAM desorption is located below -1.10 V which is in accordance with comparable thiol SAMs.[128] An additional spike (feature c) in figure 5.2B) observed in all cycles is not attributed to the SAM but can possibly be assigned to the reduction of oxygen, because our solvent was not purged with nitrogen prior to the measurement.

According to the cyclic voltammogram the stable potential regime of our SP-LA SAM is located between $\approx$-1.0 V and $\approx$0.5 V vs. a standard mercury sulfate reference electrode. The potential-dependent SFG measurements therefore will be restricted to this electric potential range.

5.2.2 Surface Coverage of SP-LA SAM

The coverage of a SAM can be determined by calculating the total charge Q that flows per surface area to perform specific redox processes, e.g. oxidation of the SAMs anchor group and subsequent desorption. In the case of our SP-LA SAM we take the potential region where the molecules dimerize and get subsequently oxidized (at around 0.56 V vs MSE, see feature a) in figure 5.2B). Q can be extracted from the CV by taking the peak area and dividing it by the scanning speed, according to

$$Q = \frac{\int I(\Phi)\mathrm{d}\Phi}{\nu_{scan}} = 1.24\,\mu C \qquad (5.1)$$

Here ν_{scan} represents the CV's scan velocity (100 mV/s).

Taking in mind that two electrons per molecule are transferred (one for the dimerization and one for the subsequent oxidation), the amount of molecules n at the surface can be calculated using Faraday's constant F:

$$n = \frac{Q}{2F} = 6.43 * 10^{-12} mol \qquad (5.2)$$

With respect to our working electrode's area (A=0.20 cm^2) we obtain for our sample a molecular surface density of 3.27*10$^{-11}\frac{mol}{cm^2}$ which is a little lower than the density observed by Ivashenko et. all.[146] of 6*10$^{-11}\frac{mol}{cm^2}$ but of the same order of magnitude. The difference suggests that the SAM in our sample possesses indeed a smaller packing than in reference[146] or it might be the result of the difficulties in determining the actual peak area since one has to subtract the area of the background (capacitive) current. We estimated that current by linearly extrapolating the current that flows at potentials below the peak (see dotted line in figure 5.2B). However, at potentials higher than the feature the background current is lower than the extrapolated current so we might in fact subtract too much off the peak area and consequently our calculated surface density is likely to be underestimated.

With a surface coverage of 3.27*10$^{-11}\frac{mol}{cm^2}$ each molecule occupies an area of roughly 5 nm^2 which equals a square with a side length of 2.2 nm. Since the molecule's linker chain is roughly 2.5 nm long and the head group from the connecting nitrogen atom to the nitro group measures roughly 1.5 nm sterical interactions between the molecules should prevent them from lying down flat on the gold surface. This diminishes interactions between the chromophore and the metal substrate which was shown to hinder the ability to switch from the SP- to the MC-form by quenching the exited transition state involved in the ring opening.[125] 5 nm^2 on the other hand should provide enough space

for the 6-Nitro-BIPS head group so that sterical hindrance does not impair its ability to switch.

Chapter 6

Homodyned SFG spectra of SP-LA SAM at a Gold Electrode

After we have characterized the SP-LA SAM we want to monitor the reorganization of the 6-Nitro-BIPS head group that is associated with the ring opening during the switching process from the closed SP- to the open MC-form. During this process functional groups within the molecule will change their orientation with respect to the substrate becoming or ceasing to be visible within the respective SFG spectrum due to SFG selection rules. Therefor SFG spectra might help to relate certain vibrational modes to specific functional groups within the SP-LA and also to generally understand the conformation of the SP-LA within the SAM. After characterizing the SP- and MC-form and discussing possible remaining ambiguities the potential-dependent SFG response of the SAM will be discussed.

6.1   Comparison: SP vs MC-Form

6.1.1   Conformational Information from SFG Spectroscopy

SFG spectra are taken within our spectroelectrochemical cell (see figure 4.1 in the experimental chapter 4.1) under electrolyte ($0.1\,M$ solution of tetramethylammonium hexafluorophosphate in acetonitrile) but without an applied
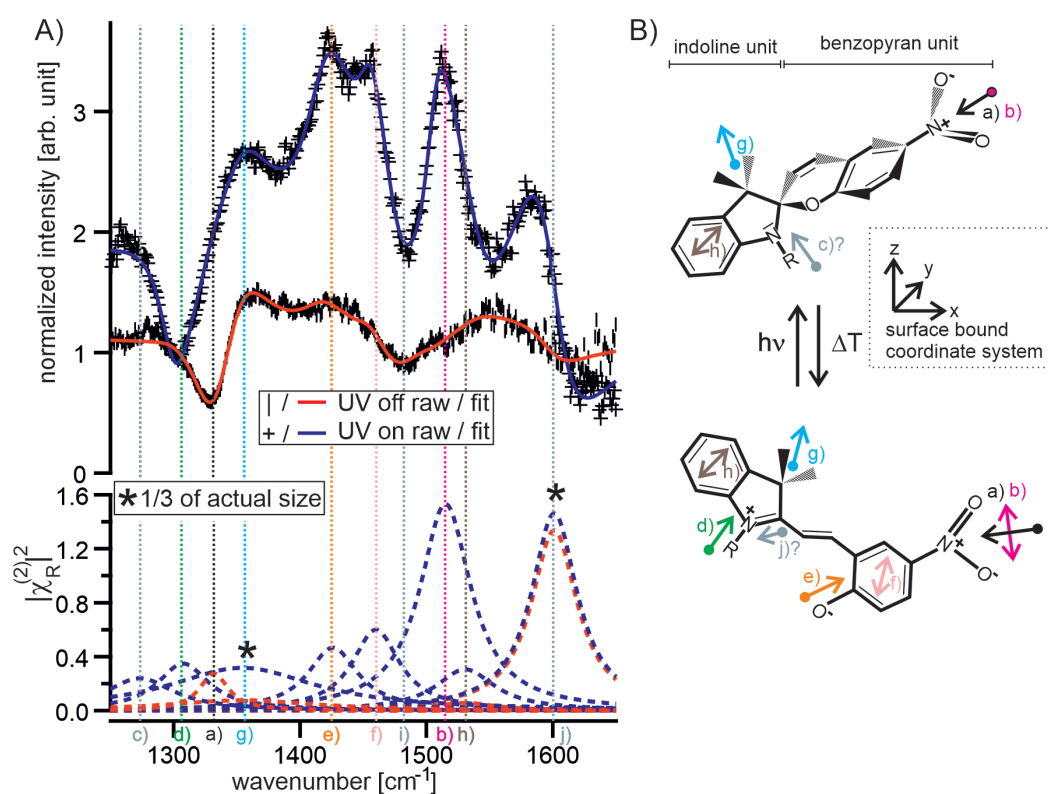
Figure 6.1: A) Fitted SFG spectra of SP-LA SAM in closed SP-form (without UV irradiation) and open MC-form (under UV irradiation). The single resonances are marked in the spectrum and assigned in B) to their origin in the molecule before and after switching. Resonances without clear assignment are marked in gray. The arrows indicate the resonances' corresponding dipole moments.

electric bias from the SP-LA SAM in its closed SP-form and during constant irradiation with UV light in its open MC-form under PPP-polarization combination. The SFG spectra are divided by a spectrum of a bare gold surface taken under the same conditions to correct for the Gaussian shaped background which is caused by the spectral profile of the IR pulse (such a correction is displayed in figure 3.6 in chapter 3.4 where both the uncorrected and corrected SFG spectra are shown). The resulting background corrected SFG spectra are shown in figure 6.1A. The respective unreferenced SP-LA spectra and a spectrum of the non-resonant gold background can be found in figure A2 in the appendix.

As opposed to the FTIR spectra for the closed and open form (figure 5.1 in

chapter 5.1) a massive change can be observed which can be related to the reorientation process of the 6-Nitro-BIPS headgroup as will be discussed in the following for the two vibrational modes of the nitro-group within the SP-LA (schematically depicted in figure 6.1B). According to the literature FTIR spectra the group's symmetric stretching vibration (spectral mode a) in figure 6.1) is located at $\approx 1335\,cm^{-1}$ while the asymmetric stretching vibration (mode b)) can be found at $\approx 1515\,cm^{-1}$ (see table 5.1 in chapter 5.1). Within our SFG spectrum of the closed form the symmetric vibration at $\approx 1335\,cm^{-1}$ resolves into a well pronounced dip, which becomes absent in the MC spectrum (the apparently frequency shifted dip in fact belongs to the C-N$^+$-stretch as will be discussed later). In contrast the asymmetric vibration is absent in the SP-form's spectrum but resolves into a peak in the open form's spectrum at $\approx 1515\,cm^{-1}$. To understand their different behavior we have to recall how a vibrational mode's local hyperpolarizability β is translated into the global second order susceptibility $\chi^{(2)}$. According to equation 2.15 in chapter 2.1.3 the total $\chi^{(2)}$ is the sum of its individual tensor components, which in turn are derived from the tensor components of β via the Euler transformation angles. If the SFG spectrum is taken under PPP polarization combination, however, one probes only four of them, as was discussed in chapter 2.1.4, namely $\chi^{(2)}_{zzz}$, $\chi^{(2)}_{xxz}$, $\chi^{(2)}_{xzx}$ and $\chi^{(2)}_{zxx}$.[40] However, as was shown in table 2.1 in chapter 2.1.6 for our experimental geometry for measurements under acetonitrile the modulus square of the nonlinear Fresnel factor $|L_{zzz}|^2$ outreaches the modulus squares of the other contributions' L-factors by 2 to 5 orders of magnitude. The $\chi^{(2)}_{zzz}$ component as a result is massively enhanced and should dominate the taken SFG spectra and the other potentially contributing tensor components can(and will) be omitted. Explicitly performing the Euler-Transformation for determining the $\chi_{v;zzz}$ tensor component for a specific mode v we get:

$$\chi_{v;zzz} = < sin(\psi)sin(\theta)\beta^{[SFG]}_{v;x} - cos(\psi)sin(\theta)\beta^{[SFG]}_{v;y} + cos(\theta)\beta^{[SFG]}_{v;z} >$$
$$+ < sin(\psi)sin(\theta)\beta^{[Vis]}_{v;x} - cos(\psi)sin(\theta)\beta^{[Vis]}_{v;y} + cos(\theta)\beta^{[Vis]}_{v;z} > \quad (6.1)$$
$$+ < sin(\psi)sin(\theta)\beta^{[IR]}_{v;x} - cos(\psi)sin(\theta)\beta^{[IR]}_{v;y} + cos(\theta)\beta^{[IR]}_{v;z} >$$

As the angle brackets indicate, the transformation is performed about the aver-

age molecular orientation. For isotropic surfaces where ψ can take any value the averaged x- and y-term equal zero. Consequently any vibration to be observed in the spectrum needs to exhibit a Raman transition moment and a transition dipole moment with vector components along the surface normal (commonly the z-direction in the surface bound coordinate system). In the SP-form the transition dipole moment for the anti symmetric stretch, however, is perpendicular to the surface normal (mode b in the spectrum in figure 6.1). Consequently the asymmetric stretch mode does not contribute to $\chi_{zzz}^{(2)}$ and the feature is absent in the SFG spectrum. Upon irradiation the SP-LA's benzopyran unit turns by 90° to be in plane with the indoline unit (see figure 2.6 in chapter 2.2.2) and consequently the transition dipole moment of the nitro group's asymmetric stretch now exhibits a large component in z-direction which gives rise to a strong peak in the spectrum (see figure 6.1). The symmetric stretch mode's amplitude in contrast diminishes during switching. The sole reorientation of the head group, however, does not influence the tilt angle θ of the symmetric stretch mode's transition dipole with respect to the surface normal indicating that the reorientation of the head group is accompanied with a lowering of the head group.

6.1.2 Features Appearing as Peaks or Dips

As was pointed out in detail in chapter 2.1.6 the line shape of a particular resonance depends on the interference of the non-resonant and resonant second order susceptibilities according to:

$$
\begin{aligned}
I_{SFG}(\omega_{IR}) &\propto |\chi_{NR}^{(2)} + \chi_{R}^{(2)}(\omega_{IR})|^2 \\
&\propto |\chi_{NR}^{(2)}|^2 + |\chi_{R}^{(2)}|^2 + \chi_{NR}^{(2)}\chi_{R}^{(2)*} + \chi_{NR}^{(2)*}\chi_{R}^{(2)}
\end{aligned}
\tag{6.2}
$$

The square term of $\chi_{NR}^{(2)}$ gives a simple off set. The square of $\chi_{R}^{(2)}$ can be neglected since in the case of gold $\chi_{NR}^{(2)}$ is orders of magnitudes larger than $\chi_{R}^{(2)}$.[40] The line shape of a particular resonance is therefore dominated by its cross

terms. Expanding the fitting equation 2.30 for homodyned SFG spectra and neglecting the square terms we get:

$$\chi_{NR}^{(2)}\chi_{R}^{(2)*} + \chi_{NR}^{(2)*}\chi_{R}^{(2)} = 2\sum_{q} N_q A_q |\chi_{NR}^{(2)}| [\frac{(\omega_{IR} - \omega_q)cos\Phi_{NR}}{(\omega_{IR} - \omega_q)^2 + \Gamma_q^2} + \frac{\Gamma_q sin\Phi_{NR}}{(\omega_{IR} - \omega_q)^2 + \Gamma_q^2}]$$

$$(6.3)$$

The sign of this cross term is determined by the sign of the resonant amplitude A_q as well as the non-resonant phase Φ_{NR}, which also determines the weighting between the dispersive and absorptive line shape. The sign of A_q depends in turn on the signs of the transition Raman $\frac{\partial \alpha}{\partial Q}$ and dipole moment $\frac{\partial \mu}{\partial Q}$ (see equation 6.4) and needs to be determined from theory. The overall sign is hardly predictable without an exact calculation which can be seen by the fact that it varies even for the same functional group attached to different molecules.[147]

$$A_q \propto \frac{\partial \mu}{\partial Q}\frac{\partial \alpha}{\partial Q} \qquad (6.4)$$

Therefore the appearance of a peak or dip in the SFG spectrum cannot without further knowledge reveal the orientation of the vibration's corresponding functional group. If, however, a vibration that was resolved in a peak in the spectrum suddenly appears as a dip, and the molecule has not significantly changed its structure in proximity of the corresponding functional group, then the functional group's transition dipole moment must have changed its orientation such that the sign of one Euler rotation matrix R changes which in turn changes the sign in $\chi_R^{(2)}$.[148]

This orientational change can be seen strikingly for the symmetric stretching mode of the Nitro-group in an additional experiment. An SFG spectrum is taken before injecting acetonitrile into the spectroelectrochemical cell. In the absence of acetonitrile the spectral mode is resolved as a peak as shown in figure 6.2A supposedly indicating a reorientation of the head group upon the solvent's addition as sketched in 6.2B.
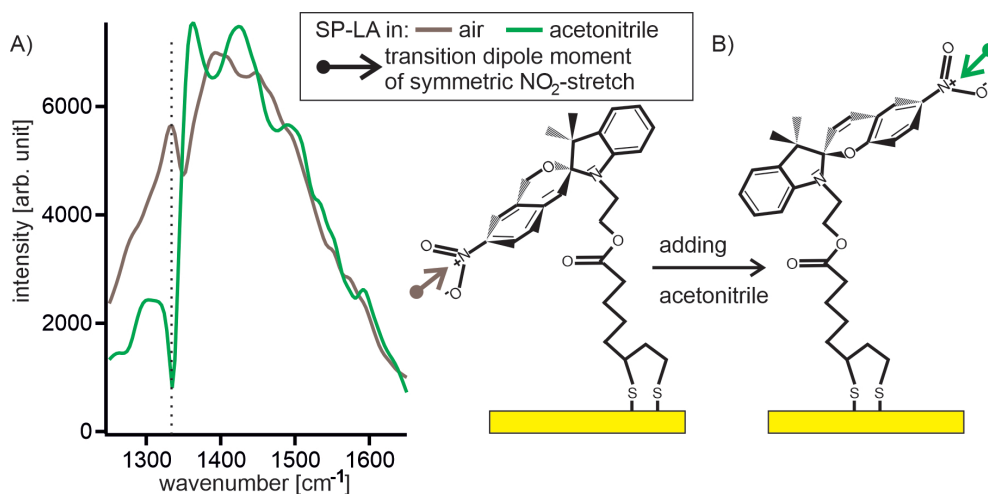
Figure 6.2: A) SFG spectra which show a change of the spectral appearance of the symmetric stretch vibration of the SP-LA's nitro-group upon the addition of acetonitrile. Spectral position indicated by dotted line. B) Sketch of the possible change in the transition dipole moment of the symmetric stretch mode upon the solvent addition that causes the observed spectral change.

6.1.3 Spectral Assignment in SP-LA SFG spectra

Global Fitting

The spectral bandwidth covered by our measurements ranges from $\approx 1250\,cm^{-1}$ to $1600\,cm^{-1}$. According to the literature[143,144] and our FTIR measurements presented in chapter 5.1 we can expect up to 10 resonant features within this range. Each of those is characterized by an amplitude A, a half width Γ and a center frequency ω. In addition with the two parameters for the non-resonant susceptibility's magnitude $|\chi_{NR}^{(2)}|$ and its phase Φ our fit contains 32 independent parameters. This large number of fit parameters obviously reduces the uniqueness of the fitting results which is a common problem in SFG spectroscopy.[91] In a first approximation we assume that the resonance frequencies and spectral line shapes are independent on the switching state of the SAM, which allows us to perform a global fit on the two spectra depicted in figure 6.1 using the fitting equation 2.30 presented in chapter 2.1.6. Fitting this way reduces the flexibility of the fit and therefore enhances its uniqueness, however, on the ex-

Assign.		Value	Assign.		Value
$\chi_{NR}^{(2)}$	$\|\chi_{NR}^{(2)}\|$	0.90±0.02/	$\chi_{NR}^{(2)}$	Φ	1.44±0.03/
	$\|\chi_{NR}^{(2)}\|$	0.60±0.03		Φ	1.01±0.07
$\nu(C-N)$	A	1.48±0.70/	$\nu(C-N^+)$	A	-2.69±0.57/
	A	15.99±1.42		A	-14.40±1.18
	ω_q	1273±1		ω_q	1307±1
	Γ_q	32.66±1.04		Γ_q	24.40±0.82
$\nu_{sym}(NO_2)$	A	-7.17±0.57/	$\nu(CH_3)$	A	33.40±2.58/
	A	-2.50±0.41		A	68.00±4.10
	ω_q	1331±1		ω_q	1353±2
	Γ_q	13.64±0.67		Γ_q	69.74±2.34
$\nu(CO^-)$	A	2.42±0.45	$\nu(C-C_{arom})$	A	2.77±1.05
	A	16.00±0.77		A	17.13±2.62
	ω_q	1423±1		ω_q	1456±1
	Γ_q	23.44±0.40		Γ_q	22.12±0.92
$\nu(C-C_{arom})$	A	-3.72±1.63	$\nu_{asym}(NO_2)$	A	-0.35±1.16
	A	-5.78±3.55		A	29.17±5.09
	ω_q	1474±3		ω_q	1509±1
	Γ_q	25.78±4.79		Γ_q	23.57±1.01
$\nu(C-C_{arom})$	A	6.55±1.51	$\nu(C=N^+)$	A	-42.07±0.52
	A	-15.14±5.25		A	-43.99±0.59
	ω_q	1524±3		ω_q	1591±1
	Γ_q	27.39±1.16		Γ_q	21.00±0.20

Table 6.1: Global fitting parameters of SFG spectra of SP-LA SAM in its native and UV switched state. Within the fit 10 resonances are assumed. Distinct fitting parameters for the UV-switched spectrum are highlighted in blue.

pense of excluding processes that affect Γ (e.g. life time broadening) and ω (e.g. Stark shift at charged surfaces) during switching. Fitting was conducted in two steps. First the center frequencies were set to literature values and held fixed to generate a good initial guess for the remaining parameters. Afterwards the fit was repeated with only free parameters.

Fitting result

Performing the global fitting procedure described in the previous section we obtained the following parameters which are listed in table 6.1. As expected the

amplitude for the symmetric Nitro-group stretch (figure 6.1, feature a) located at $1331\,cm^{-1}$ is diminished upon switching indicating the rearrangement of the SP-LA head group. This is in agreement with previous observations.[127] The corresponding anti symmetric stretch (feature b) located at $1509\,cm^{-1}$ which is basically absent in the spectrum of the SP-form in turn becomes quite strong in the open form.

Additional resonances almost absent in the SP-form but prominent in the MC-form include the ones located at $1273\,cm^{-1}$ (feature c), $1307\,cm^{-1}$ (d), $1423\,cm^{-1}$ (e) and $1456\,cm^{-1}$ (f). Since the bands at $1307\,cm^{-1}$ (d) and $1423\,cm^{-1}$ (e) are exclusively assigned to the switched form and hence this behavior can be expected. Surprising is, however, the evolution of the peaks c) and f). According to Florea et.all[143] (see table 5.1) the band at $1273\,cm^{-1}$ can be attributed to the stretch vibration of the (C-O-C)-group at the molecules' spiro-center. If this assignment was correct we would expect that upon switching a bond break occurs and this vibration should consequently vanish. Our data in contrast shows a significant increase of the peak amplitude. Delgado-Macuil et. all[144] assigned this band to a (C-N)-stretch that might still occur in the switched form provided the MC-form would, at least partially occur in its quinoic form. The fact, that it is hardly observable in the closed SP-form indicates a strong tilt in the linker chain and hence a weak transition dipole moment of this stretch along the surface normal. Limiting those interactions could lead to a straightening of the chain thereby increasing the transition dipole moments z-component.

The vibration located at $1456\,cm^{-1}$ (f) could originate from the deformation stretch vibration in the aromatic system of the benzopyran unit of the molecule. The small amplitude of the peak in the native form suggests that its transition dipole moment is oriented perpendicular to the surface normal. Reorientation of the head group upon switching would consequently lead to an increase in the observed amplitude of the SFG signal which is in good agreement to our measurement.

The next features to be discussed are located at $1353\,cm^{-1}$ (feature g in figure 6.1) and $1524\,cm^{-1}$ (h). The former was assigned to the methyl groups located in the molecules indoline unit. As such it should show a peak in both the

open and closed form and should not be affected by the head groups reorientation upon switching. The fact that a previously strong feature increases even further upon switching supports the assumption that in addition to the head groups reorientation the linker chain becomes less tilted. The same logic applies for the resonance at $1524\,cm^{-1}$ which hence should also originate from the indoline unit and was assigned to another aromatic stretch vibration. It should be noted that its center frequency extracted from the fit deviates significantly from the value given in the initial guess and thus from its FTIR value ($1578\,cm^{-1}$, see table 5.1). The exact origin of this shift is unknown. In contrast the other center frequencies are in reasonable agreement with their literature values. Anyway said resonance is a relatively small feature and therefore its exact position might easily be obstructed by the limited uniqueness of the fit.

6.1.4   Fitting Ambiguities

As discussed in the previous section apart from two exceptions the resonance amplitudes display a significant change between the SP- and MC-form. These exceptions are the resonances at $1474\,cm^{-1}$ (i) and at $1591\,cm^{-1}$ (j) which remain approximately unaffected. Although according to the fit the amplitude of the former one changes from -3.72 to -5.78 this changes is not considered significant because at the same time the non-resonant susceptibility changes in magnitude from 0.9 to 0.6. As given in equation 6.3 $|\chi_{NR}^{(2)}|$ and A_q form a product. The increase in one can consequently compensate a decrease in the other. If we normalized all resonance amplitudes for the modes in the SP and MC-form by the respective $|\chi_{NR}^{(2)}|$, the mode at $1474\,cm^{-1}$ would have about the same amplitude in both forms in contrast to the other modes.

The amplitude for the resonance at $1591\,cm^{-1}$ as resolved in the fit does not change at all, although a look into the graph at figure 6.1 would suggest an increase in its absolute value. The literature assignment to this mode by Florea at all.[143] to $\nu(C = N^+)$ which exclusively occurs in the MC-form also leads to the expectation of an increase. If we apply the same logic as in the case of the $1474\,cm^{-1}$ and normalize the amplitudes by the respective $|\chi_{NR}^{(2)}|$ for the SP and

MC-form a change in amplitude for the mode at $1591\,cm^{-1}$ during switching would be the result.

These two examples lead to the question, whether a change in $|\chi_{NR}^{(2)}|$ is expected during switching or whether this parameter during the global fit should be linked for the SP and MC-form (just as the center frequencies and the FWHM, see comments on global fitting in section 6.1.3). To resolve this predicament we would need to have a way to independently determine $|\chi_{NR}^{(2)}|$ and see its development during switching. According to equation 6.2 this can be done when $\chi_R^{(2)}$ becomes zero, in other words if we measure at a frequency, where we do not expect any resonances. Unfortunately in the observed spectral region we do not have such a point. This problem illustrates one of the big problems with homodyned SFG spectroscopy and underlines the need to measure phase-resolved spectra to disentangle $|\chi_{NR}^{(2)}|$ and A.

6.1.5 Non-Resonant Susceptibility's Phase

As was pointed out in the previous section there is an apparent change in the magnitude of the non-resonant susceptibility $|\chi_{NR}^{(2)}|$ originating from the gold substrate during the transition from the SP- to the MC-form. Interestingly according to the fit the phase of the non-resonant second order susceptibility shows a huge difference for the closed SP- ($1.44\,rad$) and open MC-form ($1.01\,rad$) respectively as well. This equals a shift of $\approx 25°$. Although a change in the phase and magnitude of $\chi_{NR}^{(2)}$ of a (in these cases single crystal) gold electrode have been observed upon a changing static electric field due to an applied electric bias,[54,149] it is debatable whether the change in dipole moment in the molecule upon switching from $\approx 5\,D$ to $\approx 17\,D$[111] is sufficient to justify this huge change in phase. This is especially true since as explained earlier the molecule's linker chain is likely to straighten up in the MC-form. Therefore the substrate's surface should be even less affected by anything related to the molecules head group.

As outlined before we cannot independently measure $|\chi_{NR}^{(2)}|$. However, as a test the same spectra discussed above are fitted assuming one non-resonant phase

and magnitude fits both the open and closed form. The results can be seen in table 6.2. The fitting uncertainties for the individual parameters is about the same as for the fit above. Additionally most of the center frequencies are again in good agreement with the literature values, with the exception of the resonance expected to be located at around $1480\,cm^{-1}$[143] (feature f) at $1474\,cm^{-1}$ in the previous fit) that disappeared in favor of a new, but insignificantly small feature at $1400\,cm^{-1}$. Instead the resonance at $1572\,cm^{-1}$ (expected at $1570\,cm^{-1}$[144]) could be resolved, which shifts to $1524\,cm^{-1}$ if $|\chi_{NR}^{(2)}|$ and Φ_{NR} are allowed to be different for the MC and SP-form. This feature, however, is resolved with a huge FWHM thus overlapping with the peak at $1590\,cm^{-1}$ (f)). The change in amplitude during switching expected for the latter one (assuming the assignment to the $C=N^+$ stretch vibration is correct) is then realized in the fit by a change in amplitude of the peak at $1572\,cm^{-1}$.

Another contradiction to previous assignments is the appearance of a strong amplitude for the $C-N^+$-vibration at $1303\,cm^{-1}$ in the spectrum of the closed SP-form since it should exclusively appear in the open MC-form. Additionally its amplitude changes here its sign upon switching. As laid out before a switch in sign of the amplitude would indicate a flip of the direction of the transition dipole moment either because the chemical environment of the respective functional group undergoes a significant change, or because the group itself has flipped direction. While the latter can be excluded since it would require the linker chain to coil up which is sterically hindered by the bulky head group, the chemical environment changes since the spiro-center's oxygen is located in close proximity to the $C-N$ group in the SP-form while it is well separated after the transition into the MC-form. The oxygen's influence on the transition dipole moment of the $C-N$ group, however, is difficult to predict and would require a thorough theoretical calculation.[147] Anyway, considering that the resolved FWHM of the $C-N^+$-stretch is quite broad it is far more likely that the apparent change in the amplitude's sign is a fitting artifact due to the overlap with the adjacent spectral feature resolved at $1283\,cm^{-1}$.

Finally we shall have a look at the obtained value for the phase of the non-resonant $\chi^{(2)}$. With $0.24\,rad$ which equals $13.8°$ this differs a lot from the expected non-resonant phase of a gold substrate $\approx 90°$ which has also been

Assign.		Value	Assign.		Value
$\chi_{NR}^{(2)}$	$|\chi_{NR}^{(2)}|$	0.65±0.01	$\chi_{NR}^{(2)}$	Φ	0.24±0.03
$\nu(C-N)$	A	-4.15± 2.13	$\nu(C-N^+)$	A	21.86±3.41
	A	42.94±7.23		A	-64.23±6.65
	ω_q	1283±1		ω_q	1303±4
	Γ_q	35.02±1.30		Γ_q	59.39±2.95
$\nu_{sym}(NO_2)$	A	-10.18±0.98	$\nu(CH_3)$	A	16.63±1.91
	A	-0.49±0.41		A	39.81±4.99
	ω_q	1341±1		ω_q	1363±1
	Γ_q	17.06±0.86		Γ_q	45.43±2.67
$\nu(CO^-)$	A	5.13±0.31	$\nu(C-C_{arom})$	A	10.26±0.35
	A	12.43±0.42		A	27.89±0.56
	ω_q	1426±1		ω_q	1458±1
	Γ_q	18.82±0.29		Γ_q	24.92±0.20
$\nu(C-C_{arom})$?	A	1.37±0.31	$\nu_{asym}(NO_2)$	A	3.75±0.38
	A	1.66±0.36		A	24.56±0.38
	ω_q	1400±1		ω_q	1512±1
	Γ_q	12.20±1.19		Γ_q	20.41±0.11
$\nu(C-C_{arom})$	A	85.00±2.96	$\nu(C=N^+)$	A	-55.38±1.50
	A	45.45±2.49		A	-51.64±1.06
	ω_q	1572±1		ω_q	1590±1
	Γ_q	48.34±1.49		Γ_q	19.96±0.21

Table 6.2: Fitting parameters of alternative global fit, where in addition to the resonance frequency and the FWHM also the magnitude and phase of the non-resonant second order susceptibility is assumed constant during the switching process from the SP- (black) to the MC-form (blue).

confirmed in a phase-resolved measurement, that will be discussed in chapter 7.1.5, and far more than the phase in the previous fit (82.5° and 57.9° for the unswitched and switched spectrum respectively). It is rather unlikely that such a large shift can be caused by the presence of the SP-LA SAM.

All the above mentioned inconsistencies clearly indicate that the results from the second fit presented in 6.2 are not reliable and we will continue working with the values (especially center frequencies and FWHM) obtained in the first fit presented in table 6.1 allowing the non-resonant susceptibility's phase and magnitude to change. The abandoned fit, however, stands as a reminder,

that fitting homodyned SFG spectra (especially on metal substrates) is far from unique and should be met with at least some skepticism.

6.2   Kinetic Data

As discussed in section 6.1.3 the obtained SFG spectra provide spectral features of different functional groups within the SP-LA molecule. Therefore it is in principle possible to follow the individual kinetics of each moiety during the photoswitch to obtain a full structural picture of the switching process. This process can be roughly divided in the fast breaking of the spiro-centers $C-O$-bond and the subsequent slow reorientation of the head groups benzopyran unit (see figure 6.3). Depending on their location in the molecule the functional groups' spectral response might be affected by both processes or only one of them (e.g. the amplitude of the $C-N^+$-stretch should show a faster kinetic than the modes for the NO_2-group). Therefor the kinetic data might also facilitate the yet unclear assignment of the features at $1273\,cm^{-1}$ (feature c in figure 6.1), $1474\,cm^{-1}$ (feature i) and $1591\,cm^{-1}$ (feature j).

Different kinetics for the bond breaking and reorientation have already been observed for the free 6-Nitro-BIPS headgroup in solution, where they happen on timescales that differ by three orders of magnitude (in ethanol in 10 ps and 10 ns respectively).[150] Inside a SAM this time scale difference is expected to be even larger, since sterical hindrance should primarily slow down the reori-
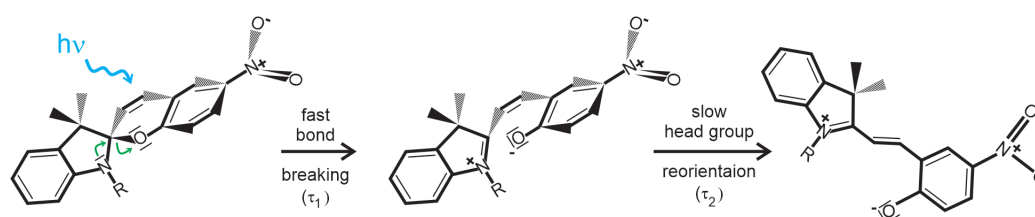
Figure 6.3: Sub processes during the switching from the closed SP- to open MC-form. Irradiation with UV light induces a fast bond break at the spiro-center, followed by a slow reorientation of the head group to yield the MC-form. The individual time scales differ by three orders of magnitude in solution.[150]
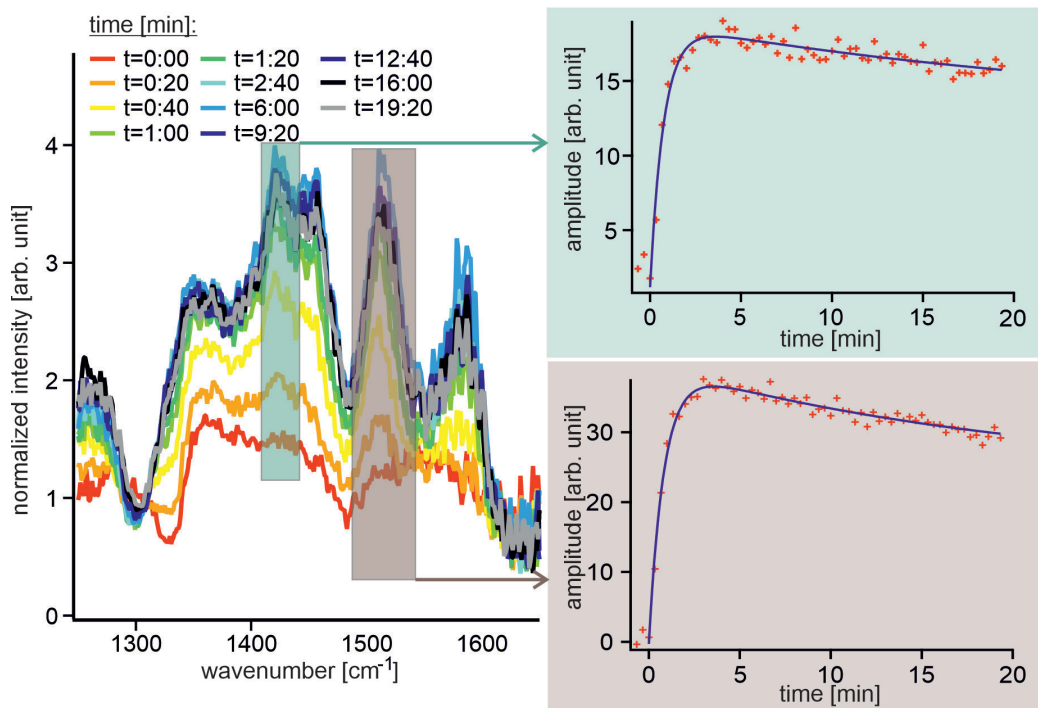
Figure 6.4: Selection of SFG spectra showing the peak development during switching. Individual peak amplitudes (+) are plotted as a function of time and fitted (continuous line) to a bi-exponential function.

entation.[127]

To determine the temporal behavior SFG spectra were measured as a function of time during the switching process. Each time point consists of 20'000 averaged SFG spectra which corresponds to an acquisition time of $20\,s$ per SFG spectrum. A selection of the resulting time dependent spectra are depicted in figure 6.4. The spectra were further analyzed performing a global fit on all spectra analogous to the global fit presented in section 6.1.3. To facilitate the fitting the values for the resonance frequencies and FWHM were taken from this previous fit and held fixed. From the result we can extract the time evolution of the amplitudes for each single resonance peak in the SFG spectrum. Under the presumption that indeed two processes happening on different time scales are involved in the switching process a bi-exponential fit is performed on each of these time traces.

$\tilde{\nu}\,[cm^{-1}]$	$\tau_1^{-1}\,[min^{-1}]$	$\tau_1[s]$	$\tau_2^{-1}[min^{-1}]$	$\tau_2[s]$
1273	1.51±0.35	40±21	0.23±0.16	262±712
1307	1.14±0.06	53±6	0.04±0.03	1607.15±7291
1331	1.35±0.31	44±22	0.25±0.21	240±1368
1353	1.14±0.16	53±15	0.04±0.07	1618±2384
1423	1.32±0.12	45±9	0.04±0.06	1664±3129
1456	0.96±0.11	63±15	0.04±0.06	1643±3129
1474	0.75±0.57	80±297	0.18±0.21	326±2453
1509	1.20±0.07	50±6	0.05±0.03	1266±2672
1524	1.20±0.16	50±14	0.05±0.04	1138±2672
1591	0.33±0.55	180±346	0.14±0.43	427±313
$\lvert\chi_{NR}^{(2)}\rvert$	1.20±0.15	50± 6	0.05±1.00	1266±1143
Φ_{NR}	1.24±0.60	48±16	0.03±1.48	1821±1961

Table 6.3: Time constants obtained through fitting the resonances' amplitude evolution using a bi-exponential fit.

$$A(t) = y_0 + A_1 e^{\tau_1^{-1}t} + A_2 e^{\tau_2^{-1}t} \qquad (6.5)$$

The so obtained time constants are listed in table 6.3.

Examplarily the time evolution of the $C-O^-$-stretching (green) and asymmetric NO_2-stretching mode (brown) is depicted in figure 6.4 along with the corresponding bi-exponential fits. As can be seen the $C-O^-$-mode's amplitude rapidly increases for the first two minutes and then slowly decreases again which seems to support the idea of the two separate processes, the bond break and reorientation, happening at different time scales. The corresponding timescales are ≈45 s and ≈1664 s. While the first process indeed is much faster than the second one the longer timescale seems with roughly half an hour unphysically long. If this process was to be assigned to the head group reorientation this would contradict the actual spectra in figure 6.4A since the final spectral shape does not change after ≈3 min except for the absolute intensity. Especially the peak for the asymmetric NO_2-stretch which is exclusively associated with the head group reorientation already reaches its maximum af-

ter this short time. In fact its peak development also shows a slow decrease at longer times. Table 6.3 lists all values for τ_1^{-1} and τ_2^{-1} as obtained through fitting with equation 6.5. For a complete list of all fitting parameters and graphs of all amplitudes' time dependent evolution check the appendix (figure A3-A12 and table A2).

It is interesting to notice, that most resonant features change on the same time scales within the range of fitting ambiguity. However, it should be noted that the reliability of this bi-exponential fit is very limited and we thus need to discuss the resulting values with great care. For instance a huge fitting uncertainty for τ_1^{-1} was obtained in the case of the aromatic $C-C$-deformation stretch at $1474\,cm^{-1}$ and the $C=N^+$-stretch at $1591\,cm^{-1}$, because they do not change significantly in amplitude during the switching process (see table 6.1). Accordingly τ_2 can only be determined with a huge fitting uncertainty. This is especially true for the amplitude of the symmetric NO_2-stretch which is hard to determine, since after the fast process took place the amplitude almost vanishes and any further changes will be obscured by noise. Also the amplitude of the resonance at $1273\,cm^{-1}$ practically stays constant after the initial fast change. Why this is the case is not directly apparent but being at the fringes of our spectrum this might be the result of uncertainties in the disentanglement of its amplitude with the magnitude of the non-resonant susceptibility (see the discussion on fitting ambiguities in section 6.1.4).

Since apart from the discussed exceptions the peaks show a similar kinetic independent on their position in the molecule, it can safely be assumed, that within the given time resolution we are not able to independently monitor the bond breaking and reorientation process. It is likely that the fast kinetic process described by τ_1^{-1} is the combination of bond breaking and head group reorientation. To enhance the time resolution one would need to average the spectra for less than 20 seconds. Unfortunately this is not possible with the current homodyned SFG setup.

The assignment for the second process, however, is more ambiguous. Since it involves the slow decrease of basically all resonances' amplitudes (though on different relative scales) it could be the result of a slow destruction due to photo-bleaching. It could also be the result of the slow increase of the non-

resonant susceptibility's magnitude and the subsequent compensation in the amplitude values according to equation 6.3, in other words a fitting artifact. To disentangle the effect of $\chi_{NR}^{(2)}$ on the resonant part of our spectrum we would need a phase-resolved measurement so that $\chi_{NR}^{(2)}$ is resolved into a linear off set in the real and imaginary parts of the resulting spectra (see figure 2.3 in chapter 2.1.6).

Finally the slow process could be assigned to an overall reorganization of the molecules with respect to each other that involves a change of the chains' tilt angle. Such a reorganization has been observed previously by Darwish et all.[127] but exclusively during the first switching. This reorganization prevented the amplitude of the symmetric NO_2-stretch to reach its initial strength during back switching. In fact as will be shown in the following chapter for the bias dependent data we see this effect on the symmetric NO_2-stretch in the bias dependent kinetic data, where additionally this slow reorganization process is absent.

6.3 Potential-dependent Spectra

6.3.1 Bias Induced Changes without Constant UV Irradiation

As pointed out in chapter 2.2.2 and in previous publications[111–117] a wide range of stimuli can induce a change in molecular switches in general and spiropyran in particular. Especially with regard to its potential use in "smart" electrodes and electrochemical sensors it is necessary to investigate the behavior of our SP-LA SAM at the surface of an electrode to which a bias is applied. Such electrodes are "smart" in a way that they can be switched "On" or "Off" under specific defined conditions, because in one form of the molecular switch a desired electrochemical reaction is impaired while in the other it is not. In the case of immunosensors for instance the molecular switch in one form is able to interact with the analyte (e. g. an antibody) thus blocking the electrode and impairing the electrochemical reaction of a redox probe (the sensor is "On").[14] The resulting drop in current can be determined amperometrically and is a function of blocked electrode surface and thus analyte concentration.
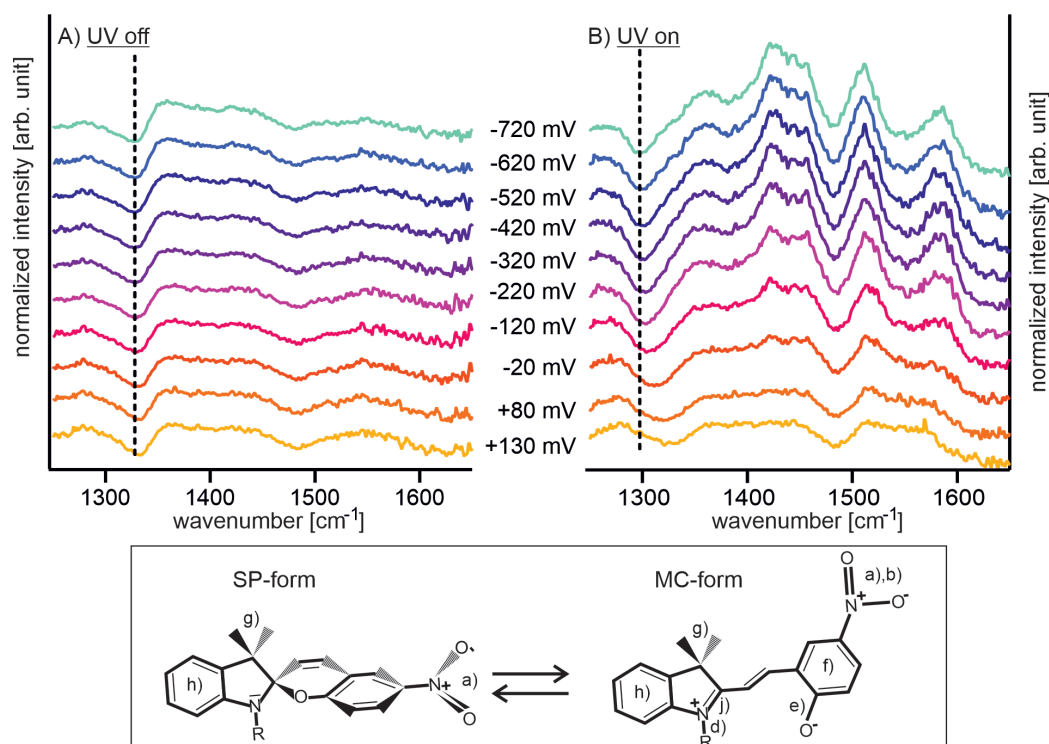
Figure 6.5: Potential-dependent SFG spectra of the SP-LA SAM attached to a gold electrode. A) without and B) under constant UV irradiation. For clarity the different spectra are shifted with respect to each other.

In the "Off" state no interaction between the analyte and the molecular switch occurs, thus a background measurement can be conducted and the analyte can be washed off the sensor ensuring its reusability. At the potential where the redox probe reacts (when the sensor is in its "On"-state), the molecular switch must not be influenced by the presence of the electric bias (to not accidentally switch the sensor "Off"). The first question to be answered is thus whether the SP-LA can be switched from the closed SP- to the open MC-form solely due to the presence of an electric bias within the stable potential regime determined in chapter 5.2.1 where no electrochemical alteration of the SAM occurs. Therefore SFG-spectra are taken successively at the same sample position at different static potentials. The potential is varied alternately between more positive and more negative values to ensure any observed change is reversible.

93

Changes in Line Shape

The resulting potential-dependent SFG spectra without constant UV irradiation can be seen in figure 6.5A. Since the line shape of all spectra appears basically unchanged one can conclude, that within the investigated potential range no bias induced ring opening occurs in the SP-LA SAM. However, a close inspection on the evolution of resonance amplitudes as a function of potential in table 6.4 reveals an increase for the amplitude of the methyl stretch located at $1353\,cm^{-1}$ (feature g) (and to a smaller extent an increase for the $C-N$-stretch at $1273\,cm^{-1}$(c)) towards more negative potentials. This indicates a change in the tilting angle of the whole molecule with respect to the surface normal, in other words an increase of the z-component of the transition dipole moments of functional groups' vibrations (see also chapter 6.1.1), rather than ring opening, especially since the resonances indicating a switching of the molecule and reorientation of the head group, namely the $C-N^+$-stretch at $1307\,cm^{-1}$ (d), the asymmetric NO_2-stretch at $1509\,cm^{-1}$ (b) and the $C-O^-$-stretch at 1423 cm^{-1}(e), (see inset figure 6.5 or in more detail figure 6.1B) remain small and constant (within the fitting limit of uncertainty).

To verify this interpretation one could determine the tilt angle to estimate the electric potential the head group actually experiences. If the molecule is not tilted with respect to the surface normal, the head group will be $\approx 2.5\,nm$ away from the surface which equals the length of the linker chain. Consequently the applied potential should already be vastly screened within our electrolyte ($0.1\,M$ solution of TMAH in acetonitrile). This screening is possible since the anchor group of the molecule is $\approx 0.24\,nm$ broad and accordingly only a small area of the estimated $\approx 5\,nm^2$ of substrate area available per molecule (determined in chapter 5.2.2) is blocked by atoms. Additionally the respective counter ions are sufficiently small (with the effective ion radius of the tetramethyl ammonium cation R$\approx 0.28\,nm$ and the hexafluoro phosphate anion R$\approx 0.23\,nm$[151]) to be able to diffuse towards the electrode's surface.

To estimate the effective potential S in percent at the position of the SP-LA head group z we make use of the expected potential's Debye length κ^{-1} in our system which is given according to the Debye-Hückel-theory, in case of mono-

Potential	$\|\chi_{NR}^{(2)}\|$		$\Phi\chi_{NR}^{(2)}$		$1273\,cm^{-1}$		$1307\,cm^{-1}$	
	UV off	UV on	UV off	UV on	UV off	UV on	UV off	UV on
$-720\,mV$	0.75	0.69	1.38	1.38	2.14	11.92	-4.26	-11.79
$-620\,mV$	0.81	0.70	1.42	1.30	1.77	13.88	-4.25	-13.04
$-520\,mV$	0.82	0.66	1.44	1.26	2.35	15.78	-4.31	-14.26
$-420\,mV$	0.83	0.60	1.41	1.13	3.11	17.06	-3.81	-15.07
$-320\,mV$	0.89	0.58	1.48	1.11	3.08	17.27	-4.18	-15.55
$-220\,mV$	0.91	0.62	1.50	1.13	2.51	15.85	-3.45	-14.64
$-120\,mV$	0.93	0.71	1.50	1.25	3.32	14.08	-3.62	-11.56
$-20\,mV$	0.96	0.82	1.53	1.34	3.85	11.59	-2.99	-8.50
$+80\,mV$	1.01	0.93	1.54	1.52	8.83	-2.75	-2.75	-4.97

Potential	$1331\,cm^{-1}$		$1353\,cm^{-1}$		$1423\,cm^{-1}$		$1456\,cm^{-1}$	
	UV off	UV on	UV off	UV on	UV off	UV on	UV off	UV on
$-720\,mV$	-7.91	-0.66	40.46	60.16	3.52	17.93	2.76	12.56
$-620\,mV$	-7.56	-1.24	35.86	64.22	2.70	18.05	2.31	14.40
$-520\,mV$	-7.05	-0.86	35.40	66.25	2.53	18.42	2.68	14.73
$-420\,mV$	-6.86	-1.29	32.53	70.68	2.84	18.68	2.57	16.74
$-320\,mV$	-6.11	-1.62	28.43	71.45	1.95	17.90	2.05	16.87
$-220\,mV$	-6.00	-2.01	26.35	67.34	2.03	15.25	1.77	17.06
$-120\,mV$	-5.73	-2.24	25.93	53.15	1.79	11.64	1.73	13.55
$-20\,mV$	-5.64	-2.91	23.29	42.36	1.30	7.67	2.00	10.55
$+80\,mV$	-5,26	-2.99	21.84	29.93	1.22	4.48	1.94	6.57

Potential	$1474\,cm^{-1}$		$1509\,cm^{-1}$		$1524\,cm^{-1}$		$1591\ cm^{-1}$	
	UV off	UV on	UV off	UV on	UV off	UV on	UV off	UV on
$-720\,mV$	-2.55	-9.42	1.25	31.48	4.69	-28.48	-36.03	-44.06
$-620\,mV$	-2.89	-9.80	-0.11	32.96	5.74	-26.87	-38.23	-45,60
$-520\,mV$	-3.44	-8.82	0.50	33.27	4.86	-26.73	-39.09	-46.24
$-420\,mV$	-3.14	-8.32	0.04	34.05	5.94	-24.95	-40.30	-44.60
$-320\,mV$	-3.58	-7.42	-0.84	32.11	6.02	-21.90	-41.33	-44.51
$-220\,mV$	-3.40	-7.95	-1.29	29.74	6.16	-16.97	-42.51	-44.45
$-120\,mV$	-3.96	-7.12	-0.72	21.64	5.47	-8.61	-42.48	-42.98
$-20\,mV$	-4.67	-6.24	-0.90	13.26	5.23	-0.58	-42.74	-43.09
$+80\,mV$	-5.11	-6.92	-0.07	8.55	4.08	0.08	-43.33	-43.75

Table 6.4: Amplitude evolution as a function of applied electric potential. Values obtained through global fitting.

valent ions as[152]

$$k^{-1} = \sqrt{\frac{\epsilon_r \epsilon_0 k_B T}{2e^2 c N_A}} \tag{6.6}$$

with the relative permittivity ϵ_r for acetonitrile at ambient conditions being $35.85^{[153]}$ and the electrolyte concentration $c = 100 \frac{mol}{m^3}$ we obtain the Debye-length $\kappa^{-1} \approx 0.65\,nm$ at $T = 298\,K$. Since after one Debye length the value of the applied potential has decreased to $1/e$, the effective potential can be calculated according to:

$$S = e^{(-\frac{z}{\kappa})} * 100\% \tag{6.7}$$

So if the tilt angle is zero the head group will experience $\approx 2\%$ of the applied potential. If the distance toward the surface is decreased to $2\,nm$ S will double. Using Pythagoras the corresponding tilt angle would be in this example $\approx 37°$. A tilt angle of $45°$ would lead to the effective potential of $\approx 6\%$. Given the strong electric fields associated with an applied electrical potential directly at the electrodes surface 6% of its initial value should still be felt by the SP-LA headgroup. Assumed the initial tilt angle was $45°$ and the SP-LA head group in it's closed form was slightly repelled by an applied negative potential bias, a small change in tilt angle of $\approx 8°$ towards $37°$ could compensate for an increased bias by tripling the screening making the observation of a changing tilt angle quite likely.

The actual tilt angle can be determined through polarization dependent measurements as briefly discussed in chapter 2.1.4. However, the SFG signal obtained in homodyned SSP measurements is orders of magnitudes weaker than the PPP signal due to the respective local field factors (see table 2.1 in chapter 2.1.6) and consequently cannot be detected within our setup. In heterodyned SFG measurements the SSP/PPP signal ratio is enhanced, since instead of their square the local field factors influence the heterodyned signal linearly. Also

NEXAFS (near edge x-ray absorption fine structure) measurements could help to determine the molecules' orientation at the surface,[154] but such measurements require synchroton radiation which we do not have access to. For now we can thus only speculate that the amplitude changes observed in the SFG spectra as a function of potential originate from changes in the tilt angle.

Possible Stark-Shift

As was laid out in chapter 6.1 to reduce the number of independent parameters for fitting the center frequencies were assumed to be the same in all spectra. Therefor any Stark shifts in the resonance frequencies due to the applied static electric field cannot be resolved. Due to the expected strong screening of the electric field at the position of the head group, such a shift is not expected. However, looking at the dip in the spectra of figure 6.5A a shift in its center frequency seems to appear. According to our fit this is the result of a change in the non-resonant phase which according to equation 6.3 changes the ratio between the resonances absorptive and dispersive line shape. It is worth noting, that at $0\,mV$ with respect to the open current voltage (OCV), which equals -220 mV with respect to the mercury sulfate reference electrode (MSE), the non-resonant phase takes a value which is in good agreement with the one obtained from the previously analyzed spectra were no voltage was applied to the sample (see table 6.1). Therefore Stark-shifts will not be considered any longer. The observed apparent change of center frequency upon application of a potential bias in our homodyned spectra, however, stands as a reminder of the necessity to unambiguously disentangle non-resonant and resonant features of the SFG response. This will be achieved through phase-resolved measurements.

Implication on SP-LA SAM to be used in Electrochemical Sensors: SP-Form

As is shown in this section an applied bias does not induce a ring opening in the SP-LA molecules within the SAM. Therefore the SP-LA SAM is a potential candidate to be used in an electrochemical sensor if the closed SP-form is used in its "On" state, since the detection of an analyte at a specific potential (at

least within our investigated range) will not be impaired by a sudden change into the sensor's "Off"-state (with the open MC -form present). In fact such a sensor has been realized for the 6-Nitro-BIPS head group with different linker chains in e.g.[14,129]. In the next section we will test, whether the open form is suitable to be used as the "On"-state in future electrochemical sensors as well.

6.3.2   Bias Dependence of the Photostationary State

Since the electric field did not show any effect on the SP-LA other than changing its tilt angle, we induce the switching by continuously irradiating the SAM with UV-light. Again alternatively a more positive and more negative bias is applied and an SFG spectrum is recorded at every potential step to study the bias dependence of the open MC-form. The resulting spectra are depicted in figure 6.5B. In contrast to the case of no irradiation with UV light under constant irradiation the applied bias has a tremendous effect on the resulting SFG spectrum's line shape. While at more positive values this line shape resembles the spectrum of the closed SP-form it resembles the line shape of the open MC-form at more negative potentials (see figure 6.1A for comparison).

Destabilization of MC-Form towards more Positive Potentials

The obtained spectra suggest an increasing destabilization of the MC-form with respect to the closed SP-form with an increasing positive bias. As noted previously a change in potential is likely to induce a change in the tilt angle of the molecule. Assumed this tilt angle increases for a positive potential the sterical interactions between neighboring molecules will increase (see figure 6.6). Since the closed head group needs less space than the open one sterical interactions would be reduced and subsequently the SP-form will be favored enhancing the back reaction with the ring to close ultimately getting the open MC-form to disappear. Additionally the closer proximity towards the metal enhances possible molecule substrate interactions which were shown in several studies[125,126] to limit the switching process, especially the ring opening forward reaction as discussed in chapter 2.2.3. However, as discussed in the evaluation of our SAM quality (chapter 5.2.2) a direct contact between the
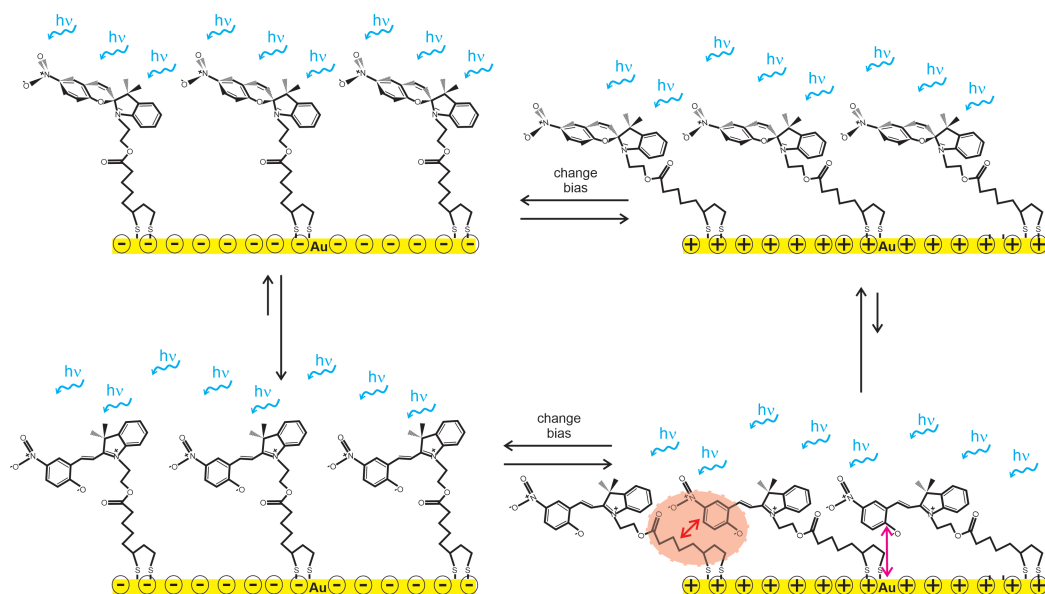
Figure 6.6: Proposed potential-dependent behavior of SP-LA SAM under constant UV irradiation as a function of applied bias. Highlighted in red is the increased sterical interaction between individual molecules within the SAM and in magenta the possible molecule/substrate interaction under an applied positive potential.

head group and the substrate should be prevented by sterical interaction and it remains unclear whether the enhanced proximity is close enough to allow such molecule substrate interactions (see figure 6.6).

Another cause for the apparent destabilization of the open form at positive potentials might be the aforementioned huge difference in dipole moments for the open and closed form ($17\,D$ and $5\,D$ respectively[111]). If sterical interactions (as a result of a tilted chain) were strong enough to impair the flexibility of the head group's arrangement the relative destabilization of the MC-form can be rationalized as a consequence of the larger dipole moment's inability to adopt an energetically favorable orientation in the electric field present at the interface at a more positive bias.

The accompanying electrolyte should not influence the photo stationary state of the head group. As described previously the electrolyte ions are sufficiently small to diffuse towards the electrode's surface which is only barely occupied by

the SP-LA. Therefore the electric double layer and in particular the Helmholtz layer which consists exclusively of the electrode potential's respective counter ions will be formed directly at the substrate's surface. The head group located at the end of the linker chain will be sufficiently far away to experience the electrolyte ions' bulk concentration unless the linker chain takes an extreme tilt angle. However, to verify whether the double layer formation in fact is not impaired by the presence of the SP-LA's anchor group one could perform impedance spectroscopy measurements to record the capacity of an uncovered and SP-LA covered gold electrode immersed in our electrolyte solution. Such measurements, however, would have required the redesign of the electrochemical cell applied in our SFG measurements.

Behavior of MC-Form towards more Negative Potentials

So the MC-form is destabilized at positive potentials. In contrast up to a potential of -420 mV vs MSE the open form is increasingly favored (see figure 6.7B for the bias dependent asymmetric NO_2-stretch amplitude, feature b, exclusively present in the MC-form). For more negative potential the amplitudes characteristic for the MC-form (e.g. feature b, d, e) apparently start to slightly decrease again (see table 6.4). However, some bands assigned to both the open and closed form also appear weaker and the symmetric NO_2-stretch (feature a) remains weak (signaling no back switch to the closed form). The reason for this behavior can be understood by taking a look at the non-resonant susceptibility's potential-dependent magnitude in table 6.4 and figure 6.7A. As discussed in chapter 6.1.4("Fitting Ambiguities") and evident from equation 6.3 the resonant amplitude and $|\chi_{NR}^{(2)}|$ form a product so an increase in one quantity can somewhat compensate a decrease in the other one. Although the square of $|\chi_{NR}^{(2)}|$ gives a specific constant off-set (see equation 6.2) this off set and thus $|\chi_{NR}^{(2)}|$ itself is difficult to determine in our case with too many resonances present. In this regard it is revealing that the apparent $|\chi_{NR}^{(2)}|$ takes a minimum at -320 mV/-420 mV vs MSE and increases again for more negative values as opposed for the $|\chi_{NR}^{(2)}|$ in the non switched case which steadily decreases for negative potentials. If one corrects for this effect by multiplying the
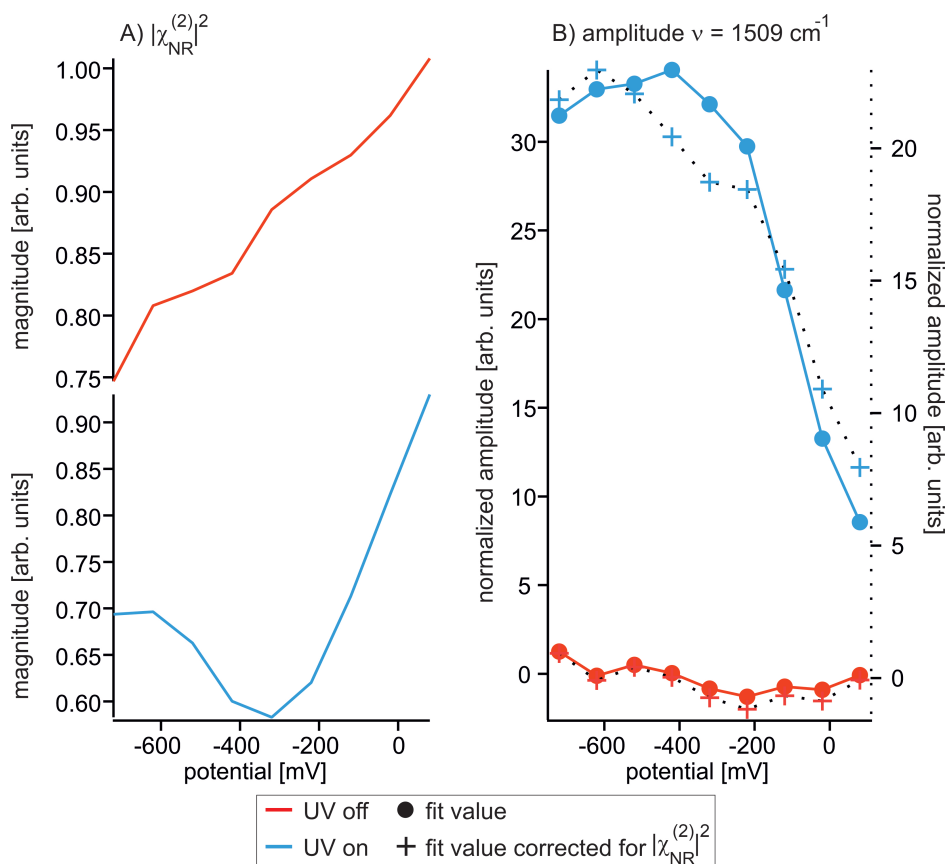
Figure 6.7: Potential-dependence of A) the magnitude square of the non-resonant second order susceptibility and B) the intensity of the asymmetric NO_2-stretch, which is shown as obtained through fitting and also shown corrected for $|\chi_{NR}|$.

amplitude with the corresponding value of $|\chi_{NR}^{(2)}|$ the amplitude of the asymmetric NO_2-stretch and accordingly the number of molecules in the MC-form increases until -520 mV and then reaches a constant value (within the reach of uncertainty), indicating that at that point all molecules have been switched to the open form.

The non-resonant phase for the UV switched and native case indicate a comparable bias dependent evolution as the respective magnitudes. While in the native case the phase decreases almost linearly (figure 6.8A) in the switched case it decreases from positive potential to reach a minimum at -320 mV and then
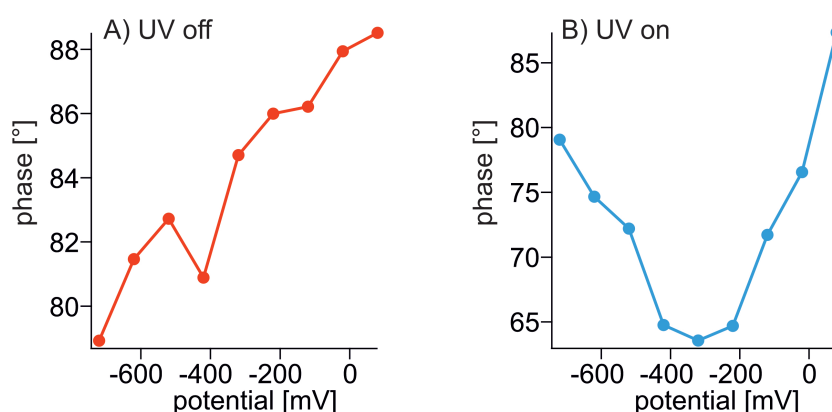
Figure 6.8: Potential-dependence of the non-resonant phase. A) UV off. B) UV on.

increases again (figure 6.8B). Interestingly for strongly positive and negative potential the phases in the switched and native cases converge to similar values. Provided the fit is correct, this would underscore the influence of the open form's large dipole moment on the non-resonant phase of the gold substrate. Under UV irradiation at strongly positive potentials the number of molecules in the MC-form is negligibly low and about the same as in the unswitched case. Hence in both cases the resolved phases take almost equal values. At moderate potentials the population of the MC-form increases and its dipole moment starts to influence Φ_{NR}. Now Φ_{NR} for the switched and unswitched case strongly diverge. At strongly negative potentials the population of MC as discussed before presumably reaches a stable maximum. However, at some point the influence of the MC head group on the substrates phase is starting to be outweighed by the applied bias after which the values of the respective phases start to approach each other again.

Implication on SP-LA SAM to be used in Electrochemical Sensors: MC-Form

As is shown in this section the equilibrium between the open MC and closed SP-form for the SP-LA SAM under constant irradiation is largely influenced by an applied electric potential. An applied positive potential forces the open

MC-form into the closed SP-form within less than 1 minute, while a negative potential stabilizes the MC-form. This impairs the use of the MC-form in smart electrodes and electrochemical sensors as their "On" state, since the desired electrochemical processes at these electrodes would be limited to the potential region below -520 mV vs MSE. Below this potential the population of molecules in the MC-form is stable and the detected electrochemical processes only depends on the analyte (or reactant) concentration in solution. Towards more positive values it depends on both the analyte concentration and the respective MC population making the quantitative evaluation of the desired electrochemical process complicated. However, there are no restrictions for the MC-form to be used as the "Off" state of such electrodes. In fact the additional stimulus to stabilize this "Off"-state (or destabilize the "On"-state) by going to negative potentials might overcome problems to completely switch off such electrodes as experienced in[14]. Here the molecular switch/analyte interactions lead to the stabilization of the closed SP-form corresponding to the "On"-state such that interconversion to the open MC-form was severely impaired, preventing the sensor to entirely switch to its "Off"-state (by illuminating with UV light).

6.3.3 Potential-Dependent Switching Kinetics

The potential-dependence of the ring opening kinetic is monitored. The kinetic measurements are conducted the same way as the non-potential-dependent kinetic measurements in section 6.2, which means constantly taking SFG spectra (1 per mS) and averaging 20'000 SFG spectra for one time point ($\equiv$ one time point every 20 s) while the sample is irradiated with UV light. Additionally different negative static electric bias' are applied. Between measurements the sample is shortly held ($\approx 1 \, min$) at +80 mV to destabilize the open MC-form (see previous section) and quickly switch back the sample into its closed initial form.

The following data analysis is performed using the two peaks assigned to the $C-N^+$-stretch and asymmetric NO_2-stretch at 1307 cm^{-1} and 1509 cm^{-1} respectively, because their temporal evolution can be exclusively related to one of the two sub-processes of the SP-LA switching, namely the $C-O$-bond break-
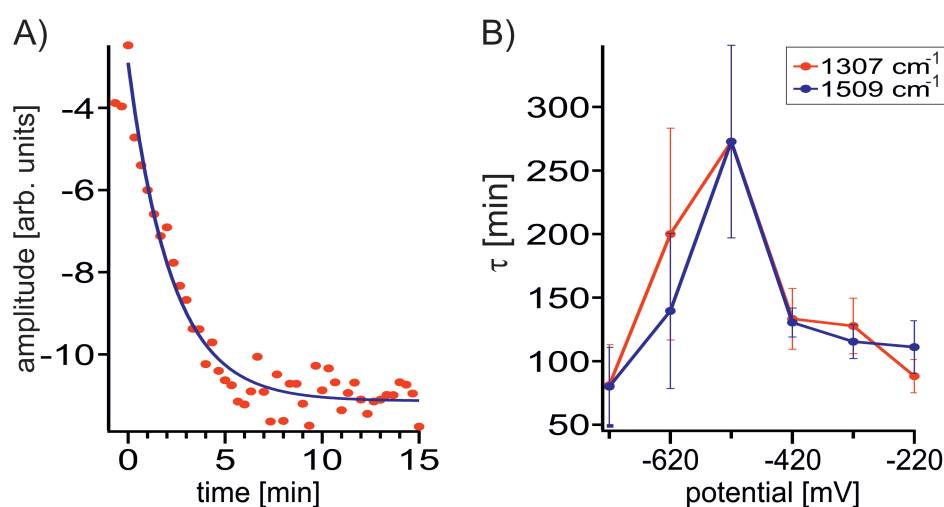
Figure 6.9: A) Kinetic evolution of the peak at $1307\,cm^{-1}$ at a potential of -420 mV. B)Time constants for the peak evolution at $1307\,cm^{-1}$ and $1509\,cm^{-1}$ as a function of potential.

ing of the spiro-center and the subsequent reorientation of the head group as was pointed out in section 6.2 and figure 6.3.

To obtain the respective timescale of interest each peak amplitude evolution over time is approximated with a mono-exponential fit (see figure 6.9A) since, as pointed out in chapter 6.2 where we used a bi-exponential fit function the very slow second process observed could not be assigned to the head group re-orientation but rather to an overall reorganization of the whole SP-LA molecule within the SAM expected to be present only in the very first switching cycle.[127] The resulting time constants are listed in table 6.5 and displayed as a function of applied bias in figure 6.9.

Both resonances seem to follow the same kinetics and their time constants for a respective potential are similar within the margin of fitting error. This is unexpected since the reorientation of the head-group requires the negatively charged oxygen atom of the former spiro-center to get closer to the electrode (see figure 6.3). Hence at a negative bias the reorientation should be slowed down with respect to the bond break. However potential screening might be efficient enough, so that reorientation is not sufficiently slowed down to be independently resolved in our 20 second averaged data points. To probe that

Potential $[mV]$	$1307\,cm^{-1}$		$1509\,cm^{-1}$	
	$\tau_1^{-1}\,[min^{-1}]$	$\tau_1\,[s]$	$\tau_1^{-1}\,[min^{-1}]$	$\tau_1\,[s]$
-720 mV	0.74±0.14	81±32	0.75±0.14	80±31
-620 mV	0.3±0.06	200±84	0.43±0.09	140±62
-520 mV	0.22±0.03	273±76	0.22±0.03	273±76
-420 mV	0.45±0.04	133±24	0.46±0.02	130±12
-320 mV	0.47±0.04	128±22	0.52±0.03	115±14
-220 mV	0.68±0.05	88±14	0.54±0.05	111±21

Table 6.5: Time constants potential-dependent switching kinetics.

one could repeat those measurements with a smaller electrolyte concentration to increase the Debye length and attenuate the potential screening, or use a method were less averaging is required to acquire spectra which are not dominated by noise.

Although the two sub processes cannot be resolved individually within our measurement, it is interesting to see that the switching process on the whole seems to be slowed down up to a bias of -520 mV vs MSE (see figure 6.9B). Why this trend is reversed for more negative potential, however, is unclear. Given the large error margins of the time constants this point could also be an artifact. The kinetic of the switching process towards the open form than would be basically independent of the applied potential indicating sufficient screening.

6.3.4 Summary of Potential-Dependent Homodyned SFG Measurements

The homodyned SFG measurements of SP-LA provided an insight into the bias dependent SP/MC equilibrium in the presence and absence of UV irradiation despite the discussed uncertainties regarding fitting. Without irradiation the equilibrium is largely shifted towards the closed form regardless of an applied electric potential within the investigated range. In contrast under constant irradiation the equilibrium is effectively shifted towards the SP-form at positive potentials and to the MC-form at negative potentials. This behavior has imme-

diate consequences on the potential use of SP-LA in functionalized electrodes, depending on which state of the molecular switch (open or closed form) is present in the "On" state and which in the "Off" state. The assignment to the "On" and "Off" state, however, is not a free choice but depends on the ability of one form (assigned to the electrode's "On" state) to interact with a desired reactant or analyte while the other form (assigned to the electrode's "Off" state) shows no interaction.

As was already pointed out in chapter 6.3.1 in this "On" state within the electric potential range of the desired electrochemical reaction the population of the respective molecular switch form should be constant and independent of bias so that the observed reaction rate only depends on the reactant's (or in case of sensors the analyte's) concentration and not on the degree to witch the sensor is switched to its "On" state. If the open MC-form corresponds to the "On" state that would limit the use of the "smart" electrode towards electrochemical reactions taking part below a potential of -520 mV vs MSE, since at more positive potentials the MC-form becomes increasingly destabilized and the electrode would ultimately be switched "Off". Therefor the electrochemical reaction of the desired species must fall into that limit.

If the closed SP-form corresponded to the electrode's "On" state there would be no limitations to the electrochemical reaction within the investigated potential range. The additional destabilization of the MC-form with an applied bias then would actually be beneficial since it would allow to switch faster from the "Off" to the "On" state as explained in the following. Without an applied bias switching from the MC to the SP-form is achieved thermally by stopping the constant irradiation of the electrode with UV light. This thermal backreaction happens on the timescale of hours[127] for the SAM in air, or for the free 6-Nitro-BIPS head group depending on the solvents polarity in several minutes in acetonitrile[155] to hours in ethanol[156]. Alternatively we now can switch off the UV light and additionally apply a positive bias switching the molecule into the SP-form (the presumed "On" state) within a minute (see the potential-dependent SFG spectra in figure 6.5 which were taken each 1 minute after the respective potential was applied). It needs to be added that the back switch time in air could also be significantly reduced if additionally light in the vis-

ible frequency range was shone onto the sample to around ten minutes.[127] However, apart from still being faster the ability to switch the SAM via electric potential perturbation removes complexity from any sensor as e.g light at only one frequency is required.

The possibility to stabilize the MC-form (assumed to be the "Off"-state) at negative potentials (while additionally irradiating with UV light) is also beneficial since it helps to overcome problems in switching the electrode "Off". Willner et. all[14] for instance saw a stabilization of the SP-form in their immunosensor due to the closed form's interaction with the present analyte. This stabilization lead to a significant portion of the molecular switch population to remain in its SP-form even under UV irradiation. The additional application of a negative bias might help in such cases to shift the SP/MC-equilibrium towards the open MC-form, more effectively switching "Off" the electrode and thus enhancing the reusability of Spiropyran embedded immunosensors. The potential-dependent kinetic measurements have shown, that such an "Off"-state can be reached within 2-4 minutes.

Chapter 7

Application of High-Accuracy Phase-Resolved SFG Spectroscopy

The previous chapter illustrated the capabilities and limitations of homodyned SFG using the example of a self-assembled monolayer (SAM) of the spiropyran derivative SP-LA. With this method we were able to e.g. monitor the SAM's behavior under the irradiation with UV light and an additional applied electric potential. However, some problems remained like e.g. the determination of the molecules' absolute orientation and the accuracy of spectra fitting. The following chapter shall discuss how to obtain additional information using the high-accuracy phase-resolved SFG setup presented in chapter 3 to solve or at least minimize those remaining issues. For this purpose phase-resolved spectra of bare gold and a model system, a SAM of 1-octadecanethiol (ODT) on gold, are evaluated. The thereby obtained knowledge of data treatment and interpretation will ultimately be transferred to phase-resolved SFG measurements on the SP-LA SAM on gold.

7.1 Heterodyned Data Evaluation

7.1.1 Data Preparation

In the following the steps will be presented, that need to be undertaken to evaluate the obtained heterodyned spectra. As pointed out in chapter 3.1.2 the collinear approach within the phase-resolved SFG setup allows to perform these measurements with quasi simultaneous referencing. The reference spectrum S_{ref}, usually taken off a bare gold or z-cut alpha-quartz surface, is ultimately used to normalize the sample spectrum S_{sam} to obtain S_{norm} according to:

$$S_{norm} = \frac{S_{sam}}{S_{ref}} \tag{7.1}$$

The complex spectra $S_{sam/ref}$ contain the respective effective nonlinear second order susceptibility $\chi^{(2)}_{eff;sam/ref}$, that equals the sum of the probed susceptibility's tensor components $\chi^{(2)}_{ijk}$ (depending on the incoming fields actual polarization $\vec{e}$), multiplied by the effective local field Fresnel factor F composed of the respective individual factors L (compare equation 2.17 in chapter 2.1.4):

$$\chi^{(2)}_{eff} \cdot F = \sum_{i}^{x,y,z} \sum_{j}^{x,y,z} \sum_{k}^{x,y,z} L_{ii}(\omega_{SFG})\vec{e}_i \chi^{(2)}_{ijk}(\omega_{SFG}) \\ L_{jj}(\omega_{Vis})\vec{e}_j\vec{\epsilon}_{Vis} L_{kk}(\omega_{IR})\vec{e}_k\vec{\epsilon}_{IR} \tag{7.2}$$

The normalized complex spectrum is additionally influenced by the different phase shift Φ_{LO} the local oscillator experiences when being reflected from the sample/reference surface. A total description of the normalized complex spectrum therefore yields:

$$S_{norm} = \frac{F_{sam}\chi^{(2)}_{sam}e^{-i(\Phi_{LO_{sam}})}}{F_{ref}\chi^{(2)}_{ref}e^{-i(\Phi_{LO_{ref}})}} \tag{7.3}$$

The normalized spectral phase $\Phi_{S_{norm}}$ is then given by:

$$
\begin{aligned}
\Phi_{S_{norm}} &= (\Phi_{S_{sam}} - \Phi_{LO_{sam}}) - (\Phi_{S_{ref}} - \Phi_{LO_{ref}}) \\
&= (\Phi_{F_{sam}} + \Phi_{\chi^{(2)}_{sam}} - \Phi_{LO_{sam}}) - (\Phi_{F_{ref}} + \Phi_{\chi^{(2)}_{ref}} - \Phi_{LO_{ref}})
\end{aligned}
\tag{7.4}
$$

and its magnitude $|S_{norm}|$ by:

$$
|S_{norm}| = \frac{|S_{sam}|}{|S_{ref}|} = \frac{|F_{sam}||\chi^{(2)}_{sam}|}{|F_{ref}||\chi^{(2)}_{ref}|}
\tag{7.5}
$$

Ideally if sample and reference are the same, $\Phi_{S_{norm}}$ should be zero and $|S_{norm}|$ be one. However, since the sample and reference signal are taken at two different spots slight differences in their subsequent detection paths (e.g. the angle certain lenses are hit) and the way they are recombined introduce different relative shifts between the orthogonally polarized local oscillator and signal SFG. Therefore a complex transfer function f_T must be determined by placing two equal samples in both positions and perform a measurement as was done on a gold surface in figure 7.1. Inserting f_T into equation 7.1 the corrected normalized spectrum S_{norm} is given by:

$$
\begin{aligned}
S_{norm} &= \frac{F_{sam}\chi^{(2)}_{sam}e^{-i(\Phi_{LO_{sam}})}}{F_{ref}\chi^{(2)}_{ref}e^{-i(\Phi_{LO_{ref}})} \cdot f_T} \\
&= \frac{|F_{sam}||\chi^{(2)}_{sam}|}{|F_{ref}||\chi^{(2)}_{ref}||f_T|} e^{i[(\Phi_{F_{sam}}+\Phi_{\chi^{(2)}_{sam}}-\Phi_{LO_{sam}})-(\Phi_{F_{ref}}+\Phi_{\chi^{(2)}_{ref}}-\Phi_{LO_{ref}})-\Phi_{f_T}]}
\end{aligned}
\tag{7.6}
$$

It is worth noting that the change in SFG wavelength over the observed IR frequency range in figure 7.1 is small enough so that the non-resonant phase can safely assumed to be constant for the whole range. The inter-band transition into the d-bands at $2.5\,eV$ ($\omega \approx 500\,nm$)[157] are sufficiently far away so that $\chi^{(2)}_{inter}$ should stay constant over the observed SFG range. Likewise $\chi^{(2)}_{intra}$ should
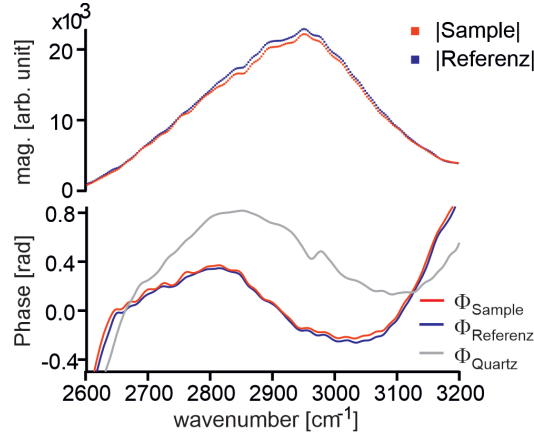
Figure 7.1: Magnitude (upper graph) and phase (lower graph) of a complex spectrum of bare gold taken simultaneously at the reference (blue) and sample (red) position. For comparison the phase of a previously taken spectrum of quartz (gray) is plotted.

be constant since it is proportional to the dielectric constant $\epsilon(\omega_{SFG})$[45] which for a Drude like metal with a plasma frequency ω_P is given by:[47,78,158]

$$\epsilon(\omega) = 1 - (\frac{\omega_P}{\omega})^2 \approx -(\frac{\omega_P}{\omega})^2 \tag{7.7}$$

and changes from $\approx$-21.0 to $\approx$-22.4 (gold:ω_P =9.08,[159] ω_{IR} =2065-3100cm^{-1}). Hence the ratio of (the real) $\chi^{(2)}_{intra}$ to (the imaginary) $\chi^{(2)}_{inter}$ and consequently the phase of $\chi^{(2)}_{NR}$ (see chapter 2.1.5) should be constant.

The change in phase with the wave length in figure 7.1 is related to the intrinsic phases of the pump pulses and the LO and will vanish upon referencing. This is supported by a similar change in phase for a comparable measurement on quartz also shown in figure 7.1.

7.1.2 Determination of Φ_S with an Absolute Reference

The influence of the substrate's non-resonant susceptibility's phase, $\Phi_{\chi^{(2)}_{Au}}$, on the line shape of homodyned SFG spectra which impairs spectral interpreta-
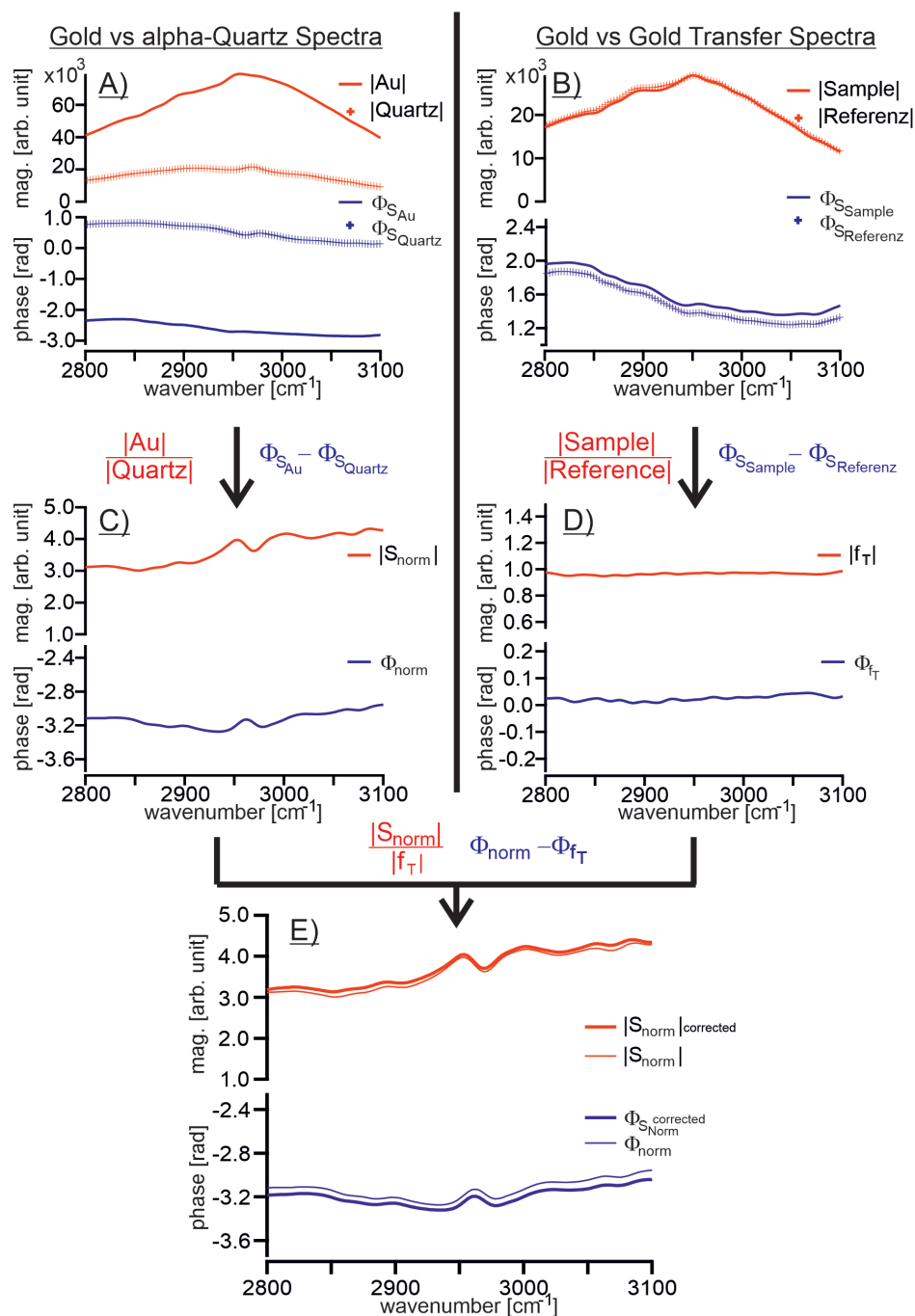
Figure 7.2: Steps to be taken to relate the spectrum to a known phase (A and C) and correction for inaccuracies due to the sample and reference spectrum taken at different spots via a transfer function (B, D and E).

tion has been extensively discussed in previous chapters. Precise knowledge of this phase would be favorable but is often not available. To gain this critical information in the case of gold in a first step the absolute phase of a phase-resolved spectrum of a bare gold mirror, $\Phi_{S_{Au,abs}}$ is determined. In order to determine the absolute phase of the non-resonant gold response we need a) an absolute phase reference and b) the complex transfer function f_T to quantify the differences that arise due to the spectra being taken at the two different positions depending critically on the beam path alignment (see previous section and equation 7.6).

As absolute reference z-cut alpha-quartz is typically used. Because of its non-centrosymmetric crystal structure which allows for the generation of second order nonlinear signals the SFG response is dominated by the bulk term. The off-resonant phase of this bulk-response displays $\Phi_{S_{Quartz}} \equiv \pm 90°$ (the sign depends on the crystal's orientation), which is why z-cut alpha-quartz can be used as a standard phase reference. Its is worth noting, however, that we found the actual phase slightly shifted to $\approx \pm 94°$.[140] This small but significant deviation from the ideal value of $\pm 90°$ originates from the impact of the surface contribution to the overall SFG response.

Figure 7.2A displays the complex spectra of the simultaneously measured gold mirror at the sample place (line) and the quartz crystal at the reference position (markers), split into their magnitude (red) and phase (blue) (see equation 7.5 and 7.4 respectively). Since the non-resonant gold response is much stronger than the quartz response the SFG signal and the LO are attenuated using a filter behind the gold sample. The magnitude of the gold spectrum is divided by the quartz spectral magnitude, while the phases are subtracted from each other. The results are displayed in figure 7.2C.

To determine f_T two spectra are taken in an analogue simultaneous measurement, with the gold mirror present in both, the sample and reference spot (see figure 7.2B). Similarly the magnitude of the "sample" spectrum is divided by the "reference" spectrum magnitude, and the reference phase is subtracted from the sample phase. The resulting f_T is shown in figure 7.2D. Its phase needs to be subtracted from the previously determined phase difference of the gold vs. quartz measurement, its magnitude quotient acts as a divisor for

113

the previously obtained magnitude quotient (see equation 7.6). The resulting normalized and corrected spectral phase and magnitude are displayed in figure 7.2E (bold lines), along with the uncorrected ones for comparison (faint lines).

To finally determine the phase difference between the gold mirror's spectral response and that of quartz the corresponding values around the spectral center frequency located at $\approx 2960\,cm^{-1}$ (2900-3050 cm^{-1}) were averaged to yield -3.23±0.01 rad or -185.1°±0.5°. To obtain $\Phi_{S_{Au},abs}$ we use equation 7.4 and the phase shifts for the reflected S-polarized local oscillator which is incident on the sample at an angle of 70° on quartz[160] and gold[161], 180.0° and -169.5° respectively. Plugging these values into 7.4 we get (our quartz phase being negative, -94°):

$$\Phi_{S_{Au},abs} = (\Phi_{F_{Au}} + \Phi_{\chi^{(2)}_{Au}}) = -185.1° + (-169.5°) + (-94° - 180°)$$
$$= \underline{-628.6°} \equiv \underline{\underline{91.4°}} \tag{7.8}$$

Now that the gold mirror's absolute spectral phase has been determined, it can in turn serve as a reference in subsequent measurements. Because gold yields an appreciable SFG response at significantly lower power of the incident beams compared to quartz simultaneously referenced measurements on delicate samples with a low damage threshold such as self-assembled monolayers of organic molecules now become possible.

7.1.3 Implications of Determined $\Phi_{S_{Au},abs}$

The determined absolute spectral phase of the gold mirror's non-resonant second order response equals 91.4°. This value is close to the 85° derived by Potterton et. al.[141] in homodyned SFG measurements for $\Phi_{\chi^{(2)}_{Au}}$. It is worth noting that they applied an IR beam of same frequency as in our experiment but an up conversion beam of $\omega =$ 532 nm which is much closer to the s→d inter-band transition of gold around $\omega \approx$ 500 nm.[157,158,162] A phase of $\approx \frac{\pi}{2}$

for a $532\,nm$ upconversion frequency has also been reported elsewhere.[40,148] The similarity to our result suggests, that for an upconversion beam of $800\,nm$ (and for the subsequent SFG frequency of $\approx 650\,nm$) inter-band transitions still play a major role contributing to $\chi_{NR}^{(2)}$. However, equation 7.8 makes it clear, that we cannot disentangle the phase contribution arising from the complex local field factors and the actual phase of $\chi_{Au}^{(2)}$. As discussed in the Theory (see chapter 2.1.4) to determine the local field factor for the z-component L_z knowledge about the interfacial refractive index, that influences the magnitude of L_z, is necessary,[37,40] which so far can only be obtained through theoretical calculation.[56] This value has been extensively discussed in the literature and among others led to conflicting results in the determination of the orientation of surface molecules.[76] However, since the local field factors influence both, the resonant and non-resonant susceptibilities the analysis of a spectrum of a self-assembled monolayer on a gold substrate might help to estimate the field factors influence .

7.1.4 Fitting Resonances in Phase-Resolved Spectra

To evaluate a phase-resolved vibrational SFG spectrum of a self-assembled monolayer (SAM) the spectrum has to be normalized by the reference spectrum and corrected by the transfer function as was outlined in the previous chapter according to equation 7.6. The magnitude and phase of an ODT SAM spectrum on gold taken in air is shown before normalization along with the simultaneously taken gold reference spectrum in figure 7.3A and after normalization and correction in figure 7.3B. The so obtained complex spectrum S_{norm} is transferred from its polar to its Cartesian form (see figure 7.3C) so that its real part can be fitted according to:

$$Re\{S_{norm}(\omega)\} = |\chi_{NR}^{(2)}|cos(\Phi_{S_{norm},NR})$$
$$+ cos(\Phi_{S_{norm},R})\sum_{\nu}(\frac{A(\omega_{\nu}-\omega)}{(\omega_{\nu}-\omega)^2+\Gamma_{\nu}^2}) - sin(\Phi_{S_{norm},R})\sum_{\nu}(\frac{A\Gamma_{\nu}}{(\omega_{\nu}-\omega)^2+\Gamma_{\nu}^2})$$
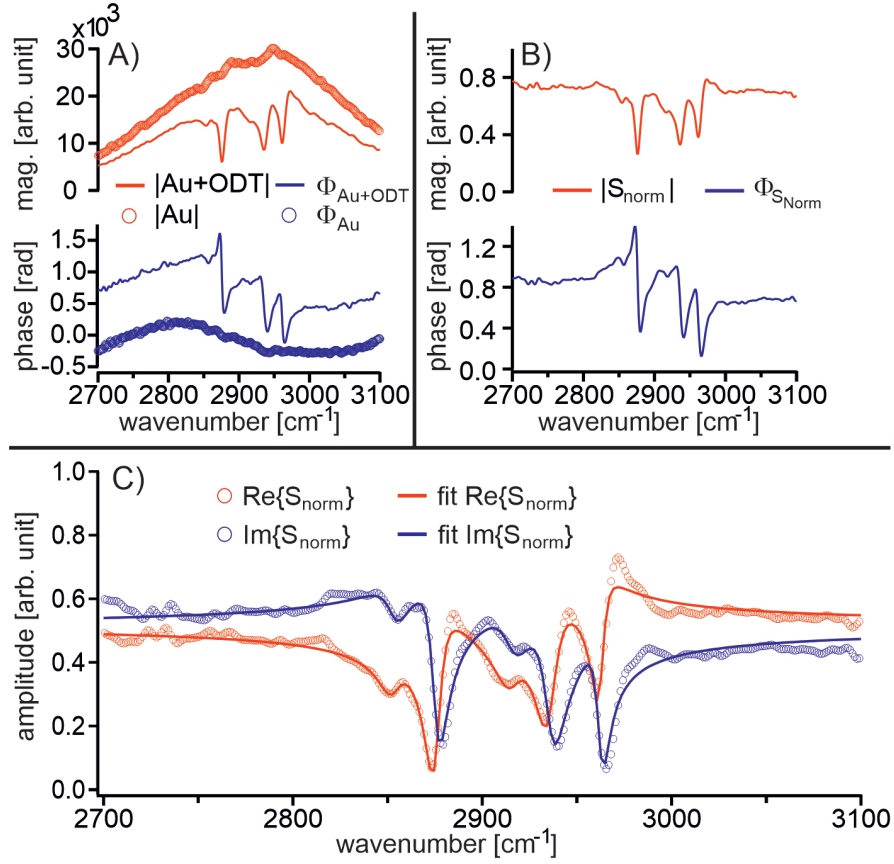
$$(7.9)$$

Figure 7.3: A) Magnitude (red) and phase (blue) of the sample (Au+ODT) and reference (Au) spectrum. B) Magnitude and phase of the normalized and f_t-corrected sample spectrum S_{norm}. C) Real (red) and imaginary part (blue) of S_{norm} and their respective fit.

while simultaneously in a global fit its imaginary part can be fitted to:

$$Im\{S_{norm}(\omega)\} = |\chi_{NR}^{(2)}|sin(\Phi_{S_{norm},NR})$$
$$+ sin(\Phi_{S_{norm},R}) \sum_\nu (\frac{A(\omega_\nu - \omega)}{(\omega_\nu - \omega)^2 + \Gamma_\nu^2}) + cos(\Phi_{S_{norm},R}) \sum_\nu (\frac{A\Gamma_\nu}{(\omega_\nu - \omega)^2 + \Gamma_\nu^2})$$

$$(7.10)$$

Note that in these equations $\Phi_{S_{norm}}$ is split into a non-resonant part $\Phi_{S_{norm},NR}$ and a resonant one $\Phi_{S_{norm},R}$.

Assign.		Value	Assign.		Value
$S_{norm,NR}$	$|S_{norm,NR}|$	0.73±0.01	$S_{norm,NR}$	$\Phi_{S_{norm,NR}}$	44.60°±0.13°
$\nu_{sym}(CH_2)$	A	-0.76±0.10	$\nu_{sym}(CH_3)$	A	-2.42±0.07
	ω_q	2853±1		ω_q	2876±1
	Γ_q	7.07±1.01		Γ_q	5.04±0.18
$\nu_{asym/Fermi}(CH_2)$	A	-1.26±0.14	$\nu_{Fermi}(CH_3)$	A	-2.67±0.13
	ω_q	2916±1		ω_q	2936±1
	Γ_q	8.88±1.00		Γ_q	7.00±0.33
$\nu_{asym}(CH_3)$	A	-1.47±0.06	$S_{norm,R}$	$\Phi_{S_{norm,R}}$	-47.45°±0.93°
	ω_q	2962±1			
	Γ_q	3.94±0.20			

Table 7.1: Fitting parameters for the normalized ODT SAM spectrum at gold (displayed in figure 7.3). Vibrational assignment according to [141].

The advantage compared to the homodyned data fitting is therefore not only the suppressed interference of the non-resonant susceptibility with the resonant one as was outlined in chapter 2.1.6, but moreover the additional constraint onto the fitting parameters that need to be equal in the fit for the real and imaginary parts of S_{norm}. The corresponding fitting values are listed in table 7.1.

The obtained center frequencies for the symmetric methyl group stretch, its Fermi resonance and the antisymmetric stretch at $2876\,cm^{-1}$, $2936\,cm^{-1}$ and $2962\,cm^{-1}$ respectively are in excellent agreement with literature values from homodyned data ($2876\,cm^{-1}$, $2936\,cm^{-1}$ and $\approx 2960\,cm^{-1}$ respectively). [141] The additional vibrations at $2853\,cm^{-1}$ and $2916\,cm^{-1}$ can be assigned to stretches of the methylene groups in the ODT chain. In a perfect SAM these resonances are absent because there the methylene groups lie in a locally centrosymmetric environment and are consequently SFG inactive. [40,141] Their presence indicates the presence of gauche defects in our SAM where the ODT chains are not aligned in an all trans confirmation but exhibit some bends.

7.1.5 Determining the Phase of the Gold Substrate's Non-Resonant Susceptibility $\Phi_{\chi_{Au}^{(2)}}$

Equation 7.4 in section 7.1.1 summarized all contributions that determine the phase of the referenced spectrum S_{norm} for the case that the transfer function is either ignored as was back then or if S_{norm} is already corrected for it as was done for the ODT spectrum in figure 7.3 before fitting. The substrate for the ODT self-assembled monolayer is gold. Likewise the substrate in the reference position is gold. Assuming the SAM does not substantially influence the reflectivity of the local oscillator off gold the induced phase shift on both surfaces is the same and $\Phi_{LO_{Sam}}$ and $\Phi_{LO_{Ref}}$ just cancel each other. Additionally one can introduce the absolute spectral phase of the reference gold mirror $\Phi_{S_{Au},abs}$ as determined in the previous chapter. Equation 7.4 then becomes:

$$\begin{aligned} \Phi_{S_{norm}} &= \left[\Phi_{S_{sam},abs} - \Phi_{S_{Au},abs}\right] \\ &= \left[(\Phi_{F_{SAM}} + \Phi_{\chi_{sam}^{(2)}}) - \Phi_{S_{Au},abs}\right] \end{aligned} \tag{7.11}$$

or, if one looks only onto the resonant part:

$$\begin{aligned} \Phi_{S_{norm},R} &= \left[\Phi_{S_{sam},R,abs} - \Phi_{S_{Au},abs}\right] \\ &= \left[(\Phi_{F_{sam}} + \Phi_{\chi_{sam}^{(2)},R}) - \Phi_{S_{Au},abs}\right] \end{aligned} \tag{7.12}$$

In the absence of any phase shift due to $\Phi_{S_{Au},abs}$ and $\Phi_{F_{sam}}$, $\Phi_{S_{norm},R}$ should equal zero, so that the dispersive line shape due to resonances occurs entirely in the real part of S_{norm} and accordingly the absorptive line shape entirely in its imaginary part (see equation 7.9 and 7.10 for $Re(S_{norm})$ and $Im(S_{norm})$ respectively). In other words $\Phi_{\chi_{sam}^{(2)},R}$ must equal zero.

The absolute spectral phase of the reference gold $\Phi_{S_{Au},abs}$ has been determined previously to be 91.4 °. With the fit parameter for $\Phi_{S_{norm},R}$ which equals $\approx$-47.5° (see table 7.1) it is possible to calculate $\Phi_{F_{sam}}$:

$$\Phi_{F_{sam}} = \Phi_{S_{norm},R} + \Phi_{S_{Au},abs} = -47.5° + 91.4° = \underline{\underline{43.9°}} \qquad (7.13)$$

Now that the phase of the local field factors for a gold surface covered with ODT is known, $\Phi_{F_{sam}}$ can be used to calculate the non-resonant susceptibilities phase for such a surface by looking at the non-resonant part of the normalized spectrum:

$$\begin{aligned}\Phi_{S_{norm},NR} &= \left[\Phi_{S_{sam},NR,abs} - \Phi_{S_{Au},abs}\right] \\ &= \left[(\Phi_{F_{SAM}} + \Phi_{\chi_{sam}^{(2)},NR}) - \Phi_{S_{Au},abs}\right]\end{aligned} \qquad (7.14)$$

With the normalized non-resonant spectral phase $\Phi_{S_{norm},NR}$ fitted to be 44.6°, $\Phi_{\chi_{sam}^{(2)},NR}$ becomes:

$$\Phi_{\chi_{sam}^{(2)},NR} = \Phi_{S_{norm},NR} - \Phi_{F_{SAM}} + \Phi_{S_{Au},abs} = \underline{\underline{92.1°}} \qquad (7.15)$$

The calculated value for $\Phi_{\chi_{sam}^{(2)},NR}$ of 92.1° should not be confused with the value of the bare gold mirror's absolute spectral phase $\Phi_{S_{Au},abs}$ of 91.4°. The ODT covered gold mirror's absolute spectral (non-resonant) phase equals 136.0°.

The result for $\Phi_{\chi_{sam}^{(2)},NR}$ suggests that $\chi_{NR}^{(2)}$ is dominated by its imaginary part and hence according to equation 2.20 its main source are inter-band transitions, that for pure gold are located at $\approx 500\,nm.$[157,158,162] It is, however, so far not possible to estimate the effect of the ODT SAM onto the $\chi_{NR}^{(2)}$ of pure gold, specifically how the covalent bonds formed between the gold and the molecules' thio-group influence the energy levels of the gold's bound and Fermi level. Under the assumption that the nonlinear Fresnel factor's phase does not change upon ODT adsorption (a change in the interfacial refractive index due to the present ODT SAM would only change its magnitude), the corresponding $\Phi_{\chi_{sam}^{(2)},NR}$ of the bare gold mirror would equal 47.5°, indicating an almost equal contribution of inter-band and intra-band transitions to the nonlinear substrate

response. Within this assumption the presence of the ODT SAM would either enhance the contribution of inter-band transitions or quench the contribution of intra-band transitions, or both.

7.1.6 Effect of Surface Treatment and Polarization Combination on the Absolute Spectral Response

The previous section has shown a massive shift in the absolute (non-resonant) spectral phase $\Phi_{S_{sam},NR,abs}$ of the gold substrate due to the presence of the ODT SAM (91.4° for the bare substrate to 136.0° for the ODT covered substrate). It is worth noting, however, that even in the absence of a SAM the absolute spectral response for different gold surfaces can differ, based on their previous surface treatment. The previously discussed gold substrate is a commercially available gold mirror which has been exposed to ozone in an ozonator for several tens of minutes to get rid of possible organic contaminants. For comparison we repeat the measurements on a freshly prepared (via physical vapor deposition) gold film under PPP and SSP polarization combination (see table 7.2). The absolute spectral phase determination of the bare substrate (and therefore entirely non-resonant) is again conducted against z-cut alpha-quartz. As opposed to the 91.4° obtained for the ozonized gold mirror, $\Phi_{S_{sam},NR,abs}$ for the freshly prepared gold film is shifted by almost 40° to 128.8° ($\Phi_{S_{sam},NR,abs}$ obtained under SSP polarization combination being 118.1°).

The phase of the local field factors are again determined via fitting of the spectra of an ODT SAM which is formed on the freshly prepared gold film as outlined in section 7.1.4 and 7.1.5. The spectra taken under PPP and SSP polarization combination and a detailed evaluation of the obtained fitting parameters can be seen in the appendix (figure A13 and table A3). The resulting $\Phi_{F_{SAM}}$ is given in table 7.2. Interestingly the determined 67.0° in case of the PPP measurement is in closer agreement with the calculated phase of the effective local field Fresnel factor of 79.1° (see table A1 in the appendix). In the case of the SSP the obtained -155.9° is even closer to the calculated phase of -160.5°.

The massive shift in $\Phi_{S_{sam},NR,abs}$ due to the presence of ODT previously observed for the case of the ozonized substrate is also present here in the case of PPP

Sample	Pol. Comb.	$\Phi_{S_{sam},NR,abs}$	$\Phi_{F_{sam}}$	$\Phi_{\chi_{sam}^{(2)},NR}$
a) Ozonized Au Mirror	PPP	91.4°	43.9°*	47.5°
b) freshly prepared Au surface	PPP	128.8°	67.0°*	61.8°
	SSP	118.1 °	-155.9°*	-86.0°
ODT SAM on a)	PPP	136.0 °	43.9°	92.1°
ODT SAM on b)	PPP	151.0°	67.0°	84.0°
	SSP	119.7°	-155.9°	-84.4°

Table 7.2: Measured values for the absolute non-resonant spectral phase $\Phi_{S_{sam},NR,abs}$. *The corresponding Fresnel shift $\Phi_{F_{sam}}$ has been obtained through fitting the spectra of the ODT SAM on gold and has been used to calculate $\Phi_{\chi_{sam}^{(2)},NR}$. It is assumed, that $\Phi_{F_{sam}}$ is unaffected by the presence of the SAM and hence the fitted values can be taken for the bare substrate as well.

measurements. To understand its origin it is helpful to look at the phase of the non-resonant second order susceptibility $\Phi_{\chi_{sam}^{(2)},NR}$ which for the bare surfaces is determined under the assumption that the effective nonlinear Fresnel factor's phase does not change upon ODT adsorption and therefore can be taken from the fitted ODT spectra. Under this assumption $\Phi_{\chi_{sam}^{(2)},NR}$ for both substrates measured under PPP polarization combination implies contribution to the non-resonant substrate response from both inter- and intra-band transitions,while the response under SSP is dominated solely by inter-band transitions. As was pointed out in the theory chapter 2.1.5, which describes the non-resonant contributions to $\chi_{sam}^{(2)}$, the normal surface component of the susceptibility for the intra-band transitions χ_a contributes almost exclusively to the tensor component $\chi_{zzz}^{(2)}$ which is probed under PPP. It is easy to imagine that this normal surface component is most influenced by the presence of the ODT SAM. In fact as can be seen in table 7.2 the presence of the ODT SAM attenuates this component of the intra-band transitions and $\Phi_{\chi_{sam}^{(2)},NR}$ becomes 92.1°, respectively 84.0°. In case of SSP $\Phi_{\chi_{sam}^{(2)},NR}$ stays basically the same and in the case of the ODT SAM present equals in value $\Phi_{\chi_{sam}^{(2)},NR}$ obtained under PPP, although the sign has changed.

7.2 Potential-Dependence of Non-Resonant Substrate Response

7.2.1 Static Potential-Dependence

According to the fitted potential-dependent homodyned SFG spectra of an SP-LA SAM presented in table 6.4 in chapter 6.3 the phase and magnitude of the non-resonant second order susceptibility is influenced by an applied bias. To check whether this potential-dependence is real or a mere fitting artifact, phase-resolved SFG spectra are taken of a bare gold electrode to investigate the effect of an applied potential on the complex non-resonant second order susceptibility $\chi_{NR}^{(2)}$. These phase-resolved spectra in addition might reveal which of the contributions to $\chi_{NR}^{(2)}$, inter-band or intra-band transitions, show a bias dependence.

Just as for the potential-dependent homodyned SFG measurements we used the three electrode scheme, with the working, (pseudo-)reference and counter electrode all being gold (see also figure 4.1 in chapter 4.1). Sodium perchlorate diluted in deuterium oxide ($c_{NaClO_4} = 100\,mM$), a) pure and b) with added sodium iodide ($c_{NaI} = 1\,mM$), acted as the electrolyte. Simultaneous referencing is performed using the (pseudo-)reference electrode which exhibits a constant potential throughout the measurements and should therefore not change its spectral phase over the course of the measurement. Under the assumption the used electrolyte has no influence on the reference phase (or that the change influences both the reference and sample position in the same manner and will therefore be canceled upon evaluation) the previously determined absolute spectral phase $\Phi_{S_{Au},abs}$ of ozonized bare gold (91.4°, see section 7.1.2) is taken to determine the absolute phase of the sample signal.

Figure 7.4 shows the referenced spectrum for the case of the pure sodium perchlorate solution in a potential range in which no electrochemical reaction takes place (such as oxidation of the gold surface by residual oxygen that we could not get rid of entirely even by flushing the setup with nitrogen). After each potential a CV (see figure A14 in the appendix as an example) and one measurement at $0\,mV$ (against the pseudo-reference electrode) was taken
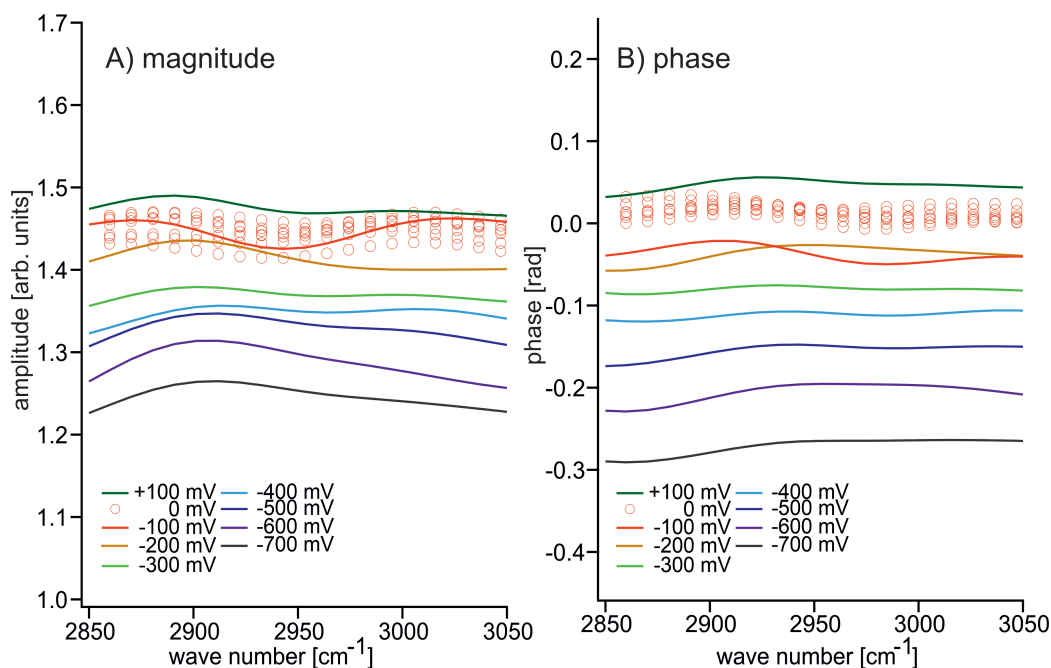
122

Figure 7.4: Phase-resolved non-resonant SFG response of bare gold as a function of applied potential. A) Magnitude. B) Phase. At every potential two spectra are taken and averaged.

to ensure the reversibility of any occurring changes. The averaged measurements at $0\,mV$ were used as the transfer function f_T. As can be seen both the magnitude and phase show a clear potential-dependence. The phase difference between the spectrum taken at $+100\,mV$ and -700 mV equals $0.32\,rad$ or $\approx 18°$. Over the same interval the magnitude decreases by $\approx 15\%$.

To monitor the potential-dependence more easily one point in the spectrum at $\approx 2950\,cm^{-1}$ is taken and its magnitude and phase are plotted as a function of applied potential in figure 7.5A. Both magnitude and phase show an almost linear behavior. In contrast the potential-dependent behavior changes entirely if iodide anions, which in contrast to perchlorate are able to specifically adsorb at the electrode,[163] are present in the solution as shown in figure 7.5B. Note, that for this measurement we had to shift the potential range by $100\,mV$ to more negative values since the oxidation of our gold working electrode through residual oxygen started at less positive potentials. It is, however,
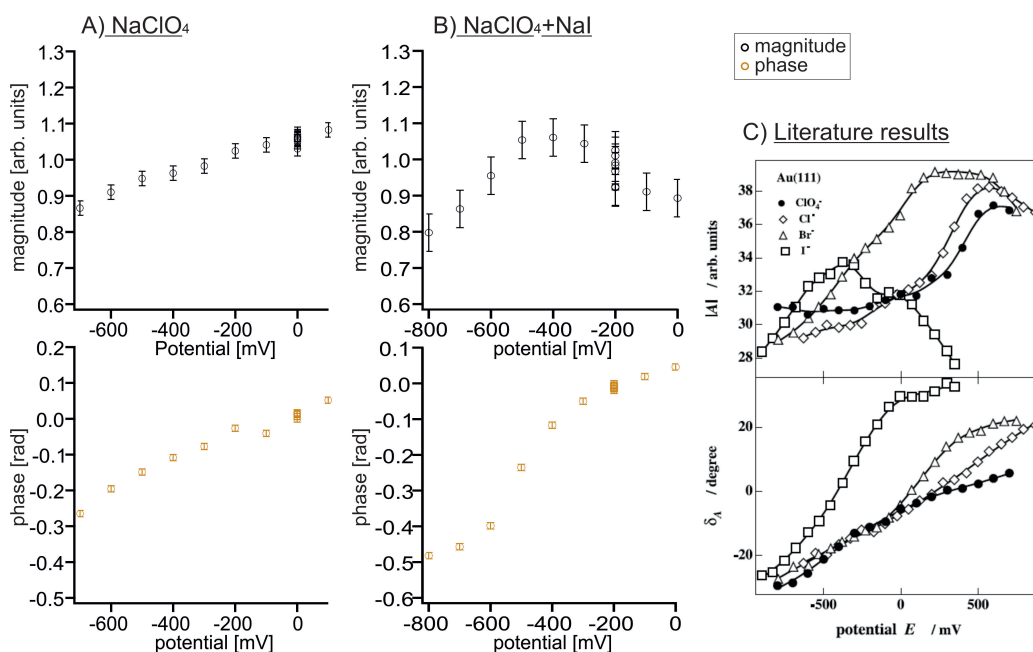
Figure 7.5: Potential-dependent phase-resolved non-resonant SFG response of gold. Electrolyte: A) $NaClO_4 + D_2O$, B) $NaClO_4 + NaI + D_2O$. Measured vs gold pseudo-reference electrode. C) Comparative measurement taken from[149]. Potential given vs SCE.

probable that this apparent shift reflects the uncertainty of measuring our potential against a pseudo-reference electrode.

The potential induced phase change in the presence of iodide ions is much stronger with $0.53\,rad$ or $\approx 30°$ and seems to reach a plateau at positive and negative potentials respectively. At the potential around the steepest phase change between $-400\,mV$ and $-500\,mV$ the magnitude reaches a maximum. This roughly coincides with the iodide adsorption peak in the CV (see figure A15 in the appendix) at $\approx -500\,mV$ against our pseudo-reference electrode.

It is worth noting that our results mirror previous phase-resolved SHG measurements by Pettinger et. al.[68,149,164], were the potential-dependent anisotropic SHG response of a single crystal Au[111] surface was investigated. The isotropic part A of these measurements corresponds to the $\chi^{(2)}_{zzz}$ component which dominates our SFG spectrum. Its potential-dependence is shown in figure 7.5C (taken from[149]). In the presence of iodide the maximum of the

isotropic part's magnitude $|A|$ also coincides with the iodide adsorption which took place at the single crystal gold[111] electrode at $\approx$-400 mV against a saturated calomel electrode(SCE).[165] In early studies Pettinger assigned this phase behavior to a covalent bond which is formed between the anion and the metal substrate upon specific adsorption.[53] The coincidental mixing of electronic states of the adsorbate and the metal and a partial charge transfer from the ion to the substrate then influence the energy levels of the inter-band transitions which are involved in the second order non linear process which in turn becomes more or less resonant. Since the adsorption strength increases for halides with growing atomic number and is weaker for perchlorate, which mostly adsorbs non-specifically due to its strongly bound solvation shell,[81] a smaller change in the phase angle can be expected for the latter one.

Later studies, however found that if plotted as a function of charge density rather than as a function of potential the change of the phase angle was widely independent of the nature of the anions over a large range.[149,165] This range includes a region in which the specifically adsorbed anions form disordered adlayers that are mobile and hence do not form covalent bonds. Consequently the anions rather influence the field at the interface than changing the electronic structure of the metal.

Only if the charge density surpasses a critical value (found to be $\approx$60 $\mu C/cm^2$) the mobile adlayers become ordered and immobile at which point the nature of the anion again determines the phase behavior.[149,163] Since Pettinger et all. however did not observe an additional change of the electrosorption valency at that point they concluded that no extra charge is transferred during the formation of new electronic states by the ordered adlayer.[165] The overall phase change therefore is explained by the change of charge density which effects intra-band transitions.

Rather than looking at the magnitude and phase, however, it is more convenient to convert the spectra into their respective real and imaginary part to understand the origin of this potential-dependence. To get a meaningful result it is crucial to use the correct phase of the gold sample's second order non-resonant susceptibility $\Phi_{\chi^{(2)}_{NR}}$ which can be derived using the measured normalized spectral phase $\Phi_{S_{norm},NR}$ and equation 7.11:

125

$$\Phi_{\chi_{NR}^{(2)}} = \Phi_{S_{norm},NR} + 91.4° - \Phi_{F_{Au}} \qquad (7.16)$$

where $\Phi_{F_{Au}}$ is the shift introduced by the Fresnel factors that needs to be taken into account at the gold sample(see also section 7.1.1). This shift so far is unknown and for a while we shall ignore it. The real and imaginary part for the spectrum which is corrected for the reference phase (91.4°) can be seen in figure 7.6A. Apparently both the imaginary and real part of the spectrum are potential-dependent. This would indicate that according to the theory on the contributions to the non-resonant second order susceptibility given in chapter 2.1.5 intra- as well as inter-band transitions would influence the SFG response's potential-dependence. For the SHG response Pettinger et all. found a similar potential-dependence of the real and imaginary part of their spectrum.[149,164] However, since they previously excluded inter-band-transitions they concluded that while the phase change depends on the charge density, "both the A_r [real] and A_i[imaginary] terms contain a complicated dependence on potential, charge density, surface coverage, etc."[164]

Pettinger et all., however, did not correct for the phase shift introduced by the nonlinear Fresnel factor $\Phi_{F_{Au}}$, which we so far have ignored as well. So the question arises, whether it is possible to find a phase shift such that only the real part, that represents the intra-band transitions which are charge density dependent, becomes potential-dependent. For a phase shift of $\Phi_{F_{Au}} \approx -30°$ this case occurs as can be seen in figure 7.6B.

So if the assumption is true that only either intra- or inter-band transitions but not both show a potential-dependence, potential-dependent measurements can help to determine $\Phi_{F_{Au}}$. This, however, assumes that $\Phi_{F_{Au}}$ itself is not potential-dependent. There is no possible way to verify this assumption. Looking at the potential behavior of the linear Fresnel coefficients might give some indication. Therefore we looked at the reflected intensity of the local oscillator from our sample spot, normalized by the intensity from the reference spot. As can be seen in figure 7.7 the reflectivity is constant within the range of uncertainty and consequently the linear Fresnel-factors are not potential-dependent
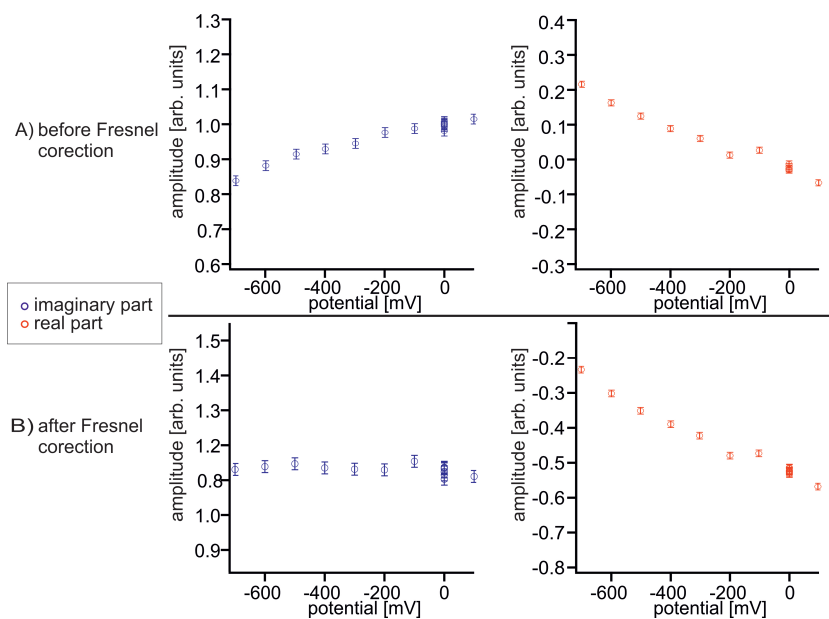
Figure 7.6: Potential-dependent phase-resolved non-resonant SFG response of gold. Electrolyte: NaClO$_4$+D$_2$O. Spectrum at $\omega_{IR} \approx 2950\, cm^{-1}$ after Shifting the Phase by 91.4° to account for the reference phase; Real and imaginary part A) before and B)after correcting for the supposed Fresnel phase of -30° so that only the real part shows a potential-dependence.
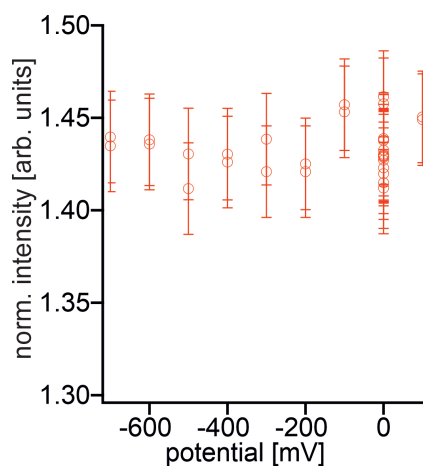

Figure 7.7: Intensity of the reflected local oscillator (LO) as a function of applied potential.
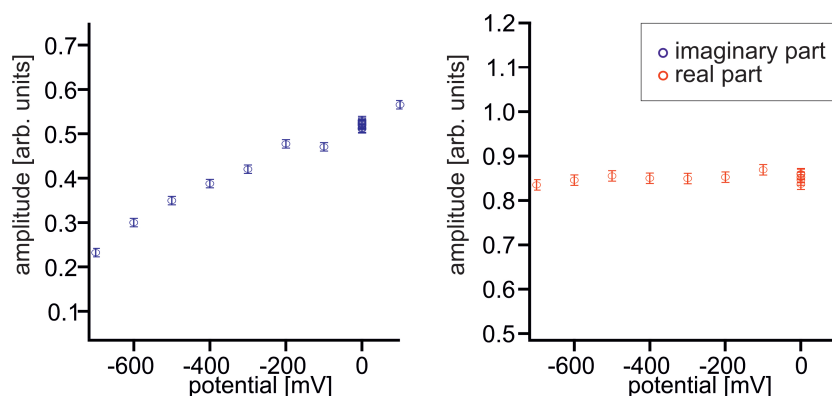
Figure 7.8: Real and imaginary part of the phase-resolved non-resonant SFG response of gold (Electrolyte: $NaClO_4$ + D_2O) after correcting for the more likely Fresnel shift of +60°.

within the investigated range.

The obtained phase shift of $\Phi_{F_{Au}} \approx$ -30°, however, is distinctly different from the calculated $\Phi_{F_{Au}}$ within our experimental geometry. $\Phi_{F_{Au}}$ should equal $\approx$+55° (see table A1 in the appendix). The difference between calculated and experimentally obtained value equals almost 90°. Consequently if a $\Phi_{F_{Au}}$ of $\approx$+60° is used in the Fresnel phase correction the potential-dependence of $\Phi_{\chi_{NR}^{(2)}}$ would entirely stem from the imaginary part (see figure 7.8) and hence according to the theory presented in chapter 2.1.5 from the inter-band transitions, which is in sharp contrast to the interpretations of Pettinger et all. This theory, however, does not take into account phase propagation effects due to the reflected SFG signal not solely originating from the upmost atomic layer, but depending on the material also from several tenth of nanometers from within the bulk.[166] In the case of e.g. dielectrics phase propagation effects lead to the bulk contribution to $\chi_{NR}^{(2)}$ being shifted in phase by 90° with respect to the surface contribution.[140] The bulk term of the intra-band transitions consequently should show up in the imaginary part after Fresnel correction. The results therefore might indicate, that the potential-dependence is dominated by the bulk term of the intra-band transition. A second possibility is the contribution of higher order terms, e.g. quadrupole terms to the measured response, which so far have been ignored but might lead to a phase shift as well. Of course there
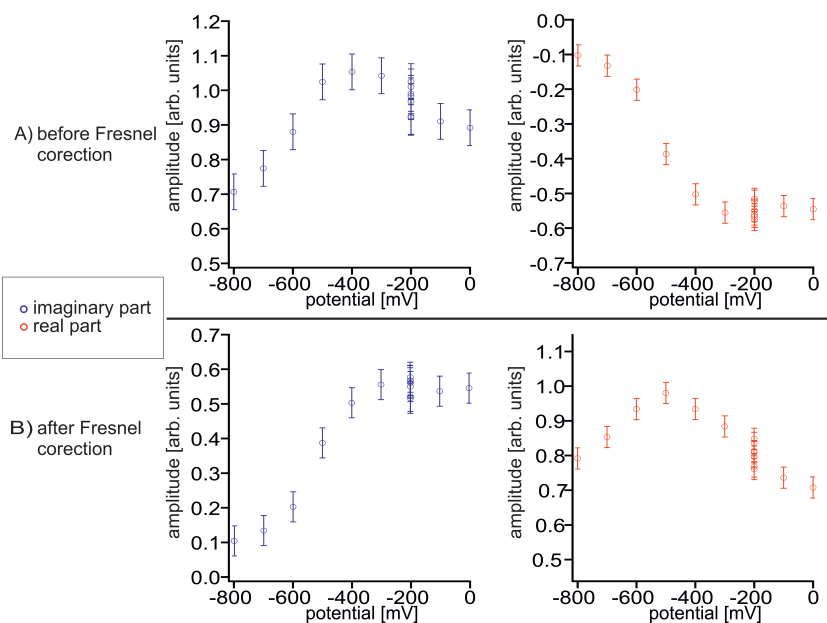
Figure 7.9: Potential-dependent phase-resolved non-resonant SFG response of gold. Electrolyte: $NaClO_4+NaI+D_2O$. Spectrum at $\omega_{IR} \approx 2950\, cm^{-1}$ after Shifting the Phase by 91.4° to account for the reference phase; Real and imaginary part A) before and B)after correcting for the Fresnel phase of +55°.

is also the chance, that the assumed assignment of intra-band transitions entirely to the real part and the inter-band transition entirely to the imaginary part of $\chi_{NR}^{(2)}$ is invalid. Either way, if the requirement holds, that only either the imaginary or the real part of the non-resonant SFG response of gold shows a potential-dependence, then it is possible to identify the overall phase shift due to the local field factors $\Phi_{F_{Au}}$.

In contrast to the measurements for the pure sodium perchlorate as soon as iodite anions are present it is not possible to find a $\Phi_{F_{Au}}$ such that only either the real or imaginary part of the spectrum becomes potential-dependent. If a phase shift of 55° is applied (which is close to the 60° in the case of pure sodium perchlorate), however, the change in the imaginary part is maximized. The spectrum's potential-dependence without and with Fresnel correction can be seen in figure 7.9A and B respectively. Based on the appearance of a potential-dependence for the real and imaginary part according to the theory presented

in chapter 2.1.5 it is likely that both intra- and inter-band transitions are influenced by an applied potential if additional specific adsorption takes place. Interestingly at around -200 mV the imaginary part seems to reach a maximum value, after which for more positive potentials the charge density seems to have no further influence. It would be interesting to see whether such a minimum could also be observed for the pure sodium perchlorate case but at higher potentials, since the presence of iodite anions faster increases the charge density. If the imaginary part reaches a constant minimum at values more negative than -600 mV or whether this apparent minimum is only an artifact due to a possible flawed Fresnel correction is difficult to say, especially since the iodite anions in this potential region are already desorbed from the electrode. It remains questionable why in that case the electrode should behave differently than in the case of pure sodium perchlorate.

The real part shows an increase in the region of the beginning adsorption of iodite and reaches a maximum in the potential range where the iodite peak in the CV also reaches it's maximum(see figure A15 in the appendix). Again it would be interesting to see the real part's behavior for more negative potentials which should not differ from the case of pure sodium perchlorate, where a constant behavior is expected. Unfortunately at more negative potentials we saw the onset of an electrochemical reaction, possibly deuterium reduction, which would interfere with such measurements. An additional open question is whether it is appropriate to assume only one distinct Fresnel phase shift over the whole potential range. It might be possible, that the adsorption of iodite changes $\Phi_{F_{Au}}$ and that the Fresnel correction should actually be conducted with different $\Phi_{F_{Au}}$ for every respective potential range.

7.2.2 Influence of the Velocity of Potential Cycling on the Potential-Dependence

As was pointed out in the previous section the non-resonant response is influenced by the charge density which in turn is modified by the presence/absence of ions in the electrochemical double layer. Upon altering the potential these ions, however, need some time to adapt to this change and to diffuse towards or away from the electrode. The velocity upon which the potential is varied, e.g. in a cyclic voltammogram, should therefore have an influence on the actual non-resonant response observed at a certain potential.

We monitored the non-resonant behavior of our gold electrode in the presence of sodium perchlorate (c=50 mM in Acetonitrile) during CV's of different scanning speeds v_{scan} to test this assumption. Acetonitrile as a solvent was used to increase the possible CV scanning range which ultimately was taken from -800 mV to +500 mV. Since recording a full interferogram takes a certain amount of time within our setup it is not generally possible to monitor kinetics. In this particular case, however, we use the fact that the adsorption, desorption and diffusion process is arbitrarily often reproducible (provided the gold electrode does not degrade). Therefore at every step in the interferogram we can take at least one full cycle of the CV before we move to the next position of the delay stage. That way we end up with a data matrix as shown in figure 7.10A. The horizontal slice in figure 7.10B taken around the interferograms maximum shows the intensity variation of the non-resonant response at this delay stage position as a function of applied potential during the CV. Compared to the static measurements discussed in the previous chapter this variation can be understood considering, that the applied potential induces a decrease in magnitude for more negative values as well as a phase shift with respect to the local oscillator. The latter causes the position of the interferograms maximum to slightly shift as well. Since the delay stage position is fixed in this slice the intensity is modulated around this maximum.

After the CV's at every delay stage position are taken one obtains full interferograms along the vertical axis as shown exemplarily in figure 7.10C that can be Fourier transformed into complex frequency spectra. In case more than one CV
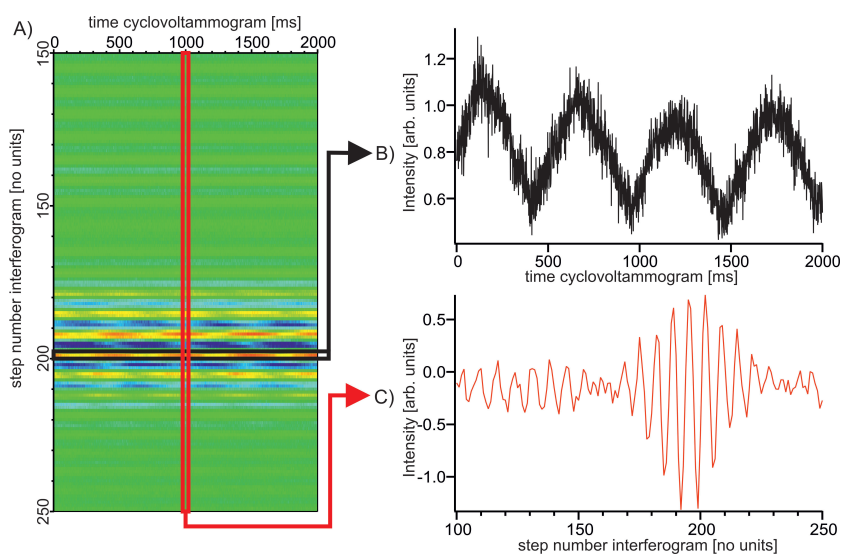
Figure 7.10: A) Data matrix. B) Intensity at distinct step in interferogram as a function of changing potential over time. C) Interferogram at distinct applied potential.

is taken, before Fourier transforming all spectra at a particular potential are averaged, additionally discriminating whether this potential was reached from a more positive or negative position (in other words at the descending, cathodic or ascending, anodic half cycle of the CV) to account for the hysteresis. A complete magnitude spectrum is shown in figure A16 in the appendix and displays mostly the Gaussian shape expected for the non-resonant response emulating the energy distribution within our broad band IR beam. One pronounced dip is related to the absorption of IR light around $1330\,cm^{-1}$ typically observed in synthetic diamond windows.[167] For further evaluation we took the point at $\approx 1500\,cm^{-1}$ and plotted its magnitude and phase against the applied potential (see figure 7.11A and B respectively). For a better comparison of the spectra taken at different scanning speeds all were normalized to the complex spectrum at $\Phi=0\,V$ (anodic half cycle).

With accumulating negative charge (see figure 7.11C, determined each from one of the taken CV's at respective scanning speeds shown in figure A17 in the appendix) the magnitude's value decreases as well as the corresponding phase value which is in agreement with the static measurements in deuterium ox-
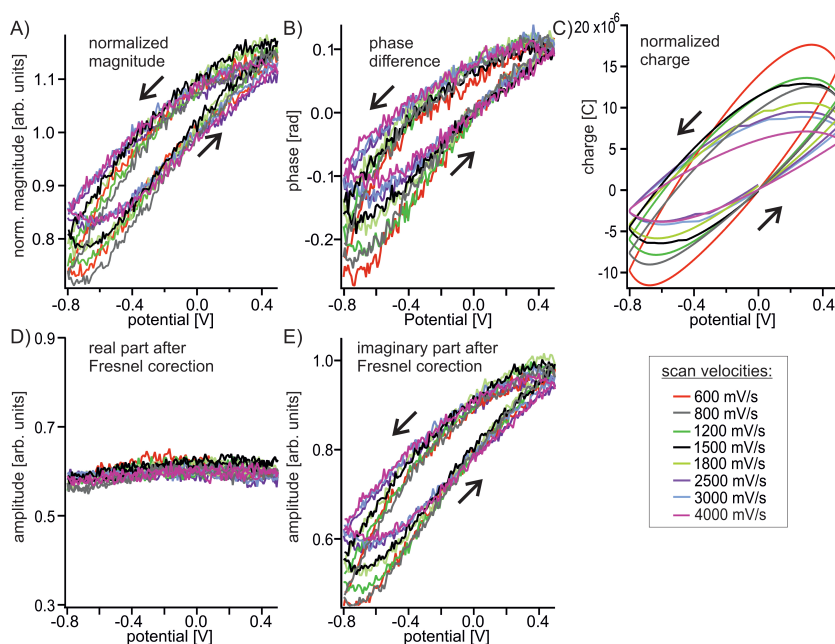
Figure 7.11: Non-resonant potential-dependent phase-resolved SFG response of gold in cyclic voltammograms (CV) of varying scanning speeds. A), B) Normalized magnitude and phase, respectively. C) Calculated accumulated charge during CV. D), E) real and imaginary part of the normalized spectrum after correcting for the Fresnel shift.

ide. The observed hysteresis for both the curves for the magnitude and phase somewhat reflect the case that the amount of charge flown towards or from the working electrode at a given potential-depends whether this potential was reached in the cathodic or anodic half-cycle as is obvious from figure 7.11C (e.g. the charge at the electrode initially at $\Phi=0\,V$ in the anodic half-cycle was reached in the cathodic half-cycle at $\approx$-510 mV to -680 mV depending on the scanning velocity).

As was pointed out in the previous chapter for the static case of the potential-dependent non-resonant measurements perchlorate anions do not adsorb specifically if solvated in an aqueous solution because of strong interactions with their solvation shell.[81] In acetonitrile conversely the anion is assumed not to be solvated.[168–170] Therefore perchlorate anions might diffuse into the inner Helmholtz-layer and adsorb specifically at the electrode, thereby either
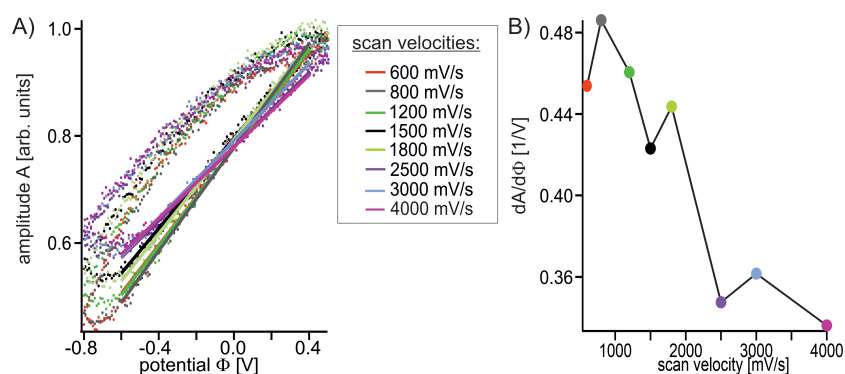
Figure 7.12: A)Fitted linear slope in the anodic branch of the CV. B) Slope as function of scanning speed.

forming covalent bonds by injecting electrons into the gold surface or at least influence the energy of surface states due to their presence.[46,80,81] Due to the absence of peaks in the CV and the corresponding calculated charge in figure 7.11C, however, it can be concluded that only non-faradaic currents are observed. Additionally we can conduct the Fresnel correction and find a value for the Fresnel shift of $+39°$ (calculated to be $\approx 52°$; see table A1 in the appendix) where in analogy to the static measurements of pure sodium perchlorate in deuterium oxide a potential-dependence of the real part is neglected in the absence of specific adsorption. The corresponding real and imaginary parts of our complex spectra at $\approx 1500\,cm^{-1}$ are presented in figure 7.11D and E.

According to figure 7.11 E the applied scanning speed v_{scan} seems to affect the slope of the amplitude of the imaginary part as a function of potential. Between $-600\,mV$ and $+400\,mV$ the imaginary part can be fitted as a linear function, which was done for the ascending, anodic half cycle to quantify this effect (see figure 7.12A). The determined linear slope as a function of v_{scan} is displayed in 7.12B. For v_{scan} smaller than $2500\,\frac{mV}{s}$ every change in v_{scan} in deed affects the amplitude of the imaginary part at a given potential. Above that value, however, the slope seems to converge to a constant minimum. To check in how far the flown charge towards or away from the electrode Q, that depends on v_{scan} (see figure 7.11 C), can explain this observation the amplitude of the imaginary part as a function of Q is plotted in figure 7.13A. The
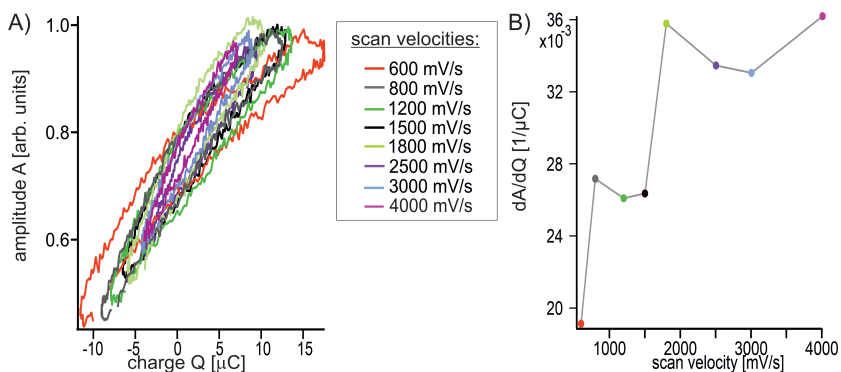
Figure 7.13: Same as figure 7.12, but imaginary amplitude plotted as function of flown charge.

corresponding fitted slopes as a function of scanning speed are shown in figure 7.13B. Up to $v_{scan} = 1800\,\frac{mV}{s}$ the change in amplitude per charge flown increases for increasing v_{scan}. This indicates that the screening of the electrode's charge density through, possibly, the electrolyte (counter-)ions becomes less effective since with an increase in v_{scan} these ions are less able to follow the alternating applied electric field due to their finite diffusion velocity. Above $v_{scan} = 1800\,\frac{mV}{s}$ every Coulomb of flown charge enhances/decreases the amplitude linearly. However, using values for the limiting molar conductivity Λ_m° of perchlorate and sodium ions in acetonitrile, $103.7\,\frac{S \cdot cm^2}{mol}$ and $77.0\,\frac{S \cdot cm^2}{mol}$ respectively (at $25°C$),[171] and the Nernst-Einstein equation to determine the diffusion coefficient D,[172]

$$\Lambda_m^\circ = \frac{F^2 z}{RT} D \qquad (7.17)$$

we can estimate the mean distance the ions travel during the time a certain potential is applied. Even for the highest v_{scan} this distance is in the range of micrometer and therefore much bigger than the electrochemical double layer. In other words even for the highest scanning speed the ions should have enough time to screen the charge density of the electrode in the same way and there should be no scanning speed dependence. So far, however, the behavior of the

solvent has not been taken into account. In the literature it has been reported, that at a positively polarized electrode the acetonitrile molecules are oriented with their nitrogen atom pointing towards the interface, possibly forming a chemical bond with the electrode via its free electron pair.[173,174] In contrast around the potential of zero charge the acetonitrile is oriented parallel with respect to the electrode.[173] The solvent's molecules reorientation upon the variation of potential could be much slower than the electrolyte's diffusion and account for most of the observed scanning speed dependence.

7.3   Heterodyned Spectra of SAM Buried by Solvents

The problematic spectral assignment and fitting ambiguities within the homodyned SFG spectra of an SP-LA SAM buried under acetonitrile are discussed in chapter 6. To tackle this issues a method has been developed within this thesis, that allows to measure phase-resolved spectra of buried interfaces (presented in section 3.4.2). The resulting spectra and their evaluation shall be discussed in the following, starting with the model SAM of ODT. Subsequently heterodyned SFG spectra of the SP-LA SAM will be fitted and compared to their homodyned analogs.

7.3.1   ODT Model Spectra

Heterodyned measurements of buried interfaces are possible using the time delay compensation scheme outlined in chapter 3.2 to account for the dispersion induced time delay between the local oscillator and the up conversion pulse. To check if this scheme is applied correctly a phase-resolved SFG spectrum of an ODT SAM on gold under acetonitrile is taken and compared to its spectrum in air (see section 7.1.4). Since a significant influence of the solvent on the spectral appearance of the ODT SAM's vibrations is not expected both spectra should basically appear the same. However, due to our spectrometer geometry we cannot apply simultaneous referencing. The distance between

the reference and sample spot is such, that in the case of a sample covered by a solvent and a window both points need to stem from the same substrate (see figure 7.14A). In that case restricting the self-assembly to the sample position is challenging. Different strategies have been tried as shown in figure 7.14A, but self-assembly at the reference spot has only been prevented, if no gold was present here but alpha-quartz. On quartz the ODT is unlikely to form thio-bonds and can be rinsed away after the self assembly process. This works well in terms of sample preparation. The SFG signal of solvent buried quartz in reflection, however, is to weak to be detected. So in the present setup geometry simultaneous referencing for samples containing SAM's buried under a solvent is not possible. In a future geometry this will be tackled by increasing the distance of the sample and reference position. Nonetheless the obtained spectra can be evaluated. Two adjustments, however, have to be made. First, to account for the chirp induced divergence from a constant value of $\Phi_{S_{norm}}$ (see also figure 7.1) an additional reference measurement has to be taken before or afterwards as shown in figure 7.14B and C. The phase chirp is constant over time (see figure 7.14C), the only problem is the determination of the absolute phase with this method.

In order to reduce inaccuracies in the resulting spectra originating from this subsequent referencing method instead of dividing the sample magnitude by the reference magnitude the fitting equations 7.9 and 7.10 for the real and imaginary part are amended to include the spectral envelope of the IR pulse. With ω_{center} the IR's center frequency and Γ_{IR} the pulses full width at half maximum the fit equation for the real part then becomes

$$
Re\{S_{norm}(\omega)\} = e^{\frac{(\omega-\omega_{center})^2}{\Gamma_{IR}^2}} [|\chi_{NR}^{(2)}|cos(\Phi_{S_{norm},NR})
$$
$$
+ cos(\Phi_{S_{norm},R}) \sum_{v}(\frac{A(\omega_v-\omega)}{(\omega_v-\omega)^2+\Gamma_v^2}) - sin(\Phi_{S_{norm},R}) \sum_{v}(\frac{A\Gamma_v}{(\omega_v-\omega)^2+\Gamma_v^2})]
$$

$$(7.18)$$

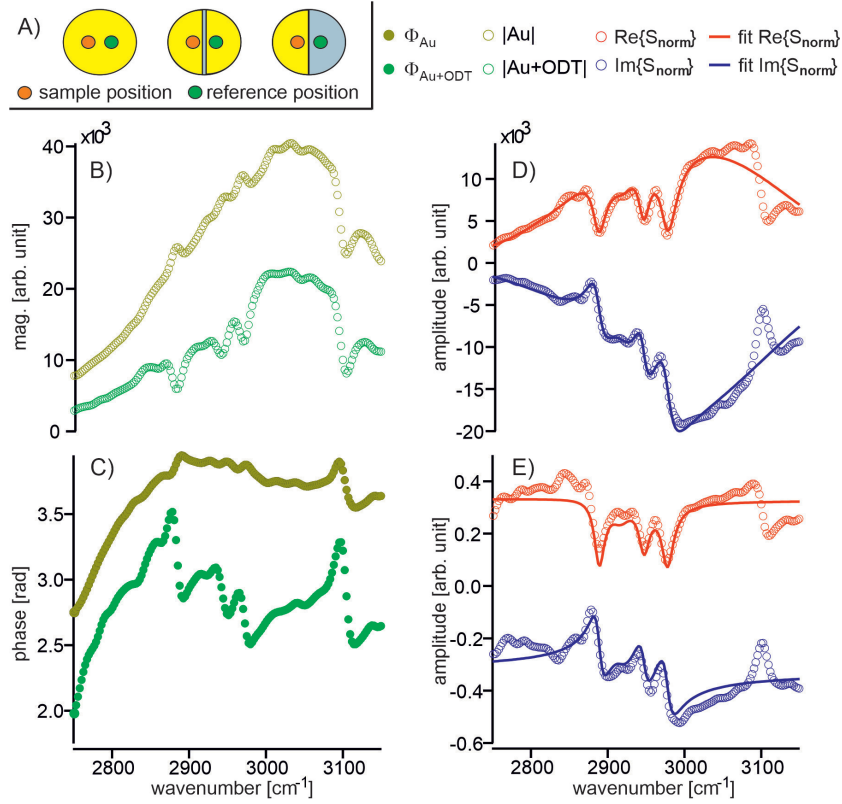and analogously the imaginary part is given as:

Figure 7.14: A) Tested substrate geometries. B) Magnitude and C) phase of solvent buried ODT SAM spectrum on gold (green) and subsequently taken reference measurement of a solvent buried bare gold substrate (gold). Real (red) and imaginary (blue) part of the complex spectrum undivided (D) and divided (E) by the reference magnitude.

$$Im\{S_{norm}(\omega)\} = e^{\frac{(\omega - \omega_{center})^2}{\Gamma_{IR}^2}} [|\chi_{NR}^{(2)}|sin(\Phi_{S_{norm},NR})$$
$$+ sin(\Phi_{S_{norm},R}) \sum_{\nu}(\frac{A(\omega_{\nu} - \omega)}{(\omega_{\nu} - \omega)^2 + \Gamma_{\nu}^2}) + cos(\Phi_{S_{norm},R}) \sum_{\nu}(\frac{A\Gamma_{\nu}}{(\omega_{\nu} - \omega)^2 + \Gamma_{\nu}^2})]$$

$$(7.19)$$

Figure 7.14D shows the so fitted spectrum (from here on called unreferenced spectrum). For comparison the same spectrum additionally divided by the magnitude of the reference measurement (and therefore in contrast to 7.14D

138

Assign.		unrefed.	refed.	Assign.		unrefed.	refed.
$\chi_{NR}^{(2)}$	$\|\chi_{NR}^{(2)}\|$	21080.86	0.46	$\chi_{NR}^{(2)}$	$\Phi_{S_{norm},NR}$	-42.3 °	-44.7 °
$\nu_s(CH_3)$	A	-205251.76	-1.94	$\nu_{as/F}(CH_2)$	A	-65857.62	-0.94
	ω_q	2885	2889		ω_q	2919	2916
	Γ_q	11.73	7.91		Γ_q	15.73	14.99
$\nu_F(CH_3)$	A	-79919.12	-1.46	$\nu_{as}(CH_3)$	A	-104142.20	-2.17
	ω_q	2945	2947		ω_q	2975	2977
	Γ_q	9.67	8.28		Γ_q	11.37	9.40
$\chi_R^{(2)}$	$\Phi_{S_{norm},R}$	-120.6°	-97.6°	Gauss	ω_{center}	3002.79	
					Γ_{IR}	172.26	

Table 7.3: Fitting values of solvent buried ODT SAM on gold spectrum shown in figure 7.14, either divided by reference spectrum or taken as is.

called referenced spectrum) is displayed in figure 7.14E. The fit parameters for both fits can be found in table 7.3. The peak visible at $\approx 3100\,cm^{-1}$ in both the SAM and the reference spectrum which can be attributed to the solvent was not included in either fit.

Both the referenced and unreferenced spectrum are more noisy than the ODT SAM spectra taken in air (shown in chapter 7.1.4 in figure 7.3). Therefore the determination of the center frequencies for resonances of the methyl group by fitting is more ambiguous. Consequently their fitted values are markedly shifted with respect to the literature values by 10-15 cm^{-1}.[141] In neither spectrum the fit could resolve the symmetric vibration of the methylene group indicating a gauche defect located at $\approx 2850\,cm^{-1}$ and thus located at the edge of our spectral region defined by the Gaussian shaped IR beam. In contrast the feature indicating its anti-symmetric stretch and a Fermi resonance at $\approx 2915\,cm^{-1}$ (much closer to the IR's center frequency) could be fitted.

The absolute values of $\Phi_{S_{norm},NR}$ and $\Phi_{S_{norm},R}$ (see section 7.1.5 equation 7.12, respectively 7.14) do not bear any scientific value, since the absolute spectral reference phase $\Phi_{S_{ref},abs}$ that was subtracted from the raw spectrum to correct for the chirp is unknown, as was pointed out earlier. However, taking their difference $\Phi_{S_{ref},abs}$ cancels and the phase of the non-resonant substrate response $\Phi_{\chi_{sam}^{(2)},NR}$ is calculated to be 78.3° and 52.9° for the unreferenced and referenced

spectrum respectively. The latter value is far off the expected $\approx 90°$ that was observed in the measurements against air (see table 7.2 in section 7.1.6). Additionally the obtained center frequencies in the case of the referenced spectrum are further away from literature values as in the unreferenced case. To avoid spectral distortion from imperfect referencing in future measurements, where no simultaneous referencing is applicable, we therefore only correct the raw spectrum for the phase chirp and otherwise fit it as an unreferenced spectrum according to equation 7.18 and 7.19. This approach will also be applied in the next section for the evaluation of the heterodyned SFG spectra of the SP-LA SAM on gold, buried under acetonitrile.

7.3.2   Heterodyned SP-LA Spectra: NO_2-range

As could be shown so far both the presence of actual covalent bonds as well as an applied potential bias can influence the phase of the non linear second order response of the gold substrate. Since switching the SP-LA with the help of UV light from the closed Spiropyran (SP) to the open Merocyanine (MC) form creates a large electric dipole moment within the molecule an influence on the non-resonant phase by this dipole is conceivable. The magnitude of this influence, however depends on the interspace between molecule and substrate since the latter is attached via a linker chain and thus no actual phase change might be observable. This has already been discussed in chapter 6.1.5 when fitting the SP-LA data required the decision to allow or prevent the parameter $\Phi_{\chi_{sam}^{(2)},NR}$ to be different for the respective SP and MC-form's spectrum. Finally both was tested and based on the physical probability of the resulting fits it was concluded that a change of $\Phi_{\chi_{sam}^{(2)},NR}$ during the course of switching was likely. In the following phase-resolved measurements of the two SP-LA forms shall be used to back or revise this conclusion.

The complex spectral magnitude for the SP-form in Air and Acetonitrile, as well as the MC-form in Acetonitrile are shown in figure 7.15A. Qualitatively they resemble the homodyned intensity spectra. Especially the behavior of the symmetric stretch vibration of the Nitro group at $\approx 1340 cm^{-1}$ which changes the direction of its transition dipole moment upon addition of acetonitrile and
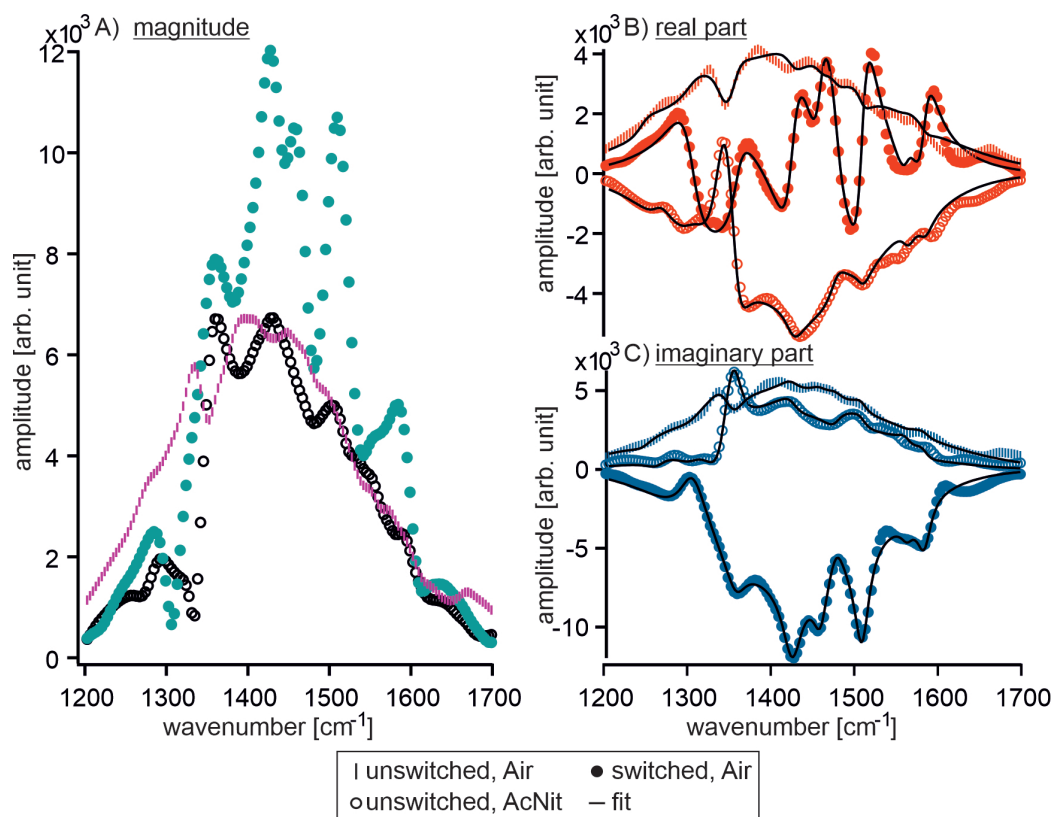
Figure 7.15: A) Magnitudes of unreferenced phase-resolved SP-LA spectra in air and switched and unswitched in acetonitrile. B) and C) respective real and imaginary parts.

consequently appears as a peak in the spectrum against air and afterwards as a dip is reproduced. Also its disappearance upon switching as well as the appearance of new prominent features at $\approx 1310\,cm^{-1}$, $\approx 1510\,cm^{-1}$ and $\approx 1590\,cm^{-1}$ representing the MC-form are observed. We can therefore conclude that the samples in both the homodyned and heterodyned measurements are comparable and any differences in the obtained fit parameters stem from the uncertainties associated with the respective fitting method.

The fitting was conducted using the spectral real and imaginary part shown in figure 7.15B and C respectively simultaneously to globally fit all spectra together. As was the case for the ODT SAM buried by solvents simultaneous referencing was not possible due to the lack of a SAM free reference spot on

Assignment		Air SP-form	AcNit. SP-form	AcNit MC-form
$\chi_{NR}^{(2)}$	$|\chi_{NR}^{(2)}|$	$(5.99\pm0.06)\cdot10^3$	$(6.09\pm0.10)\cdot10^3$	$(7.68\pm0.10)\cdot10^3$
$\chi_{NR}^{(2)}$	$\Phi_{\chi_{NR}^{(2)}}$	13.89°±5.37°	90.58°±4.75°	114.74°±3.43°
		(52.12°-38.23°)	(149.45°-58.87°)	(-64.31°-(-179.05°))
$\nu(C-N)$	A	(-20.04±3.49)·10^3	(-23.55±8.67)·10^3	(0.98±5.21)·10^3
	ω_q	1247±4	1266±4	
	Γ_q	16.83*	14.05±5.48	
$\nu(C-N^+)$	A	(-12.29±3.07)·10^3	(-27.20±6.32)·10^3	(-123.07±9.40)·10^3
	ω_q	1305±1		
	Γ_q	19.56±1.45		
$\nu_{sym}(NO_2)$	A	(33.28±7.16)·10^3	(-136.44±29.21)·10^3	(15.37±6.38)·10^3
	ω_q	1343±2		
	Γ_q	17.84±1.64		
$\nu(CH_3)$	A	(-18.21±5.99)·10^3	(81.48±23.71)·10^3	(37.95±5.18)·10^3
	ω_q	1358±2		
	Γ_q	14.60±1.27		
$\nu(CO^-)$	A	(8.68±1.61)·10^3	(12.50±1.86)·10^3	(66.35±5.60)·10^3
	ω_q	1426±1		
	Γ_q	14.42±0.95		
$\nu(C-C_{arom})$	A	(3.68±1.27)·10^3	(0.31±1.75)·10^3	(36.64±7.28)·10^3
	ω_q	1460±1		
	Γ_q	10.85±1.41		
$\nu(C-C_{arom})$	A	(6.61±1.72)·10^3	(-12.83±2.99)·10^3	(-34.52±9.24)·10^3
	ω_q	1479±2		
	Γ_q	13.07±2.43		
$\nu_{asym}(NO_2)$	A	(8.60±1.41)·10^3	(9.26±1.96)·10^3	(93.17±4.56)·10^3
	ω_q	1510±1		
	Γ_q	10.86±0.46		
$\nu(C-C_{arom})$	A	(-1.82±1.77)·10^3	(13.42±4.37)·10^3	(24.58±8.40)·10^3
	ω_q	1564±2		
	Γ_q	9.36±2.22		
$\nu(C=N^+)$	A	(7.14±2.27)·10^3	(22.90±5.00)·10^3	(109.13±12.20)·10^3
	ω_q	1584±1		
	Γ_q	10.60±1.06		

Table 7.4: Fitting values of SP-LA spectra displayed in figure 7.15.

our gold substrate. The phase of a reference measurement taken beforehand had thus to be used to account for the interferometer induced phase chirp and the Gaussian shape of the IR beam had to be taken into consideration by fitting with equation 7.18 and 7.19 for the real and imaginary part respectively. As was pointed out with this method the absolute phase of the spectrum and thus information about the influence of the Fresnel factor's phase on the spectrum cannot be obtained, but the difference of the fitting parameters $\Phi_{S_{norm},NR}$ and $\Phi_{S_{norm},R}$ can be used to determine the substrate's phase $\Phi_{\chi^{(2)}_{sam},NR}$. The fitting parameters are shown in table 7.4. The resonances' assignments have been discussed in the chapter 6.1.3 while presenting the fitted homodyned spectra in table 6.1. Compared to the previous fitting parameters the center frequencies have only shifted little with the exception for the aromatic stretch at $1564\,cm^{-1}$ which was in the homodyned case resolved at $1524\,cm^{-1}$, back then pointed out as unreasonable since according to the literature a center frequency at around $1570\,cm^{-1}$[144] could be expected. Within our heterodyned fitting this value is more closely met. A second exception is the center frequency of the C-N-stretch for the SP-form in air at $1247\,cm^{-1}$. Unlike the frequencies for the other resonances this value could not be linked with the other spectral center frequency of the same resonance otherwise causing the parameter to walk out of the actual fitting range. This was, however, not an issue when only the two spectra taken in acetonitrile where fitted simultaneously.

The amplitude development for the Nitro-group stretches show the same behavior as in the homodyned case as the symmetric stretch at $1343\,cm^{-1}$ decrease to one ninth of the initial magnitude and the asymmetric stretch at $1510\,cm^{-1}$ increases tenfold. This behavior shows as was discussed before that the benzopyran unit of the head group is rotated by $\approx 90°$ around an axis orthogonal to the surface normal during the transformation from the SP to the MC-form (see figure 6.1 in chapter 6.1.1). In contrast to the homodyned case the remaining amplitude of $\nu_{sym}(NO_2)$ in the MC-form has switched its sign which would indicate that its transition dipole moment has changed direction once more indicating a further lowering of the head group. However, in the homodyned case the sign of the amplitude for the oxygen in para-position to the nitro group was opposite to the one of $\nu_{sym}(NO_2)$ and if this additional

143

lowering is true, it's amplitude should be negative. This is not the case. Therefore it is more likely that the sign change of the amplitude of $\nu_{sym}(NO_2)$ is the result of the interference between the adjacent $\nu_{sym}(NO_2)$ and $\nu(CH_3)$ which lead to fitting ambiguities. Anyway, compared to the other amplitudes in the MC-form the one of $\nu_{sym}(NO_2)$ is quite small.

The vibrations involving the nitrogen atom at the linker chain show a physically more consistent picture than in the homodyned case. Not only increases the dip at $1305\,cm^{-1}$ representing $\nu(C-N^+)$ (also observed in the homodyned fit) but additionally the by eye observable rise of the peak at $1584\,cm^{-1}$ representing $\nu(C=N^+)$ is now resolved in an increased amplitude. In the homodyned fit this amplitude seemed constant in the case of the SP and MC-form due to the inability to disentangle the changes in the resonance amplitude from changes in the contribution of the non-resonant background. Also the amplitude for the vibration of the neutral $\nu(C-N)$ group now decreases as expected.

The aromatic stretches' amplitudes display a similar behavior in the heterodyned fit as in the homodyned one with a strong increase for the resonance at $1460,cm^{-1}$ and smaller ones for the resonances at $1479,cm^{-1}$ and $1564,cm^{-1}$. The absence of the resonance at $1460,cm^{-1}$ in the SP-form points to its origin in the benzopyran unit which is most affected by the transition to the MC-form. Finally the increase of the amplitude for the $\nu(CO^-)$-stretch is also comparable to the homodyned case so in total the heterodyned fit confirms most of the values extracted from the homodyned fit. The only question left is whether it is justified to assume different phases for the non-resonant gold substrate response as we did previously. As was laid out before this phase can be unambiguously determined using the non-resonant off set in the real and imaginary part of our complex spectra obtained in our heterodyned measurement. In deed a phase shift of $\approx 24°$ could be observed while switching from the closed SP to the open MC-form which approximately equals the outcome of our homodyned fit reassuring the correctness of the latter one and affirming an influence of the head group's dipole moment on the substrate's non-resonant phase. Hence $\Phi_{\chi^{(2)}_{NR}}$ can be used to monitor the local potential and the polarity of adjacent molecules and ions.

7.3.3   Ambiguities in the Fitted 'SP-LA in Air' spectrum

The non-resonant phase of the gold substrate in the spectrum of the SP-form measured in air was determined through global fitting to be 13.89° (see table 7.4). This is suspiciously far off the ≈90° the non-resonant gold phase should ideally take when thiols are attached (and which it did in the case of the buried SP-form). Possible fitting ambiguities that might be responsible for this apparent divergence can originate from the fact that all resonant features except the peak for $\nu_{sym}(NO_2)$ were obscured by the in comparison large non-resonant background. However, since in the measurement against air we are able to simultaneously take a reference spectrum which we can use to normalize the background we can additionally use the so obtained normalized spectrum to fit its real and imaginary part (shown in figure 7.16) according to equation 7.9 and 7.10 respectively (see section 7.1.4).

The fit with 10 assumed resonances was not successful as can be seen in table A4 in the appendix since some features were too close to the noise level so that the resonance frequencies walked off during the fit and the respective full widths at half maximum became unreasonably large. This fact also explains their large fitting error. Better results were achieved assuming only 9 resonances (table A5 in the appendix). The non-resonant substrate's phase, however, was in both cases closer to 90°, with ≈57° and ≈52° respectively but still remarkably shifted. What ultimately caused that shift remains still unknown. The fitting difficulties show, however, that even though fitting heterodyned spectra give more accurate results than fitting homodyned ones the system is still under-determined and additional information are needed to get physically reasonable results. Some additional information are actually directly accessible by looking at the difference frequency (DFG) response which is created simultaneously to the SFG one. Especially within our collinear setup the two responses copropagate and could be easily separated in future measurements using a beam splitter and photodiodes sensitive in the respective frequency range.
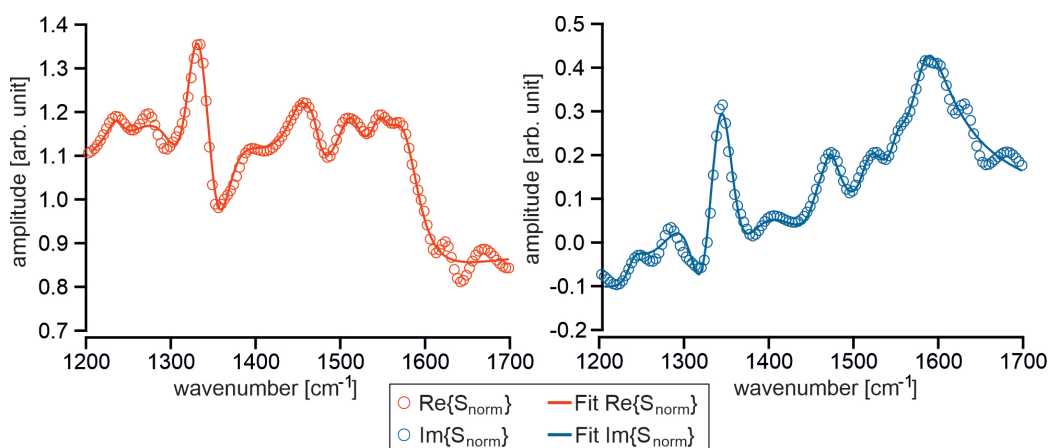
Figure 7.16: (Fitted) Real and imaginary part of the referenced spectrum of unswitched SP-LA SAM at gold in air.

7.3.4 Heterodyned SP-LA spectra: CH_3-range

Contrary to the homodyned case it was possible to additionally record spectra of the SP-LA SAM in the methyl range due to the enhanced sensitivity introduced by the balanced detection scheme into the heterodyned SFG Set Up. According to the literature[144] the SP-LA head group's main features can be expected at $2863\,cm^{-1}$ and $2969\,cm^{-1}$ representing the symmetric and anti-symmetric stretching vibration respectively of the methyl groups located at position 3 in the indoline unit of the molecule. However, based on the non referenced magnitude spectrum (figure A18 shown in the appendix) of SP-LA measured in air three additional resonances were assumed for fitting. The imaginary and real part of the complex normalized SP-LA spectrum and the respective fits are shown in figure 7.17A.

The symmetric stretch could be resolved in accordance with the literature at $\approx 2860\,cm^{-1}$ (see table 7.5), the presumed anti-symmetric one, however, is located at $2954\,cm^{-1}$ and would be quite shifted. Additionally according to the fit the sign of its amplitude is different than the one of the symmetric stretch's amplitude. For the case of the $\chi^{(2)}_{zzz}$-tensor component, which should dominate these SFG spectra, a terminal methyl group's symmetric and anti-symmetric stretches' amplitudes exhibit the same sign. This fact is also reproduced in the
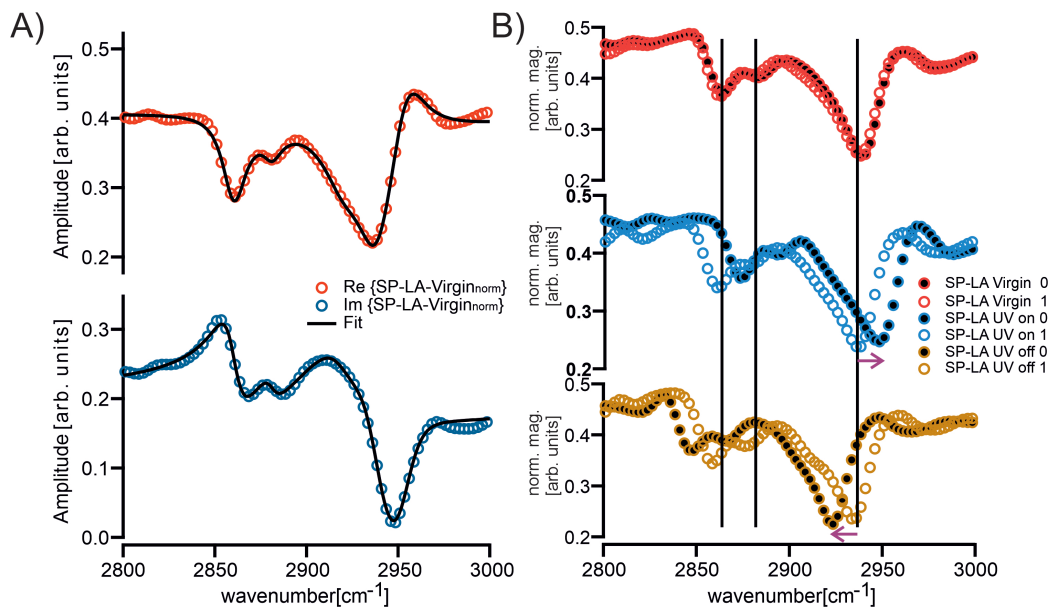
Figure 7.17: A) Normalized phase-resolved SFG spectrum of an SP-LA SAM in the methyl region. B) Apparent shift of the spectral center frequencies due to the UV-lamp's introduction of heat into the interferometer.

SFG spectra of the (buried) ODT SAM discussed previously and there is no obvious reason why in the case of SP-LA this should be different. The origin of the resonance at $2954\,cm^{-1}$ therefore is not clear.

The additional resonances at $2881\,cm^{-1}$, $2919\,cm^{-1}$ and $2938\,cm^{-1}$ very likely originate in the linker chain since aromatic resonances from within the head group would be expected above $3000\,cm^{-1}$ [145] (and are in fact observed as

	Value		Value		Value
A	-0.94±0.04	A	-0.24±0.04	A	-1.16±0.47
ω_q	2860±1	ω_q	2881±1	ω_q	2919±3
Γ_q	7.85±0.34	Γ_q	6.61±1.06	Γ_q	25.34±2.16
A	-2.49±0.91	A	1.63±0.46	$|\chi_{NR}^{(2)}|$	0.45±0.01
ω_q	2938±1	ω_q	2954±2	$\Phi_{\chi_{NR}^{(2)}}$	126.65°±1.40°
Γ_q	13.66±2.52	Γ_q	12.55±1.15		(26.17° -(-100.48°))

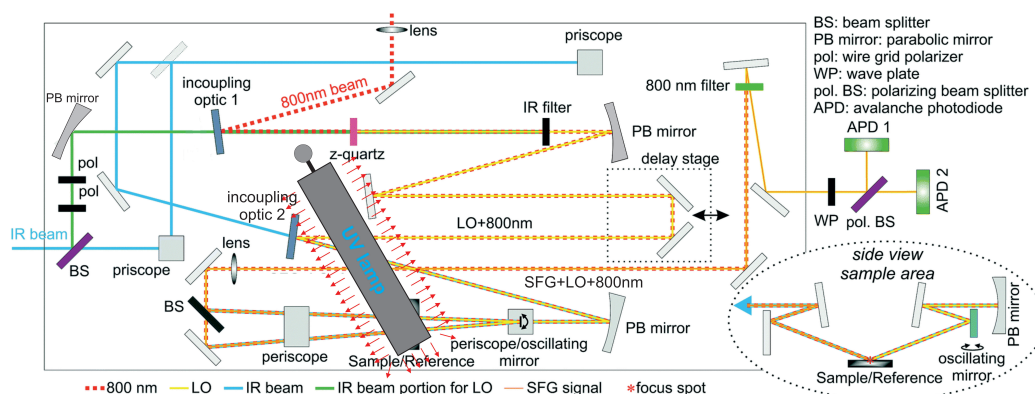Table 7.5: Fitting Parameter SP-LA in Air; Methyl-Range.

Figure 7.18: Heat introduction into the HDSFG setup through running UV lamp.

weak features in the magnitude spectrum in figure A18). If this is true these resonances would allow us to monitor the behavior of the linker chain during switching between the SP and MC-form, e.g. an increase or decrease of the tilt angle (provided the resonances do not all stem from the bridging methylene group in the anchor group of the linker which should not be affected by switching).

In the kinetic homodyned SFG data (see chapter 6.2) two processes on distinct time scales were observed. While the first process, that associated with the ring opening and subsequent reorientation of the head group, happens to be to fast to be monitored with our current heterodyned SFG setup the second process with a half life time of more than 20 minutes (see table 6.3) is slow enough. This slow process was possibly linked among others to the reorientation of the linker chain. To examine this link it was planned to take a series of heterodyned SFG spectra of SP-LA while switching with UV light. However, the UV lamp was located above our sample but also next to the in-coupling mirror of the interferometer part in our setup (see figure 7.18). After switching the lamp "On" the emitted heat caused a change of the thermal equilibrium inside our setup over the cause of one interferogram cycle which caused an apparent frequency shift of the whole spectrum to higher wavenumbers (see figure 7.17B). After reaching the thermal equilibrium the spectrum again was

resolved at the expected frequency. Switching the UV lamp off accordingly caused the spectrum to shift to lower apparent frequencies. Therefore globally fitting the kinetic data would only be possible without fixing the resonance frequencies. The resulting amplitudes then were less comparable so we refrained from taking actual kinetic measurements. In a future planned setup this problem will be tackled by well separating the sample area and the interferometer part.

Chapter 8

Summary and Outlook

Phase-resolved SFG Spectra of Buried Interfaces

The main objective of this thesis was to characterize processes at the electrochemical interface with the means of phase-resolved vibrational sum frequency generation spectroscopy. Therefore a procedure was developed to extent phase-resolved second order nonlinear measurements to solid/liquid interfaces in general and the electrode/electrolyte interface in particular by achieving precise timing control between the generated nonlinear sample signal and the local oscillator (LO). Details of this procedure are presented in chapter 3.2. In this scheme the two linearly polarized orthogonal sample and LO pulses are directed through a birefringent crystal were they experience a polarization-dependent group velocity delay which for the pulse whose electric field lies in plane with the crystal's optical axis can be continuously tuned as a function of its incident angle, thus compensating (or introducing) a relative time delay between the pulses. Afterwards a polarization-based balanced detection scheme (chapter 3.1.3) is applied to bring the two pulses to interference. The utilization of a thin z-cut α-quartz for the generation of the LO pulse in transmission could be shown to permit the required orthogonal polarization with respect to the signal pulse regardless of the polarization of the pump pulses involved in the nonlinear process and thus allowing full flexibility in polarization dependent measurements.

The scheme was implemented into a collinear spectrometer design, presented in chapter 3, thus taking advantage of enhanced phase accuracy, the possibility of simultaneously taking a reference spectrum and a simplified alignment inherent in collinear phase-resolved SFG approaches but adding the benefit of precise timing control so far only possible in noncollinear geometries. While our spectrometer operates in the time domain this timing control method can easily be applied in phase-resolved frequency domain techniques as well. As a result it became possible to obtain phase-resolved SFG spectra of solvent-buried interfaces to study the behavior of self-assembled monolayers (SAM's) of octadecanethiol (a widely studied model system) and the spiropyran-derivative SP-LA at gold buried under acetonitrile, as well as the potential-dependent non-resonant second order nonlinear response of a bare gold electrode in the presence of nonspecific and specific adsorbing ions.

Molecular Switches at the Electrode/Electrolyte Interface

The behavior of a self-assembled monolayer(SAM) of the spiropyran-derivative SP-LA attached to a gold electrode has been investigated utilizing conventional homodyned SFG spectroscopy (see chapter 6) as well as the within the framework of this thesis developed phase-resolved approach (see chapter 7.3). Photo-switchable spiropyran-derivatives with the same 6-Nitro-BIPS headgroup as SP-LA had already been implemented into "On/Off"-switchable electrochemical sensors, although understanding of how the interfacial field affects the properties of the molecular switch has not been available so far. Due to the interface specificity of the nonlinear second order vibrational SFG spectroscopy it could already be shown within the homodyned spectra that even moderate interfacial fields have a pronounced effect on the SP-LA molecules' switching behavior. The open merocyanine (MC) form, that is achieved by irradiating the SP-LA SAM with UV light, is destabilized applying a positive potential bias which leads to the formation of the closed spiropyran (SP) form. A negative bias on the other hand stabilizes the MC-form. If the SAM is not irradiated with UV light the application of a potential bias has no effect

on the SP-LA headgroup. This result is important for the application of SP-LA in electrochemical sensors since it shows, that the potential range over which the MC-form could be used as the possible "On"-state is limited, but with the benefit that at a certain potential this sensor could be unambiguously switched "Off" when excess analyte needs to be removed.

Fitting Ambiguities

While homodyned SFG spectra gave some insight into the potential-dependent switching behavior of the SP-LA SAM uniquely fitting the such obtained spectra and unambiguously assigning individual resonances to functional groups within the molecule was hardly possible and required the comparison with bulk values from an ATR-FTIR spectrum taken, as well as literature values. Since in the homodyned case the intensity of the SFG response is detected the interference between the resonant and non-resonant SFG response of the molecules and the gold substrate respectively (proportional to their respective second order susceptibilities $\chi_R^{(2)}$ and $\chi_{NR}^{(2)}$) distorts the line shape depending on their often unknown relative phase relationship. During the application of an electric potential this relationship might additionally change. In contrast in heterodyned SFG spectra this problematic interference is resolved to a simple summation. Also fitting comes with additional constraints since the real and imaginary part of the SFG response are obtained separately but need to be fitted with the same fitting parameters simultaneously. Thus the fit's uniqueness could be enhanced. Chapter 7.1 presented the steps that need to be performed in order to correctly evaluate such heterodyned spectra for the exemplary case of an octadecanethiol (ODT) SAM attached to a gold surface and measured in air. Such way within the phase-resolved spectra the phase of $\chi_{NR}^{(2)}$ could be determined and it could be shown, that for gold it is influenced by the presence of a SAM as well as surface treatment (e.g. freshly evaporated or taken from the ozonator).
In contrast to the case in air for SFG measurements of SAM's at buried interfaces such as the SP-LA SAM at the gold electrode within a liquid cell simulta-

neous referencing so far was not possible, because SAM formation could not be restricted to the sample spot, but extended towards the reference spot. For geometrical reasons the latter had to be on the same substrate as the sample spot. In a future setup design sample and reference spot will be divided apart more clearly, but so far correcting for the spectral shape of the non-resonant background was here not possible, making the spectra more noisy and the absolute spectral phase unobtainable. Therefore phase-resolved measurements of SP-LA attached to a gold electrode have only been conducted to characterize the open and closed form without the application of a potential bias. Nevertheless fitting could be performed, basically corroborating the fitting values obtained for the homodyned data. It must be noted, however, that even though fitting heterodyned spectra in general give more accurate results the system is still under-determined and the fit still won't be unique. This problem is especially true if the spectra are more noisy and additional parameters for the Gaussian shaped background have to be introduced. Additional constraints are needed and in fact could be readily accessible if the difference frequency (DFG) response was recorded as well. Within our collinear setup the simultaneously created DFG response (so far filtered out) copropagates with the SFG one and could be easily separated in future measurements applying a dichroic mirror and photodiodes sensitive in the respective frequency range. Then two complex spectra with the same fitting parameters for the center frequencies and FWHM's, as well as amplitudes linked by multiplication with a constant would be available, further constraining the fit. Such a setup will be applied in future measurements.

Switching Kinetics

In addition to the spectra of the SP-LA SAM in its respective photostationary state the switching kinetics between the closed SP- and open MC-form has been monitored within the homodyned SFG setup (chapter 6.2). Two processes on distinct time scales have been observed of which the slow process is assumed to be connected to a tilt in the alkyl chain of the molecules' anchor group. To

verify this assumption kinetic measurements in the vibrational CH-stretch region were planned. The signal-to-noise ratio, however, was to poor. Due to the balanced detection scheme within the heterodyned SFG setup (presented in chapter 3.1.3) this spectral region became accessible and we could record spectra of the SP-LA alkyl chain (chapter 7.3.4). The current phase-resolved setup, however, is limited to static measurements since the interferometer is based on a (slow) step-scanning-approach. For future investigations the interferometer will apply a continuously running delay stage. This fast-scanning approach in combination with balanced detection, that minimizes the number of spectra to be averaged in order to achieve a sufficient signal-to-noise ratio, might even be able to disentangle the two processes that are usually associated with the switching of spiropyran derivatives, namely bond breaking at the spiro-center and reorientation of the headgroup. Both subsequent processes were assigned to the fast kinetic process observed in the homodyned spectra. The potential-dependent kinetic measurements (chapter 6.3.3) indicated a slow down of the switching process towards the open MC-form going from more positive values down to -520 mV (vs MSE). At even more negative values the velocity increased again. Which part of the switching process is most affected by the presence of an applied bias remains, however, unknown until the process of bond breaking and that of reorientation can be disentangled unambiguously.

Potential-dependent Nonlinear Background Contribution

One result of the fitted homodyned SFG response of SP-LA at a gold electrode was the supposed potential-dependence of the non-resonant substrate's response. This dependence was verified in phase-resolved measurements at a bare gold electrode presented in chapter 7.2 with an observed shift in the non-resonant substrate's phase of $\approx$20° as well as a decrease of its magnitude towards more negative potentials. In addition the influence of specific and non-specific adsorption has been investigated. It could be shown, that in the absence of specific adsorption and after correcting for the local field Fresnel shift

154

which was in close agreement to the theoretically calculated one the potential-dependence could be entirely related to the imaginary part of the complex spectrum. In contrast in the presence of specific adsorption (confirmed via a present Faradaic current in a subsequently taken CV over the same potential range) both the real and imaginary part showed a potential-dependence regardless of the applied Fresnel shift correction. The origin of this behavior, however, remains unclear. In the literature the real and imaginary part of the complex non-resonant SFG response have been assigned to intra- and inter-band transitions. Simultaneously it was assumed, that only intra-band transitions (and hence the real part) should be a affected by an applied potential in the absence of specific adsorption. This contradicts our observation implying that either the assignment is wrong or inter-band-transitions are mainly affected by an applied potential. Further measurements, that might additionally look at molecular vibrations of specifically adsorbed species are necessary to solve this contradiction.

However, the confirmed potential-dependence of the non-resonant background and especially its phase show the advantage of phase-resolved SFG measurements over their homodyned analogues in the characterization of electrochemical processes at interfaces. In those measurements a change in the non-resonant phase due to an applied potential and the resulting change of the spectral line shape could become the cause of serious misinterpretations. For instance an apparent change of the center frequencies of molecular vibrations within ions/molecules present at the electrode/electrolyte-interface could be misinterpreted as a Stark-shift. By enabling phase-resolved measurements at the electrode/electrolyte interface using the technique presented in this work, this thesis can be understood as a step towards a more unambiguous characterization of (fundamental) electrochemical processes which might help in the development of e.g. more effective electrode materials in fuel cells. Furthermore, the potential dependence of the non-resonant gold response could be exploited to "measure" local potentials at the electrode interface.

Gaining Access to Local Field Factors

Using the accuracy of simultaneous referencing it was possible to compare the sample spectrum to a reference one with known phase (e.g. z-cut alpha-quartz) to obtain its absolute phase. If molecules are present at the interface whose vibrational center frequencies are known, that absolute phase can be utilized to determine the phase shift introduced by the local field (L-)factors which mix the dispersive and absorptive line shapes otherwise expected entirely in the real or imaginary part respectively of the complex heterodyned spectrum. In the homodyned case only the magnitude of the L-factors influences the final spectrum. While the complex L_x and L_y-factor can be calculated from the linear Fresnel factors with the help of the complex refractive indices of the adjoining bulk phases, the L_z-factor additionally uses a scaling factor often called interfacial refractive index which influences its magnitude and so far had to be modeled. In measurements with more than one tensor component present the total Fresnel-shift depends on the relative magnitudes between the L-factors. Measuring the actual Fresnel-shift could in future measurements help to determine this relation and ultimately the interfacial refractive index.

Chapter A

Appendix

Fresnel Factors

The complex Fresnel factors were determined with the help of the program Wolfram Mathematica applying equations for their calculation which can be found in[56] (see also equation 2.18 in chapter 2.1.4). In the following the used Mathematica script is given in addition to annotations that explain the physical meaning of the employed variables. The latter is written in *italic* letters. The various input variables for a given experimental setting are listed in table A1.

Mathematica Script

Input:

```
deltaSFG = x[°]/180*Pi
deltaVis = x[°]/180*Pi
deltaIR = x[°]/180*Pi
```

Incident angles of the respective visible and IR input pulses as well as the resulting angle of the generated SFG pulse according to the experimental geometry. Actual values have to be inserted instead of x.

```
nSFG = x
kSFG = x
```

nVis = **x**

kVis = **x**

nIR = **x**

kIR = **x**

Real and imaginary part (n and k respectively) of the complex refractive index of the substrate at whose surface the SFG pulse is generated. Values are taken for the respective SFG, Vis and IR frequency.

incnSFG = **x**

inckSFG = **x**

incnVis = **x**

inckVis = **x**

incnIR = **x**

inckIR = **x**

Complex refractive index of the incidence medium (air, acetonitrile or deuterated water) at the respective frequencies.

Calculation:

betaSFG = ArcSin[(Sin[deltaSFG]/(incnSFG+i*inckSFG))]

betaVis = ArcSin[(Sin[deltaVis]/(incnVis+i*inckVis))]

betaIR = ArcSin[(Sin[deltaIR]/(incnIR+i*inckIR))]

Application of Snell's law to determine the angle of the incident pulses with respect to the substrate's surface normal. "ArcSin" in Mathematica refers to the trigonometric arcus sine, "Sin" to the sine function. Their arguments have to be given in [rad]. "i" refers to the imaginary unit.

gammaSFG = ArcSin[(Sin[betaSFG]/(nSFG+i*kSFG))]

gammaVis = ArcSin[(Sin[betaVis]/(nVis+i*kVis))]

gammaIR = ArcSin[(Sin[betaIR]/(nIR+i*kIR))]

Calculation of the refractive angle the respective pulse experiences passing from the incident medium into the substrate medium.

FSSFG=((incnSFG+i*inckSFG)*Cos[betaSFG]-(nSFG+i*kSFG)*Cos[gammaSFG])/ ((incnSFG+i*inckSFG)*Cos[betaSFG]+(nSFG+i*kSFG)*Cos[gammSFG])

FPSFG=((nSFG+i*kSFG)*Cos[betaSFG]-(incnSFG+i*inckSFG)*Cos[gammaSFG])/ ((incnSFG+i*inckSFG)*Cos[gammaSFG]+(nSFG+i*kSFG)*Cos[betaSFG])

FSVIS=((incnVIS+i*inckVIS)*Cos[betaVIS]-(nVIS+i*kVIS)*Cos[gammaVIS])/

((incnVIS+i*inckVIS)*Cos[betaVIS]+(nVIS+i*kVIS)*Cos[gammVIS])

FPVIS=((nVIS+i*kVIS)*Cos[betaVIS]-(incnVIS+i*inckVIS)*Cos[gammaVIS])/

((incnVIS+i*inckVIS)*Cos[gammaVIS]+(nVIS+i*kVIS)*Cos[betaVIS])

FSIR=((incnIR+i*inckIR)*Cos[betaIR]-(nIR+i*kIR)*Cos[gammaIR])/

((incnIR+i*inckIR)*Cos[betaIR]+(nIR+i*kIR)*Cos[gammIR])

FPIR=((nIR+i*kIR)*Cos[betaIR]-(incnIR+i*inckIR)*Cos[gammaIR])/

((incnIR+i*inckIR)*Cos[gammaIR]+(nIR+i*kIR)*Cos[betaIR])

Calculation of the linear Fresnel factors for the S- and P-polarized pulses, FSx and FPx respectively. [56] *"Cos" in Mathematica refers to the trigonometric Cosine function. The argument is given in [rad].*

LxxSFG = 1-FPSFG

LxxVis = 1-FPVis

LxxIR = 1-FPIR

LyySFG = 1+FSSFG

LyyVis = 1+FSVis

LyyIR = 1+FSIR

LzzSFG = (1+FPSFG)*((incnSFG+i*inckSFG)/(1.18))^2

LzzVis = (1+FPVis)*((incnVis+i*inckVis)/(1.18))^2

LzzIR = (1+FPIR)*((incnIR+i*inckIR)/(1.18))^2

Lzzz = LzzSFG*LzzVis*LzzIR

Lxxz = LxxSFG*LxxVis*LzzIR

Lxzx = LxxSFG*LzzVis*LxxIR

Lzxx = LzzSFG*LxxVis*LxxIR

Lyyz = LyySFG*LyyVis*LzzIR

Calculation of the respective nonlinear Fresnel factors [56] *for the non-zero tensor components of the second order nonlinear susceptibility for sum frequency generation at isotropic surfaces. For the Lzz factors the value of the interfacial refractive index, which influences the magnitude of the factor only, is taken to be 1.18 as is typically assumed for alkane monolayers.* [76]

PhiLzzz = Arg[Lzzz]*180/Pi

PhiLyyz = Arg[Lyyz]*180/Pi

The "Arg"-function yields the phase of the complex nonlinear Fresnel factor in [rad].

magLzzzSq = Abs[Lzzz]^2

magLyyzSq = Abs[Lyyz]^2

The "Abs"-function yields the magnitude of the complex nonlinear Fresnel factor.

Input Values and Results

Incident medium	Air		Acetonitrile		D$_2$O
Substrate	gold				
ω_{SFG}	645 nm				
ω_{Vis}	800 nm				
ω_{IR}	3300 nm				
	input				
deltaSFG	60°	70°	60°	70°	70°
deltaVis	65°	70°	65°	70°	70°
deltaIR	40°	70°	40°	70°	70°
nSFG	0.11522[175]				
kSFG	3.4542[175]				
nVis	0.11522[175]				
kVis	4.8339[175]				
nIR	0.63905[175]				
kIR	22.497[175]				
incnSFG	1		1.3391[176]		1.3268[177]
inckSFG	0		0		2.89e-08[177]
incnVis	1		1.3372[176]		1.3240[177]
inckVis	0		0		4.21e-08[177]
incnIR	1		1.3304[178]		1.3380*[179]
inckIR	0		0.0035131[178]		0.00845*[179]
	output				
PhiLzzz	59.9°	79.1°	51.7°	54.9°	52.1°
PhiLyyz	-161.1°	-160.5°	-145.7°	-146.2°	-145°
magLzzzSq	4.9335	3.3434	186.0580	177.8550	176.4680
magLyyzSq	0.0046	0.0014	0.3039	0.2491	0.2910

Table A1: Input variables and results for the calculation of the complex nonlinear Fresnel factors with the help of Wolfram Mathematica for different experimental settings. *Due to a lack of D$_2$O data at 3300 nm the corresponding refractive index of water at 4300 nm was used.
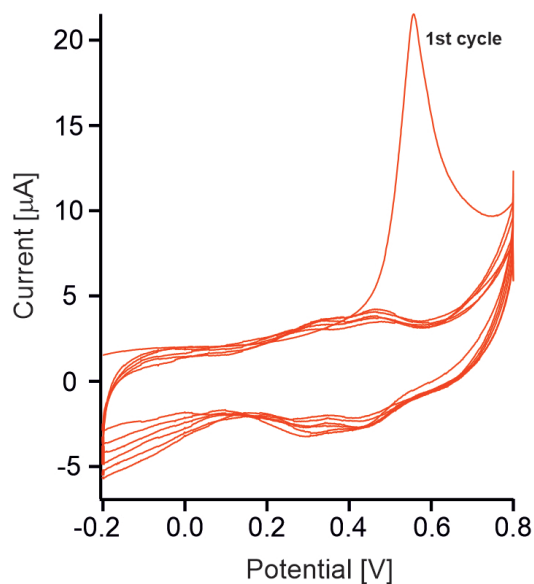
SP-LA Cyclic Voltammogram Reference Measurement

Figure A1: Cyclic voltammogram of SP-LA attached to a gold substrate. Potential measured against a mercury/mercury(II) sulfate reference electrode.
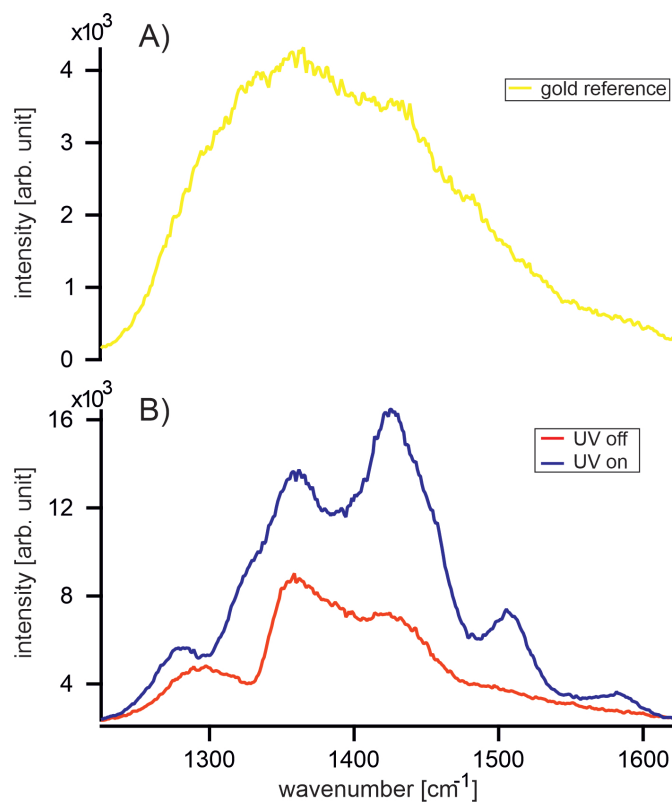
Unreferenced Homodyned SFG Spectrum of SP-LA

Figure A2: A) Gold reference spectrum by which the unreferenced SP-LA spectra in their respective SP- and MC-form shown in B) ultimately were divided for further evaluation.
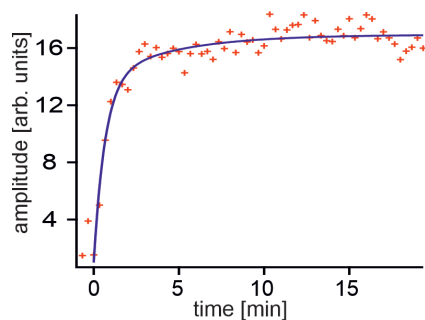
Peak Evolution During Switching

Figure A3: Amplitude development during switching for Peak around $1273\,cm^{-1}$.

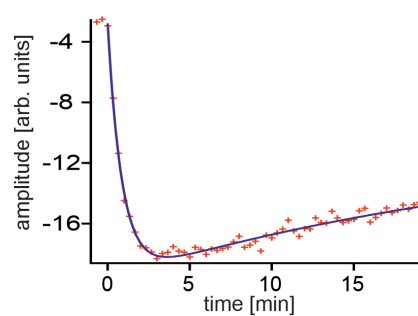Figure A4: Amplitude development during switching for Peak around $1307\,cm^{-1}$.

Figure A5: Amplitude development during switching for Peak around $1331\,cm^{-1}$.

Figure A6: Amplitude development during switching for Peak around $1353\,cm^{-1}$.

Figure A7: Amplitude development during switching for Peak around $1456\,cm^{-1}$.

Figure A8: Amplitude development during switching for Peak around $1474\,cm^{-1}$.

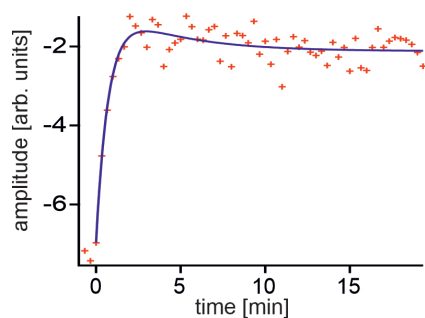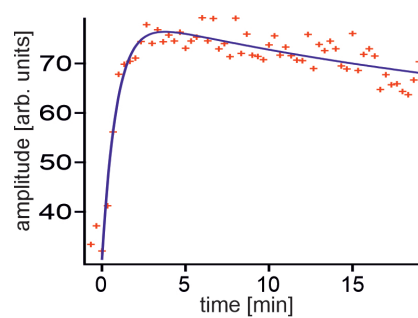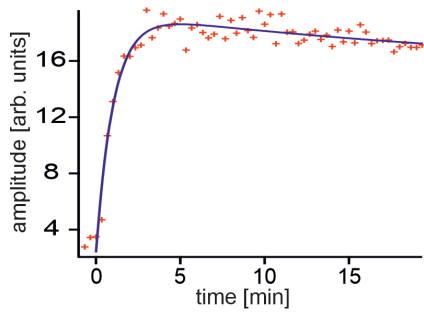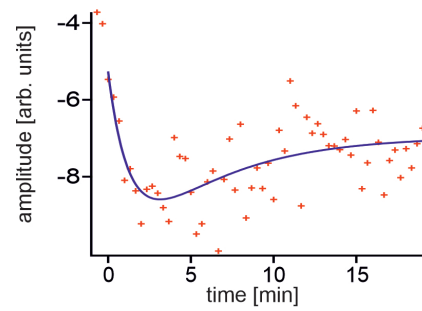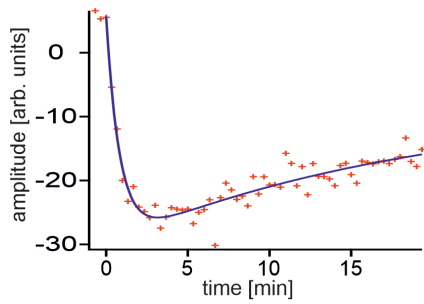
Figure A9: Amplitude development during switching for Peak around $1524\,cm^{-1}$.
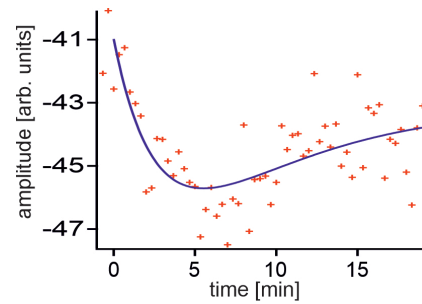
Figure A10: Amplitude development during switching for Peak around $1591\,cm^{-1}$.
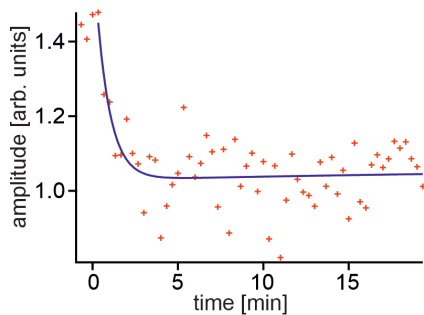
Figure A11: Non-resonant phase development during switching.
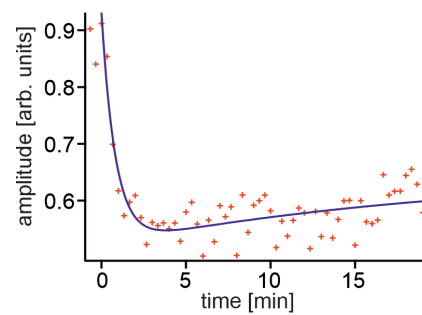
Figure A12: Non-resonant magnitude development during switching.

$\tilde{\nu}[cm^{-1}]$	y_0 [arb. units]	A_1 [arb. units]	A_2 [arb. units]
1273	16.93±0.30	-12.70±1.87	-3.24±1.68
1307	-10.26±3.53	16.85±0.42	-9.40±3.21
1331	-2.12±0.12	-6.13±1.03	1.29±0.98
1353	56.28±32.30	-49.93±3.37	23.92±29.81
1423	12.62±6.59	-17.70±0.74	6.26±6.09
1456	15.036±9.10	-17.13±1.03	4.46±8.24
1474	-7.00±0.57	5.56±4.56	-3.87±4.27
1509	22.639±5.95	40.19±1.17	17.26±5.10
1524	-7.98±9.42	35.64±2.32	-21.99±7.73
1591	-43.14±2.85	11.79±47.54	-9.64±45.18
$|\chi_{NR}^{(2)}|$	0.65±0.02	0.41±0.03	-0.13±0.03
Φ_{NR}	1.06±1.12	0.64±0.17	-0.04±1.04

Table A2: Remaining fitting constants of the resonances' amplitude development using the bi-exponential fit as given in equation 6.5 in chapter 6.2.

ODT SFG Spectrum: PPP vs SSP

Polarization dependent measurements (see figure A13) have been taken for an ODT SAM, which were prepared analogously to the SAM in the measurement discussed in chapter 7.1.4. The difference, however, was the substrate which in the former case has been a commercially available gold mirror, which has been exposed to ozone in an ozonator for several tens of minutes and whose consecutively determined effective non-resonant phase was $91.4°$. This time in contrast we used a freshly evaporated gold surface whose effective non-resonant phase has been determined to be $128.8°$ and $51.7°$ for PPP and SSP polarization combination respectively which makes up for most of the difference in the obtained fitting values (the rest being fitting ambiguities) for $\Phi_{S_{norm},NR}$ and $\Phi_{S_{norm},R}$ for the two PPP measurements (compare table 7.1 and table A3).

Interestingly for both the PPP and SSP measurement the formation of the ODT SAM shifted the NR phase, which is determined according to equation 7.12 and 7.14 as the difference of the fitting parameters $\Phi_{S_{norm},NR}$ and $\Phi_{S_{norm},R}$ (see table A3), to $84°$(PPP) and $95°$(SSP). These values are close to the $\approx 90°$ previously observed. This result supports the idea, that the substrates non-resonant phase critically depends on the oxidation state of the gold substrate.

Apart from the differences in the fitting parameters for the phases the resonant frequencies in table A3 are in close agreement with the previous measurement. Since the current measurement was recorded with a lower spectral resolution, the small features representing the gauche defects could not be resolved. As an additional consequence the full width at half maximum of the resolved features appears broader.
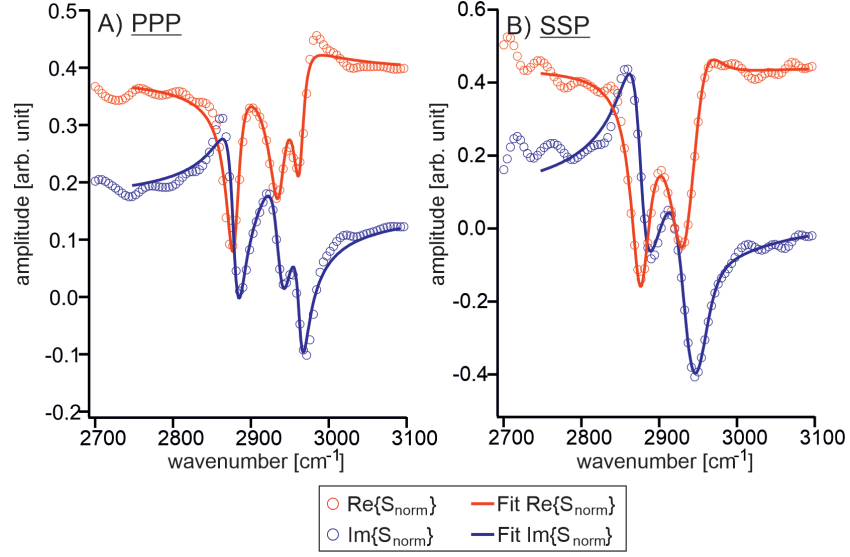
Figure A13: Fitted phase-resolved ODT spectra on gold. A) PPP polarization combination B) SSP polarization combination.

Assign.		PPP	SSP	Assign.		PPP	SSP
$\chi_{NR}^{(2)}$	$\lvert\chi_{NR}^{(2)}\rvert$	0.42	0.44	$\chi_{NR}^{(2)}$	$\Phi_{S_{norm},NR}$	22.2°	7.1°
$\nu_{sym}(CH_3)$	A	-2.87	7.98	$\nu_{Fermi}(CH_3)$	A	-2.48	12.46
	ω_q	2879	2876		ω_q	2937	2932
	Γ_q	9.84	14.85		Γ_q	12.00	22.29
$\nu_{asym}(CH_3)$	A	-1.77	-5.23	$\chi_R^{(2)}$	$\Phi_{S_{norm},R}$	-61.8°	91.9°
	ω_q	2963	2958				
	Γ_q	8.14	24.78				

Table A3: Fitting parameters of the ODT spectra shown in figure A13.

Potential-dependence of Non-Resonant Substrate Response: CVs
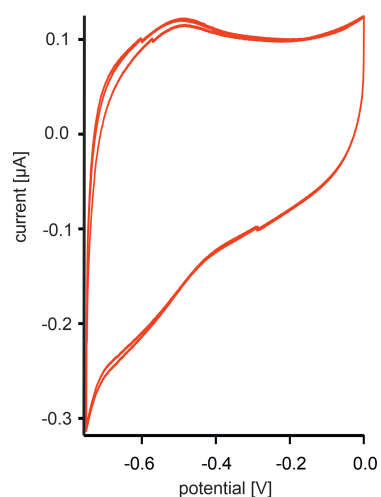
Figure A14: One round of cyclic voltammograms taken in between the static potential-dependent measurements of the non-resonant substrate response.
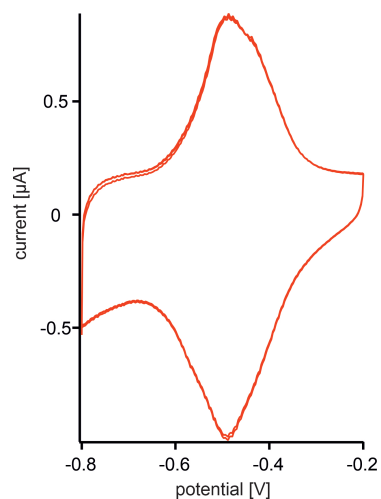
Figure A15: Cyclic voltammograms of the reversible adsorption and desorption of iodide anions. Potential measured against a gold pseudo-reference electrode.

Scanning Speed Dependent Potential-Dependence
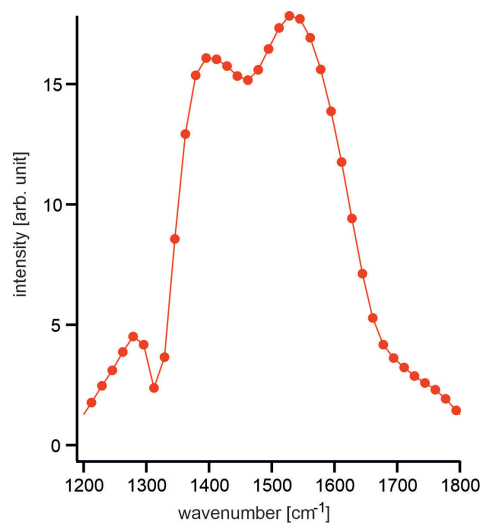
Figure A16: Magnitude spectrum that was obtained Fourier transforming the interferogram shown in figure 7.10C in chapter 7.2.2.
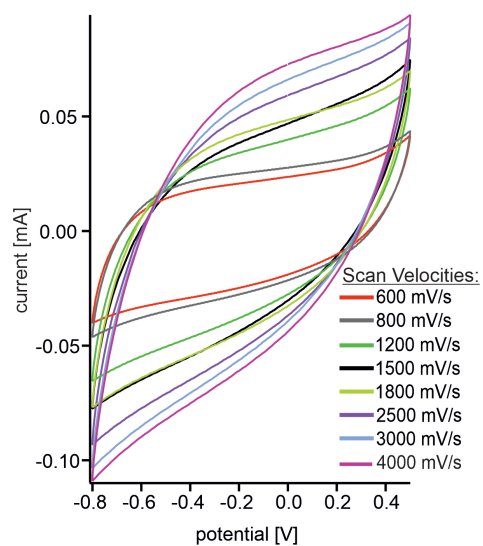
Figure A17: Each of the presented CVs shown acts as the representative for all CVs taken at a specific scanning speed.

Heterodyned SFG Spectrum of SP-LA on Gold in Air

Assign.		Value	Assign.		Value
$\chi^{(2)}_{NR}$	$\|\chi^{(2)}_{NR}\|$	0.93±0.01	$\chi^{(2)}_{NR}$	Φ	56.58°±2.18° (0.46-(-56.12))
$\nu(C-N)$	A	0.73±0.30	$\nu(C-N^+)$	A	-34.15±52.14
	ω_q	1237±2		ω_q	1320±5
	Γ_q	12.67±4.16		Γ_q	29.00±6.67
$\nu_{sym}(NO_2)$	A	82.71±40.53	$\nu(CH_3)$	A	-29.17±52.80
	ω_q	1335±22		ω_q	1355±6
	Γ_q	40.48±5.20		Γ_q	28.60±9.77
$\nu(CO^-)$	A	0.43±12.88	$\nu(C-C_{arom})$	A	2.60±12.81
	ω_q	1434±297		ω_q	1457±14
	Γ_q	31.52±317.03		Γ_q	18.27±33.92
$\nu(C-C_{arom})$	A	0.976±4.21	$\nu_{asym}(NO_2)$	A	3.69±0.99
	ω_q	1470±6		ω_q	1515±2
	Γ_q	10.81±14.65		Γ_q	20.61±3.77
$\nu(C-C_{arom})$	A	20.61±3.76	$\nu(C=N^+)$	A	-8.76±1.10
	ω_q	1549±2		ω_q	1578±2
	Γ_q	14.22±4.82		Γ_q	27.71±2.10

Table A4: Fitting parameters of the normalized phase-resolved SFG spectrum of an SP-LA SAM at gold, measured in air. 10 resonances assumed.

Assign.		Value	Assign.		Value
$\chi_{NR}^{(2)}$	$\lvert\chi_{NR}^{(2)}\rvert$	0.94±0.01	$\chi_{NR}^{(2)}$	Φ	52.28°±2.38° (0.32-(-51.95))
$\nu(C-N)$	A	8.64±1.55	$\nu(C-N^+)$	A	-0.24±0.26
	ω_q	1269±4		ω_q	1300±3
	Γ_q	50.96±6.40		Γ_q	7.38±5.98
$\nu_{sym}(NO_2)$	A	3.91±0.26	$\nu(CH_3)$	A	1.06±0.54
	ω_q	1337±1		ω_q	1399±2
	Γ_q	10.11±0.53		Γ_q	11.98±3.70
$\nu(CO^-)$	A	1.48±1.45	$\nu(C-C_{arom})$	A	—
	ω_q	1428±5		ω_q	—
	Γ_q	21.32±14.38		Γ_q	—
$\nu(C-C_{arom})$	A	4.73±1.05	$\nu_{asym}(NO_2)$	A	3.50±0.58
	ω_q	1463±2		ω_q	1516±2
	Γ_q	20.39±2.71		Γ_q	19.90±2.69
$\nu(C-C_{arom})$	A	0.81±0.52	$\nu(C=N^+)$	A	11.28±1.10
	ω_q	1548±2		ω_q	1577±2
	Γ_q	10.61±4.36		Γ_q	32.48±2.17

Table A5: Fitting parameters of the normalized phase-resolved SFG spectrum of an SP-LA SAM at gold, measured in air. 9 resonances assumed.
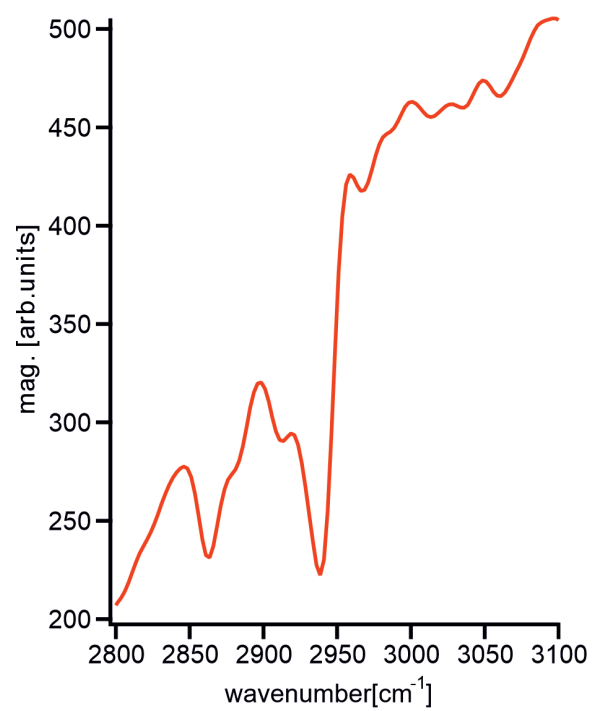
Figure A18: SP-LA SAM in air; Unreferenced magnitude spectrum.

Bibliography

[1] S. O. Amrouche. Overview of energy storage in renewable energy systems. Int. J. Hydrog. Energy, 41(45):20914–20927, December 2016.

[2] A. Eftekhari. Energy efficiency: a critically important but neglected factor in battery research. Sustain. Energ. Fuels, 1(10):2053–2060, 2017.

[3] P. Wang, K. Jiang, G. Wang, J. Yao, and X. Huang. Phase and Interface Engineering of Platinum-Nickel Nanowires for Efficient Electrochemical Hydrogen Evolution. Angew. Chem., 128(41):13051–13055, October 2016.

[4] Z. Wu, X. Guo, Z. Zhang, M. Song, T. Jiao, Y. Zhu, J. Wang, and X. Liu. Interface Engineering of MoS$_2$ for Electrocatalytic Performance Optimization for Hydrogen Generation via Urea Electrolysis. ACS Sustainable Chem. Eng., 7(19):16577–16584, October 2019.

[5] M. Zhou and J. Wang. Biofuel Cells for Self-Powered Electrochemical Biosensing and Logic Biosensing: A Review. Electroanalysis, 24(2):197–209, February 2012.

[6] W. Cheng, L. Ding, S. Ding, Y. Yin, and H. Ju. A Simple Electrochemical Cytosensor Array for Dynamic Analysis of Carcinoma Cell Surface Glycans. Angew. Chem. Int. Ed., 48(35):6465–6468, August 2009.

[7] C. Mousty. Biosensing applications of clay-modified electrodes: a review. Anal. Bioanal. Chem., 396(1):315–325, January 2010.

[8] Y. Fu, C. Chen, Q. Xie, X. Xu, C. Zou, Q. Zhou, L. Tan, H. Tang, Y. Zhang, and S. Yao. Immobilization of Enzymes through One-Pot Chemical Pre-oxidation and Electropolymerization of Dithiols in Enzyme-Containing Aqueous Suspensions To Develop Biosensors with Improved Performance. Anal. Chem., 80(15):5829–5838, August 2008.

[9] I. Willner and M. Zayats. Electronic Aptamer-Based Sensors. Angew. Chem. Int. Ed., 46(34):6408–6418, August 2007.

[10] Y. Fu, Z. Callaway, J. Lum, R. Wang, J. Lin, and Y. Li. Exploiting Enzyme Catalysis in Ultra-Low Ion Strength Media for Impedance Biosensing of Avian Influenza Virus Using a Bare Interdigitated Electrode. Anal. Chem., 86(4):1965–1971, February 2014.

[11] M. Asif, M. Ajmal, G. Ashraf, N. Muhammad, A. Aziz, T. Iftikhar, J. Wang, and H. Liu. The role of biosensors in COVID-19 outbreak. Curr. Opin. Electrochem., page S2451910320301654, September 2020.

[12] X. Xie, G. Mistlberger, and E. Bakker. Reversible Photodynamic Chloride-Selective Sensor Based on Photochromic Spiropyran. J. Am. Chem. Soc., 134(41):16929–16932, October 2012.

[13] J.-I. Anzai, K. Sakamura, Y. Hasebe, and T. Osa. Protein sensors based on the potentiometric photoresponse of polymer membranes doped with photochromic spiropyran. Anal. Chim. Acta, 281(3):543–548, September 1993.

[14] I. Willner, R. Blonder, and A. Dagan. Application of photoisomerizable antigenic monolayer electrodes as reversible amperometric immunosensors. J. Am. Chem. Soc., 116(20):9365–9366, 1994.

[15] M. Che. Nobel Prize in chemistry 1912 to Sabatier: Organic chemistry or catalysis? Catal. Today, 218-219:162–171, December 2013.

[16] G. Ertl. Elementarschritte bei der heterogenen Katalyse. Angew. Chem., 102(11):1258–1266, November 1990.

[17] A. J. Medford, A. Vojvodic, J. S. Hummelshøj, J. Voss, F. Abild-Pedersen, F. Studt, T. Bligaard, A. Nilsson, and J. K. Nørskov. From the Sabatier principle to a predictive theory of transition-metal heterogeneous catalysis. J. Catal., 328:36–42, August 2015.

[18] G. A. Somorjai. Modern Surface Science and Surface Technologies: An Introduction. Chem. Rev., 96(4):1223–1236, January 1996.

[19] G. Ertl. Surface Science and Catalysis—Studies on the Mechanism of Ammonia Synthesis: The P. H. Emmett Award Address. Cataly. Rev., 21(2):201–223, January 1980.

[20] C. T. Campbell. Cesium-promoted silver(111): model studies of selective ethylene oxidation catalysts. J. Phys. Chem., 89(26):5789–5795, December 1985.

[21] J. E. Demuth, D. W. Jepsen, and P. M. Marcus. Crystallographic Dependence of Chemisorption Bonding for Sulfur on (001), (110), and (111) Nickel. Phys. Rev. Lett., 32(21):1182–1185, May 1974.

[22] G. A. Somorjai and J. Carrazza. Structure sensitivity of catalytic reactions. Ind. Eng. Chem. Fund., 25(1):63–69, February 1986.

[23] M. P. Seah. A review of the analysis of surfaces and thin films by AES and XPS. Vacuum, 34(3-4):463–478, March 1984.

[24] J. Odriozola. AES and TDS study of the adsorption of NH3 and NO on V2O5 and TiO2 surfaces: Mechanistic implications. J. Catal., 119(1):71–82, September 1989.

[25] M. Takagi-Kawai, M. Soma, T. Onishi, and K. Tamaru. The adsorption and the reaction of NH_3 and NO_x on supported V_2O_5 catalysts: effect of supporting materials. Can. J. Chem., 58(20):2132–2137, October 1980.

[26] P. Liao. Activity and XPS studies of sulfur poisoning effect on Pt-Cu/gamma-Al2O3 oxidation catalysts. J. Catal., 75(2):396–403, June 1982.

[27] C. H. Wu, B. Eren, and M. B. Salmeron. Structure and Dynamics of Reactant Coadsorption on Single Crystal Model Catalysts by HP-STM and AP-XPS: A Mini Review. Top. Catal., 59(5-7):405–419, March 2016.

[28] L. R. Danielson, M. J. Dresser, E. E. Donaldson, and J. T. Dickinson. Adsorption and desorption of ammonia, hydrogen, and nitrogen on ruthenium (0001). Surf. Sci., 71(3):599–614, February 1978.

[29] G. Ertl. Primary steps in catalytic synthesis of ammonia. J. Vac. Sci. Technol. A, 1(2):1247–1253, April 1983.

[30] F. Besenbacher, E. Laegsgaard, I. Stensgaard, P. Stoltze, and H. Topsoe. Scanning tunneling microscopy characterization of ammonia synthesis catalysts. Catal. Lett., 8(5-6):273–282, 1991.

[31] F. Atamny, D. Duff, and A. Baiker. STM and TEM investigation of a technical platinum/graphite catalyst. Catal. Lett., 34(3-4):305–311, 1995.

[32] R. Erlandsson. Gas-induced restructuring of palladium model catalysts studied with atomic force microscopy. J. Vac. Sci. Technol. B, 9(2):825, March 1991.

[33] K. H. Lee and E. E. Wolf. AFM studies of Pd silica supported thin film catalysts. Catal. Lett., 26(3-4):297–314, 1994.

[34] G. Ertl. Heterogeneous catalysis on the atomic scale. Chem. Rec., 1:33–45, 2001.

[35] S. H. Kim and G. A. Somorjai. Surface science of single-site heterogeneous olefin polymerization catalysts. P. Natl. A. Sci., 103(42):15289–15294, October 2006.

[36] J. Greeley. Theoretical Heterogeneous Catalysis: Scaling Relationships and Computational Catalyst Design. Annu. Rev. Chem. Biomol. Eng., 7(1):605–635, June 2016.

[37] Y.R Shen. Surfaces probed by nonlinear optics. Surf. Sci., 299-300:551–562, January 1994.

[38] Y.R. Shen. Phase-Sensitive Sum-Frequency Spectroscopy. <u>Annu. Rev. Phys. Chem.</u>, 64(1):129–150, April 2013.

[39] Y. R. Shen. Optical second harmonic generation at interfaces. <u>Annu. Rev. Phys. Chem.</u>, 40(1):327–350, 1989.

[40] A. G. Lambert, P. B. Davies, and D. J. Neivandt. Implementing the Theory of Sum Frequency Generation Vibrational Spectroscopy: A Tutorial Review. <u>Appl. Spectrosc. Rev.</u>, 40(2):103–145, May 2005.

[41] J. P. Smith and V. Hinson-Smith. Product Review: SFG coming of age. <u>Anal. Chem.</u>, 76(15):287 A–290 A, August 2004.

[42] H.-F. Wang, W. Gan, R. Lu, Y. Rao, and B.-H. Wu. Quantitative spectral and orientational analysis in surface sum frequency generation vibrational spectroscopy (SFG-VS). <u>Int. Rev. Phys. Chem.</u>, 24(2):191–256, April 2005.

[43] C. Hirose, N. Akamatsu, and K. Domen. Formulas for the analysis of surface sum-frequency generation spectrum by CH stretching modes of methyl and methylene groups. <u>J. Chem. Phys.</u>, 96(2):997, 1992.

[44] G. L. Richmond, J. M. Robinson, and V. L. Shannon. Second harmonic generation studies of interfacial structure and dynamics. <u>Prog. Surf. Sci.</u>, 28(1):1–70, 1988.

[45] A. Tadjeddine, A. Le Rille, O. Pluchery, F. Vidal, W. Q. Zheng, and A. Peremans. Sum and Difference Frequency Generation at the Electrochemical Interface. <u>Phys. Stat. Sol. A</u>, 175(1):89–107, September 1999.

[46] B. Pettinger, J. Lipkowski, and S. Mirwald. In situ SHG studies of adsorption induced surface reconstruction of Au(111)-electrodes. <u>Electrochim. Acta</u>, 40(1):133–142, January 1995.

[47] J. Rudnick and E. A. Stern. Second-Harmonic Radiation from Metal Surfaces. <u>Phys. Rev. B</u>, 4(12):4274–4290, December 1971.

[48] N. Bloembergen, R. K. Chang, S. S. Jha, and C. H. Lee. Optical Second-Harmonic Generation in Reflection from Media with Inversion Symmetry. Phys. Rev., 174(3):813–822, October 1968.

[49] J. E. Sipe, V. C. Y. So, M. Fukui, and G. I. Stegeman. Analysis of second-harmonic generation at metal surfaces. Phys. Rev. B, 21(10):4389–4402, May 1980.

[50] A. V. Petukhov. Sum-frequency generation on isotropic surfaces: General phenomenology and microscopic theory for jellium surfaces. Phys. Rev. B, 52(23):16901–16911, December 1995.

[51] P. Guyot-Sionnest and A. Tadjeddine. Study of Ag(111) and Au(111) electrodes by optical second-harmonic generation. J. Chem. Phys., 92(1):734–738, January 1990.

[52] B. Pettinger and C. Bilger. A novel approach to analyze the optical second harmonic generation anisotropy at surfaces employing interference techniques. Example: the Au(110) electrode. Chem. Phys. Lett., 286(3-4):355–360, April 1998.

[53] Z. Shi, J. Lipkowski, S. Mirwald, and B. Pettinger. Electrochemical and second harmonic generation study of bromide adsorption at the Au(111) electrode surface. Faraday Trans., 92(20):3737, 1996.

[54] C. Bilger and B. Pettinger. Potential dependence of the non-linear polarizability of an Au (110) electrode. J. Chem. Soc. Faraday T., 94(18):2795–2801, 1998.

[55] N. Ji, V. Ostroverkhov, C.-Y. Chen, and Y. R. Shen. Phase-Sensitive Sum-Frequency Vibrational Spectroscopy and Its Application to Studies of Interfacial Alkyl Chains. J. Am. Chem. Soc., 129(33):10056–10057, August 2007.

[56] Y. Tong, Y. Zhao, N. Li, M. Osawa, P. B. Davies, and S. Ye. Interference effects in the sum frequency generation spectra of thin organic films. I.

Theoretical modeling and simulation. J. Chem. Phys., 133(3):034704, 2010.

[57] S. Nihonyanagi, J. A. Mondal, S. Yamaguchi, and T. Tahara. Structure and Dynamics of Interfacial Water Studied by Heterodyne-Detected Vibrational Sum-Frequency Generation. Annu. Rev. Phys. Chem., 64(1):579–603, April 2013.

[58] Y. R. Shen. Fundamentals of Sum-Frequency Spectroscopy. Cambridge University Press, 2016.

[59] S. Nihonyanagi, S. Yamaguchi, and T. Tahara. Direct evidence for orientational flip-flop of water molecules at charged interfaces: A heterodyne-detected vibrational sum frequency generation study. J. Chem. Phys., 130(20):204704, 2009.

[60] S. Sun, R. Liang, X. Xu, H. Zhu, Y. R. Shen, and C. Tian. Phase reference in phase-sensitive sum-frequency vibrational spectroscopy. J. Chem. Phys., 144(24):244711, June 2016.

[61] S. Nihonyanagi, T. Ishiyama, T.-K. Lee, S. Yamaguchi, M. Bonn, A. Morita, and T. Tahara. Unified Molecular View of the Air/Water Interface Based on Experimental and Theoretical $x^{(2)}$ Spectra of an Isotopically Diluted Water Surface. J. Am. Chem. Soc., 133(42):16875–16880, October 2011.

[62] S. Nihonyanagi, R. Kusaka, K.-I. Inoue, A. Adhikari, S. Yamaguchi, and T. Tahara. Accurate determination of complex $x^{(2)}$ spectrum of the air/water interface. J. Chem. Phys., 143(12):124707, September 2015.

[63] C.-S. Tian and Y. R. Shen. Isotopic Dilution Study of the Water/Vapor Interface by Phase-Sensitive Sum-Frequency Vibrational Spectroscopy. J. Am. Chem. Soc., 131(8):2790–2791, March 2009.

[64] A. M. Gardner, K. H. Saeed, and A. J. Cowan. Vibrational sum-frequency generation spectroscopy of electrode surfaces: studying the mecha-

nisms of sustainable fuel generation and utilisation. Phys. Chem. Chem. Phys., 21(23):12067–12086, 2019.

[65] R. W. Boyd. Nonlinear Optics. Elsevier, 2003.

[66] M. B. Feller, W. Chen, and Y. R. Shen. Investigation of surface-induced alignment of liquid-crystal molecules by optical second-harmonic generation. Phys. Rev. A, 43(12):6778–6792, June 1991.

[67] P. B. Miranda and Y. R. Shen. Liquid Interfaces: A Study by Sum-Frequency Vibrational Spectroscopy. J. Phys. Chem. B, 103(17):3292–3307, April 1999.

[68] Z. Chen, Y. R. Shen, and G. A. Somorjai. Studies of polymer surfaces by sum frequency generation vibrational spectroscopy. Annu. Rev. Phys. Chem., 53(1):437–465, October 2002.

[69] C. Humbert, T. Noblet, L. Dalstein, B. Busson, and G. Barbillon. Sum-Frequency Generation Spectroscopy of Plasmonic Nanomaterials: A Review. Materials, 12(5):836, March 2019.

[70] P. Guyot-Sionnest, J. H. Hunt, and Y. R. Shen. Sum-frequency vibrational spectroscopy of a Langmuir film: Study of molecular orientation of a two-dimensional system. Phys. Rev. Lett., 59(14):1597–1600, October 1987.

[71] L. J. Richter, T. P. Petralli-Mallow, and J. C. Stephenson. Vibrationally resolved sum-frequency generation with broad-bandwidth infrared pulses. Opt. Lett., 23(20):1594–1596, 1998.

[72] F. Vidal and A. Tadjeddine. Sum-frequency generation spectroscopy of interfaces. Rep. Prog. Phys., 68(5):1095–1127, May 2005.

[73] M. Buck and M. Himmelhaus. Vibrational spectroscopy of interfaces by infrared–visible sum frequency generation. J. Vac. Sci. Technol. A, 19(6):2717, 2001.

[74] R. Superfine, J.Y. Huang, and Y.R. Shen. Experimental determination of the sign of molecular dipole moment derivatives: an infrared—visible sum frequency generation absolute phase measurement study. Chem. Phys. Lett., 172(3-4):303–306, September 1990.

[75] G. Bell, C. D. Bain, and R. N. Ward. Sum-frequency vibrational spectroscopy of soluble surfactants at the air/water interface. Faraday Trans., 92(4):515, 1996.

[76] X. Zhuang, P. B. Miranda, D. Kim, and Y. R. Shen. Mapping molecular orientation and conformation at interfaces by surface nonlinear optics. Phys. Rev. B, 59(19):12632–12640, May 1999.

[77] K.A. Friedrich and G.L. Richmond. Surface second harmonic generation studies of stepped Ag (111) electrode surfaces. Chem. Phys. Lett., 213(5-6):491–497, October 1993.

[78] E. K. L. Wong and G. L. Richmond. Examination of the surface second harmonic response from noble metal surfaces at infrared wavelengths. J. Chem. Phys., 99(7):5500–5507, October 1993.

[79] M.-L. Thèye. Investigation of the Optical Properties of Au by Means of Thin Semitransparent Films. Phys. Rev. B, 2(8):3060–3078, October 1970.

[80] S. Mirwald, B. Pettinger, and J. Lipkowski. Sulfate adsorption at Au(111) electrodes: an optical second harmonic generation study. Surf. Sci., 335:264–272, July 1995.

[81] D. M. Kolb and C. Franke. Surface states at the metal-electrolyte interface. Appl. Phys. A, 49(4):379–387, October 1989.

[82] B. Busson and L. Dalstein. Nonlinear optical response of a gold surface in the visible range: A study by two-color sum-frequency generation spectroscopy. III. Simulations of the experimental SFG intensities. J. Chem. Phys., 149(15):154701, October 2018.

182

[83] A. Liebsch. Theory of sum frequency generation from metal surfaces. Appl. Phys. B-Lasers O., 68(3):301–304, March 1999.

[84] G. Gonella, C. Lütgebaucks, A. G. F. de Beer, and S. Roke. Second Harmonic and Sum-Frequency Generation from Aqueous Interfaces Is Modulated by Interference. J. Phys. Chem. C, 120(17):9165–9173, May 2016.

[85] A. G. F. de Beer, R. K. Campen, and S. Roke. Separating surface structure and surface charge with second-harmonic and sum-frequency scattering. Phys. Rev. B, 82(23):235431, December 2010.

[86] F. M. Geiger. Second Harmonic Generation, Sum Frequency Generation, and x $^{(3)}$: Dissecting Environmental Interfaces with a Nonlinear Optical Swiss Army Knife. Annu. Rev. Phys. Chem., 60(1):61–83, May 2009.

[87] C. H. Lee, R. K. Chang, and N. Bloembergen. Nonlinear Electroreflectance in Silicon and Silver. Phys. Rev. Lett., 18(5):167–170, January 1967.

[88] O. A. Aktsipetrov, I. M. Baranova, L. V. Grigor'eva, K. N. Evtyukhov, E. D. Mishina, T. V. Murzina, and I. V. Chernyĭ. Second harmonic generation at a semiconductor–electrolyte interface and investigation of the surface of silicon by the nonlinear electroreflection method. Sov. J. Quantum Electron., 21(8):854–859, August 1991.

[89] A. A. Kornyshev and I. Vilfan. Phase transitions at the electrochemical interface. Electrochim. Acta, 40(1):109–127, January 1995.

[90] J. Schneider and D.M. Kolb. Potential-induced surface reconstruction of Au(100). Surf. Sci., 193(3):579–592, January 1988.

[91] B. Busson and A. Tadjeddine. Non-Uniqueness of Parameters Extracted from Resonant Second-Order Nonlinear Optical Spectroscopies. J. Phys. Chem. C, 113(52):21895–21902, December 2009.

[92] I. V. Stiopkin, H. D. Jayathilake, A. N. Bordenyuk, and A. V. Bender-skii. Heterodyne-Detected Vibrational Sum Frequency Generation Spectroscopy. J. Am. Chem. Soc., 130(7):2271–2275, February 2008.

[93] X. Chen, W. Hua, Z. Huang, and H. C. Allen. Interfacial Water Structure Associated with Phospholipid Membranes Studied by Phase-Sensitive Vibrational Sum Frequency Generation Spectroscopy. J. Am. Chem. Soc., 132(32):11336–11342, August 2010.

[94] M. Thämer, R. K. Campen, and M. Wolf. Detecting weak signals from interfaces by high accuracy phase-resolved SFG spectroscopy. Phys. Chem. Chem. Phys., 20(40):25875–25882, 2018.

[95] S. Roke, A. W. Kleyn, and M. Bonn. Time- vs. frequency-domain femtosecond surface sum frequency generation. Chem. Phys. Lett., 370(1-2):227–232, March 2003.

[96] Y. Tong, J. Wirth, H. Kirsch, M. Wolf, P. Saalfrank, and R. K. Campen. Optically probing Al—O and O—H vibrations to characterize water adsorption and surface reconstruction on alpha-alumina: An experimental and theoretical study. J. Chem. Phys., 142(5):054704, February 2015.

[97] T. Garling, Y. Tong, T. A. Darwish, M. Wolf, and R. K. Campen. The influence of surface potential on the optical switching of spiropyran self assembled monolayers. J. Phys.-Condens. Mat., 29(41):414002, October 2017.

[98] J. E. Laaser, W. Xiong, and M. T. Zanni. Time-Domain SFG Spectroscopy Using Mid-IR Pulse Shaping: Practical and Intrinsic Advantages. J. Phys. Chem. B, 115(11):2536–2546, March 2011.

[99] J. Areephong, W. R. Browne, N. Katsonis, and B. L. Feringa. Photo- and electro-chromism of diarylethene modified ITO electrodes—towards molecular based read–write–erase information storage. Chem. Commun., (37):3930–3932, 2006.

[100] N. Katsonis, M. Lubomska, M. Pollard, B. L. Feringa, and P. Rudolf. Synthetic light-activated molecular switches and motors on surfaces. Prog. Surf. Sci., 82(7-8):407–434, 2007.

[101] N. Crivillers, E. Orgiu, F. Reinders, M. Mayor, and P. Samorì. Optical Modulation of the Charge Injection in an Organic Field-Effect Transistor Based on Photochromic Self-Assembled-Monolayer-Functionalized Electrodes. Adv. Mater., 23(12):1447–1452, March 2011.

[102] I. Vlassiouk, C.-D. Park, S. A. Vail, D. Gust, and S. Smirnov. Control of Nanopore Wetting by a Photochromic Spiropyran: A Light-Controlled Valve and Electrical Switch. Nano Lett., 6(5):1013–1017, May 2006.

[103] R. Blonder, I. Willner, and A. F. Bückmann. Reconstitution of apo-glucose oxidase on nitrospiropyran and FAD mixed monolayers on gold electrodes: photostimulation of bioelectrocatalytic features of the biocatalyst. J. Am. Chem. Soc., 120(36):9335–9341, 1998.

[104] G. Wang, A. K. Bohaty, I. Zharov, and H. S. White. Photon Gated Transport at the Glass Nanopore Electrode. J. Am. Chem. Soc., 128(41):13553–13558, October 2006.

[105] J. Tao, P. Zhao, Y. Li, W. Zhao, Y. Xiao, and R. Yang. Fabrication of an electrochemical sensor based on spiropyran for sensitive and selective detection of fluoride ion. Anal. Chim. Acta, 918:97–102, April 2016.

[106] K. Nishinari, Y. Okada, A. Schadschneider, and D. Chowdhury. Intracellular Transport of Single-Headed Molecular Motors KIF1A. Phys. Rev. Lett., 95(11):118101, September 2005.

[107] B. L. Feringa. The Art of Building Small: From Molecular Switches to Motors (Nobel Lecture). Angew. Chem. Int. Ed., 56(37):11060–11078, September 2017.

[108] J. T. McIlwain, editor. An Introduction to the Biology of Vision. Cambridge University Press, 1 edition, November 1996.

[109] The Nobel Prize in Chemistry 2016, Press Release. page 1, October 2016.

[110] B. L. Feringa, W. F. Jager, and B. de Lange. Organic materials for reversible optical data storage. Tetrahedron, 49(37):8267–8310, January 1993.

[111] R. Klajn. Spiropyran-based dynamic materials. Chem. Soc. Rev., 43(1):148–184, 2014.

[112] J. Ratner, N. Kahana, A. Warshawsky, and V. Krongauz. Photochromic Polysulfones. 2. Photochromic Properties of Polymeric Polysulfone Carrying Pendant Spiropyran and Spirooxazine Groups. Ind. Eng. Chem. Res., 35(4):1307–1315, January 1996.

[113] J. T. C. Wojtyk, A. Wasey, N.-N. Xiao, P. M. Kazmaier, S. Hoz, C. Yu, R. P. Lemieux, and E. Buncel. Elucidating the Mechanisms of Acidochromic Spiropyran-Merocyanine Interconversion. J. Phys. Chem. A, 111(13):2511–2516, April 2007.

[114] F. M. Raymo and S. Giordani. Signal Processing at the Molecular Level. J. Am. Chem. Soc., 123(19):4651–4652, May 2001.

[115] W. Qiu, P. A. Gurr, G. da Silva, and G. G. Qiao. Insights into the mechanochromism of spiropyran elastomers. Polym. Chem., 10(13):1650–1659, 2019.

[116] S. Wan, Z. Ma, C. Chen, F. Li, F. Wang, X. Jia, W. Yang, and M. Yin. A Supramolecule-Triggered Mechanochromic Switch of Cyclodextrin-Jacketed Rhodamine and Spiropyran Derivatives. Adv. Funct. Mater., 26(3):353–364, January 2016.

[117] K. Wagner, R. Byrne, M. Zanoni, S. Gambhir, L. Dennany, R. Breukers, M. Higgins, P. Wagner, D. Diamond, G. G. Wallace, and D. L. Officer. A Multiswitchable Poly(terthiophene) Bearing a Spiropyran Functionality: Understanding Photo- and Electrochemical Control. J. Am. Chem. Soc., 133(14):5453–5462, April 2011.

[118] R. Rosario, D. Gust, M. Hayes, F. Jahnke, J. Springer, and A. A. Garcia. Photon-Modulated Wettability Changes on Spiropyran-Coated Surfaces. Langmuir, 18(21):8062–8069, October 2002.

[119] M. Plaschke, R. Czolk, and H.J. Ache. Fluorimetric determination of mercury with a water-soluble porphyrin and porphyrin-doped sol-gel films. Anal. Chim. Acta, 304(1):107–113, March 1995.

[120] M. Sakuragi, K. Aoki, T. Tamaki, and K. Ichimura. The Role of Triplet State of Nitrospiropyran in Their Photochromic Reaction. BCSJ, 63(1):74–79, January 1990.

[121] Y. Strokach, M. Alfimov, V. Barachevsky, V. Arsenov, and A. Gorelik. Relative Investigation of the Properties for Monomer and Dimer Photochromic Spirocompounds. Mol. Cryst. Liq. Crys. A, 298(1):97–103, May 1997.

[122] K. Sumaru, M. Kameda, T. Kanamori, and T. Shinbo. Characteristic Phase Transition of Aqueous Solution of Poly(N -isopropylacrylamide) Functionalized with Spirobenzopyran. Macromolecules, 37(13):4949–4955, June 2004.

[123] M.-H. Lee, X. Li, and E. Kim. Preparation of Photochromic Cellulose Derivatives Containing Spirobenzopyran. Mol. Cryst. Liq. Crys. A, 349(1):51–54, September 2000.

[124] B. K. Pathem, S. A. Claridge, Y. B. Zheng, and P. S. Weiss. Molecular Switches and Motors on Surfaces. Annu. Rev. Phys. Chem., 64(1):605–630, April 2013.

[125] M. Wolf and P. Tegeder. Reversible molecular switching at a metal surface: A case study of tetra-tert-butyl-azobenzene on Au(111). Surf. Sci., 603(10-12):1506–1517, June 2009.

[126] G. Schulze, K. J. Franke, and J. I. Pascual. Induction of a Photostationary Ring-Opening—Ring-Closing State of Spiropyran Monolayers on the

Semimetallic Bi(110) Surface. Phys. Rev. Lett., 109(2):026102, July 2012.

[127] T. A. Darwish, Y. Tong, M. James, T. L. Hanley, Q. Peng, and S. Ye. Characterizing the Photoinduced Switching Process of a Nitrospiropyran Self-Assembled Monolayer Using In Situ Sum Frequency Generation Spectroscopy. Langmuir, 28(39):13852–13860, October 2012.

[128] J. C. Love, L. A. Estroff, J. K. Kriebel, R. G. Nuzzo, and G. M. Whitesides. Self-Assembled Monolayers of Thiolates on Metals as a Form of Nanotechnology. Chem. Rev., 105(4):1103–1170, April 2005.

[129] E. Katz, M. Lion-Dagan, and I. Willner. Control of electrochemical processes by photoisomerizable spiropyran monolayers immobilized onto Au electrodes: amperometric transduction of optical signals ". J. Electroanal. Chem., page 7, 1995.

[130] H. Wang, T. Gao, and W. Xiong. Self-Phase-Stabilized Heterodyne Vibrational Sum Frequency Generation Microscopy. ACS Photonics, 4(7):1839–1845, July 2017.

[131] B. Xu, Y. Wu, D. Sun, H.-L. Dai, and Y. Rao. Stabilized phase detection of heterodyne sum frequency generation for interfacial studies. Opt. Lett., 40(19):4472, October 2015.

[132] H. Vanselous and P. B. Petersen. Extending the Capabilities of Heterodyne-Detected Sum-Frequency Generation Spectroscopy: Probing Any Interface in Any Polarization Combination. J. Phys. Chem. C, 120(15):8175–8184, April 2016.

[133] H. P. Yuen and V. W. S. Chan. Noise in homodyne and heterodyne detection. Opt. Lett., 8(3):177–179, 1983.

[134] E. C. Fulmer, P. Mukherjee, A. T. Krummel, and M. T. Zanni. A pulse sequence for directly measuring the anharmonicities of coupled vibrations: Two-quantum two-dimensional infrared spectroscopy. J. Chem. Phys., 120(17):8067–8078, May 2004.

[135] T. Garling, R. K. Campen, M. Wolf, and M. Thämer. A General Approach To Combine the Advantages of Collinear and Noncollinear Spectrometer Designs in Phase-Resolved Second-Order Nonlinear Spectroscopy. J. Phys. Chem. A, 123(51):11022–11030, December 2019.

[136] J. W. Wilson and R. A. Bartels. Rapid Birefringent Delay Scanning for Coherent Multiphoton Impulsive Raman Pump–Probe Spectroscopy. IEEE J. Sel. Top. Quantum Electron., 18(1):130–139, January 2012.

[137] B. D. Guenther. Modern Optics. Oxford University Press, October 2015.

[138] P. Schlup, J. Wilson, K. Hartinger, and R. A. Bartels. Dispersion balancing of variable-delay monolithic pulse splitters. Appl. Opt., 46(23):5967–5973, 2007.

[139] A. W. Lawson. Comment on the Elastic Constants of Alpha-Quartz. Phys. Rev., 59(10):838–839, May 1941.

[140] M. Thämer, T. Garling, R. K. Campen, and M. Wolf. Quantitative determination of the nonlinear bulk and surface response from alpha-quartz using phase sensitive SFG spectroscopy. J. Chem. Phys., 151(6):064707, August 2019.

[141] E.A. Potterton and C.D. Bain. Infrared-infrared sum-frequency generation from adsorbates on metal surfaces. J. Electroanal. Chem., 409(1-2):109–114, June 1996.

[142] T.-A. Ishibashi and H. Onishi. A multiplex infrared-visible sum-frequency spectrometer with wavelength tunability of the visible probe. Appl. Phys. Lett., 81(7):1338, 2002.

[143] L. Florea, A. Hennart, D. Diamond, and F. Benito-Lopez. Synthesis and characterisation of spiropyran-polymer brushes in micro-capillaries: Towards an integrated optical sensor for continuous flow analysis. Sensor. Actuator., 175:92–99, December 2012.

189

[144] R. Delgado-Macuil, M. Rojas-López, V.L. Gayou, A. Orduña-Díaz, and J. Díaz-Reyes. ATR spectroscopy applied to photochromic polymer analysis. Mater. Charact., 58(8-9):771–775, August 2007.

[145] E. Pretsch, P. Bühlmann, and M. Badertscher. Structure Determination of Organic Compounds. Springer Berlin Heidelberg, Berlin, Heidelberg, 2009.

[146] O. Ivashenko, J. T. van Herpt, B. L. Feringa, P. Rudolf, and W. R. Browne. Electrochemical Write and Read Functionality through Oxidative Dimerization of Spiropyran Self-Assembled Monolayers on Gold. J. Phys. Chem. C, 117(36):18567–18577, September 2013.

[147] R. Superfine, J. Y. Huang, and Y. R. Shen. ol-15-22-1276.pdf. Opt. Lett., 15(22):1276–1278, 1990.

[148] C. D. Bain. Sum-frequency vibrational spectroscopy of the solid/liquid interface. Faraday Trans., 91(9):1281, 1995.

[149] B. Pettinger, C. Bilger, and J. Lipkowski. SHG Studies on Halide Adsorption at Au(111) Electrodes. In K. Wandelt and S. Thurgate, editors, Solid—Liquid Interfaces, volume 85, pages 223–242. Springer Berlin Heidelberg, Berlin, Heidelberg, 2003. Series Title: Topics in Applied Physics.

[150] S. A. Krysanov and M. V. Alfimov. Picosecond Flash Photolysis of Photochromic Spiropyrans. Laser Chem., 4(1-6):129–138, 1984.

[151] A. L. Rohl and D. M. P. Mingos. The size and shape of molecular ions and their relevance to the packing of the hexafluorophosphate salts. J. Chem. Soc., Dalton Trans., (24):3541, 1992.

[152] H. Saboorian-Jooybari and Z. Chen. Calculation of re-defined electrical double layer thickness in symmetrical electrolyte solutions. Results Phys., 15:102501, December 2019.

[153] J.-F. Cote, D. Brouillette, J. E. Desnoyers, J.-F. Rouleau, J.-M. St-Arnaud, and G. Perron. Dielectric constants of acetonitrile, ?-butyrolactone, propylene carbonate, and 1,2-dimethoxyethane as a function of pressure and temperature. J. Solution Chem., 25(12):1163–1173, December 1996.

[154] D. A. Outka, J. Stöhr, J. P. Rabe, and J. D. Swalen. The orientation of Langmuir–Blodgett monolayers using NEXAFS. J. Chem. Phys., 88(6):4076–4087, March 1988.

[155] A. K. Chibisov and H. Görner. Photoprocesses in spiropyran-derived merocyanines. J. Phys. Chem. A, 101(24):4305–4312, 1997.

[156] H. Görner. Photochromism of nitrospiropyrans: effects of structure, solvent and temperature. Phys. Chem. Chem. Phys., 3(3):416–423, 2001.

[157] G. L. Richmond. Second Harmonic Generation as an In-situ Probe of Single Crystal Electrode Surfaces. In H. Gerischer and C. W. Tobias, editors, Advances in Electrochemical Sciences and Engineering, volume 2, pages 141–204. Wiley, 1 edition, December 1991.

[158] A. Le Rille, A. Tadjeddine, W.Q. Zheng, and A. Peremans. Vibrational spectroscopy of a Au(hkl)-electrolyte interface by in situ visible-infrared difference frequency generation. Chem. Phys. Lett., 271(1-3):95–100, June 1997.

[159] S. Karimi, A. Moshaii, S. Abbasian, and M. Nikkhah. Surface Plasmon Resonance in Small Gold Nanoparticles: Introducing a Size-Dependent Plasma Frequency for Nanoparticles in Quantum Regime. Plasmonics, 14(4):851–860, August 2019.

[160] G. Ghosh. Dispersion-equation coefficients for the refractive index and birefringence of calcite and quartz crystals. Opt. Commun., 163(1-3):95–102, May 1999.

[161] P. B. Johnson and R. W. Christy. Optical Constants of the Noble Metals. Phys. Rev. B, 6(12):4370–4379, December 1972.

[162] C. Humbert, L. Dreesen, A. A. Mani, Y. Caudano, J.-J. Lemaire, P.A. Thiry, and A. Peremans. IR–visible sum-frequency vibrational spectroscopy of Biphenyl-3 methylene thiol monolayer on gold and silver: effect of the visible wavelength on the SFG spectrum. Surf. Sci., 502-503:203–207, April 2002.

[163] A. Chen, Z. Shi, D. Bizzotto, J. Lipkowski, B. Pettinger, and C. Bilger. Iodide adsorption at the Au(111) electrode surface. J. Electroanal. Chem., 467(1-2):342–353, June 1999.

[164] B. Pettinger, C. Bilger, J. Lipkowski, and W. Schmickler. Second Harmonic Generation Anisotropy from Single Crystalline Electrode Surfaces. In Andrzej Wieckowski, editor, Interfacial Electrochemistry, pages 373–404. Marcel Dekker, Inc., New York, Basel, 1999.

[165] J. Lipkowski, Z. Shi, A. Chen, B. Pettinger, and C. Bilger. Ionic adsorption at the Au(111) electrode. Electrochim. Acta, 43(19-20):2875–2888, June 1998.

[166] N. Bloembergen and P. S. Pershan. Light Waves at the Boundary of Nonlinear Media. Phys. Rev., 128(2):606–622, October 1962.

[167] A. T. Collins and G. S. Woods. An anomaly in the infrared absorption spectrum of synthetic diamond. Philos. Mag. B, 46(1):77–83, July 1982.

[168] P. Eberspächer, E. Wismeth, R. Buchner, and J. Barthel. Ion association of alkaline and alkaline-earth metal perchlorates in acetonitrile. J. Mol. Liq., 129(1-2):3–12, October 2006.

[169] J. Barthel and R. Deser. FTIR study of ion solvation and ion-pair formation in alkaline and alkaline earth metal salt solutions in acetonitrile. J. Solution Chem., 23(10):1133–1146, October 1994.

[170] J. F. Coetzee and W. R. Sharpe. Solute-solvent interactions. VII. Proton magnetic resonance and infrared study of ion solvation in dipolar aprotic solvents. J. Solution Chem., 1(1):77–91, July 1972.

[171] J. Barthel, L. Iberl, J. Rossmaier, H. J. Gores, and B. Kaukal. Conductance of 1,1-electrolytes in acetonitrile solutions from -40° to 35℃. J. Solution Chem., 19(4):321–337, April 1990.

[172] P.W. Atkins and J. de Paula. Physikalische Chemie, Vierte Auflage. Wiley-VCH Verlag GmbH & Co. KGaA, Weinheim, 2006.

[173] E. Panzram, H. Baumgärtel, B. Roelfs, C Schröter, and T. Solomun. A Capacitance and Infrared Study of the Electrical Double Layer Structure at Single Crystal Gold Electrodes in Acetonitrile. Ber. Bunsenges. Phys. Chem., 99(6):827–837, June 1995.

[174] O.A. Petrii and I.G. Khomchenko. Electrochemical properties of platinum and palladium electrodes in acetonitrile solutions. J. Electroanal. Chem. Interf. Electrochem., 106:277–286, January 1980.

[175] S. Babar and J. H. Weaver. Optical constants of Cu, Ag, and Au revisited. Appl. Opt., 54(3):477, January 2015.

[176] K. Moutzouris, M. Papamichael, S. C. Betsis, I. Stavrakas, G. Hloupis, and D. Triantis. Refractive, dispersive and thermo-optic properties of twelve organic solvents in the visible and near-infrared. Appl. Phys. B, 116:617–622, December 2013.

[177] S. Kedenburg, M. Vieweg, T. Gissibl, and H. Giessen. Linear refractive index and absorption measurements of nonlinear optical liquids in the visible and near-infrared spectral region. Opt. Mater. Express, 2(11):1588–1611, 2012.

[178] T. L. Myers, R. G. Tonkyn, T. O. Danby, M. S. Taubman, B. E. Bernacki, J. C. Birnbaum, S. W. Sharpe, and T. J. Johnson. Accurate Measurement of the Optical Constants n and k for a Series of 57 Inorganic and Organic Liquids for Optical Modeling and Detection. Appl. Spectrosc., 72(4):535–550, 2018.

[179] G. M. Hale and M. R. Querry. Optical Constants of Water in the 200-nm to 200-micro m Wavelength Region. <u>Appl. Opt.</u>, 12(3):555–563, March 1973.

Publications

1. T. Garling, Y. Tong, T. A. Darwish, M. Wolf, and R. K. Campen. The influence of surface potential on the optical switching of spiropyran self assembled monolayers. J. Phys.-Condens. Mat., 29(41):414002, October 2017.

2. T. Garling, R. K. Campen, M. Wolf, and M. Thämer. A General Approach To Combine the Advantages of Collinear and Noncollinear Spectrometer Designs in Phase-Resolved Second-Order Nonlinear Spectroscopy. J. Phys. Chem. A, 123(51):11022–11030, December 2019.

3. M. Thämer, T. Garling, R. K. Campen, and M. Wolf. Quantitative determination of the nonlinear bulk and surface response from alphaquartz using phase sensitive SFG spectroscopy. J. Chem. Phys., 151(6):064707, August 2019.

Declaration of Authorship

Name: Garling

First name: Tobias

Date of birth: xx.xx.xxxx *(not available in the electronic version)*

Student-ID: xxxxxxx *(not available in the electronic version)*

I declare to the Freie Universität Berlin that I have completed the submitted dissertation independently and without the use of sources and aids other than those indicated. The present thesis is free of plagiarism. I have marked as such all statements that are taken literally or in content from other writings. The dissertation has not been submitted in the same or similar form in any previous doctoral procedure.

I agree to have my thesis examined by a plagiarism examination software.

_____

(Location, date, signature)

For reasons of data protection, the curriculum vitae is not published in the electronic version.

For reasons of data protection, the curriculum vitae is not published in the electronic version.